UNIVERSITY OF CALIFORNIA SAN DIEGO

Dynamics of Tidally-Driven Flows in Coral Reef Shelves: Observations from Autonomous and Fixed Instruments

A dissertation submitted in partial satisfaction of the
requirements for the degree
Doctor of Philosophy

in

Engineering Sciences (Applied Ocean Science)

by

André Miguel Amador Ramírez

Committee in charge:

Professor Geno Pawlak, Chair
Professor Janet Becker
Professor Falk Feddersen
Professor Sarah Giddings
Professor Antonio Sánchez
Professor Sutanu Sarkar

2020

The Dissertation of André Miguel Amador Ramírez is approved, and it is acceptable in quality and form for publication on microfilm and electronically:

_____

_____

_____

_____

_____

_____

Chair

University of California San Diego

2020

TABLE OF CONTENTS

LIST OF FIGURES

LIST OF TABLES

ACKNOWLEDGEMENTS

First and foremost I would like to acknowledge and thank my advisor, Geno Pawlak, for his guidance, patience, and support over the course of my PhD. His honest and insightful feedback has been invaluable to my development as a researcher. I sincerely appreciate the opportunities to do fieldwork in some spectacular places, particularly in O'ahu and the Seychelles. I also want to thank my committee members for all your brilliant comments and suggestions, and for letting my defense be an enjoyable moment.

Despite not having family in San Diego, I was lucky to enough to have an incredible support network in San Diego who deserve my heartfelt gratitude, in particular all my SIO and MAE classmates and colleagues as well as the Puerto Rican surfing crew. Thanks especially to Jesse Vassallo and Dr. Cruz for stitching me up (twice) after the occasional surfing mishap.

To all the people who motivated me to pursue a PhD: Jorge Corredor, Julio Morell, and Miguel Canals – thank you for training me and opening the door to scientific research. I am eternally grateful to my parents for instilling in me a passion for the ocean and to my sister Paola for coming to visit and for making me a proud brother and uncle. Finally, thanks to Adriana Rivero, who was always there through the ups and downs of my PhD journey, for all her love and support, I am eternally grateful.

Chapter 2, in full, is a reprint of published work featured in the Journal of Atmospheric and Oceanic Technology (Amador A., Jaramillo S., and Pawlak G., 2017). The dissertation author was the primary investigator and author of this paper.

Chapter 3 is currently being prepared for submission for publication (Amador A., Giddings S. N., and Pawlak G., 2020). The dissertation author was the primary investigator and author of this paper.

Chapter 4 is currently being prepared for submission for publication (Amador A., Arzeno I. B., Giddings S. N., Merrifield M., and Pawlak G., 2020). The dissertation author was the primary investigator and author of this paper.

VITA

2010	B. S. in Mechanical Engineering, University of Puerto Rico, Mayagüez
2013	M. S. in Mechanical Engineering, University of Puerto Rico, Mayagüez
2020	Ph. D. in Engineering Sciences (Applied Ocean Science), University of California, San Diego

PUBLICATIONS

Amador, A., Jaramillo, S., and Pawlak, G. "ADCP Bias and Stokes Drift in AUV-Based Velocity Measurements", *Journal of Atmospheric and Oceanic Technology*, 34 (9):2029–2042, 2017.

Amador A., and Canals, M. "Design and development of an Instrumented Drifter for Lagrangian Measurements of Inertial Particle Dynamics in Breaking Waves", *IEEE Journal of Oceanic Engineering*, 41(1):82–93, 2015.

Corredor, J.E., Amador, A., Canals, M., Rivera, S., Capella, J.E., Morell, J.M., Glenn, S., Roarty, H., Handel, E., and Lemus, E.R., "Optimizing and Validating High-frequency Radar Surface Current Measurements in the Mona Passage", *Marine Technology Society Journal*, 45(3):49–58, 2011.

ABSTRACT OF THE DISSERTATION

Dynamics of Tidally-Driven Flows in Coral Reef Shelves: Observations from Autonomous and Fixed Instruments

by

André Miguel Amador Ramírez

Doctor of Philosophy in Engineering Sciences (Applied Ocean Science)

University of California San Diego, 2020

Professor Geno Pawlak, Chair

The present work examines the hydrodynamics of the inner-shelf region, focusing on tidally-driven alongshore flows over coral reef shelves. This study draws on field data collected in O'ahu, Hawai'i using fixed and mobile assets to develop new modes of observational research.

First, a theoretical model is developed to describe how autonomous underwater vehicle (AUV)-based water velocity measurements are influenced by a surface wave field. The model quantifies a quasi-Lagrangian, wave-induced velocity bias as a function of the local wave conditions, and the vehicle's depth and velocity using a first-order correction to the linear wave solution. The theoretical bias is verified via field experiments over a range of wave and current conditions.

The analysis considers velocity measurements made using a REMUS-100 AUV, but the findings apply to any small AUV (vehicle size $\ll$ wavelength) immersed in a wave field. The observed wave-induced biases [O(1–5) cm s^{-1}] can be significant, and can be comparable to steady flow velocities for inner-shelf regions.

Second, a new approach to estimate lateral turbulent Reynolds stresses ($\overline{u'v'}$) in wavy coastal environments using acoustic Doppler current profilers (ADCPs) is described. The performance of the proposed method is evaluated via comparisons with independent acoustic Doppler velocimeter (ADV)-based stress estimates at two sites, and the vertical structure of the tidally-averaged turbulent Reynolds stresses is examined for an unstratified, tidally-driven flow over a rough coral reef seabed in weak waves. Observations and analysis indicate that lateral stresses are sustained by the cross-shore gradient of the mean alongshore flow, and driven by bottom-generated turbulence. Scaling considerations suggest that cross-shore transport by lateral turbulent mixing could be relevant to coral reef shelves with steep cross-reef slopes and rough bottoms.

Finally, a tidally-driven alongshore flow over a forereef shelf is examined using AUV-based spatial velocity measurements along with time series data of the alongshore pressure gradient. Ensemble phase averages of AUV-based velocities reveal characteristics akin to an oscillatory boundary layer, with the nearshore flow leading the offshore flow in phase and with a corresponding velocity magnitude attenuation near the shallower regions of the reef. Analysis of the depth-averaged alongshore momentum equation indicates that the cross-shore structure and evolution of the alongshore flow is well described by a balance between local acceleration, barotropic pressure gradient, and bottom drag. This primary balance allows the estimation of a spatially-averaged drag coefficient as a function of cross-shore distance over depths spanning from 24 to 6 m. Seabed roughness data suggest that larger scales, with wavelengths of O(10 m), are more relevant than smaller meter-scale roughness for drag.

Chapter 1

Introduction

1.1 Background

The inner-shelf region connects the open ocean with the outer edge of the surf zone, and typically spans depths from a few meters to a few tens of meters (Lentz and Fewings, 2012). To a large extent, the inner-shelf represents a bottleneck for mass and momentum flux, where we can anticipate a minimum in cross- and along-shore transport and dispersion. From the outer shelf, dispersion will decrease shoreward, with diminishing depth and distance from shore (Nickols et al., 2012). From shore, dispersion rapidly decreases outside of the surf zone (Clark et al., 2010) as the influence of wave-driven flow weakens. We can consider the dynamics of the inner-shelf as part of a closely coupled interface constrained by flow associated with strong forcing at the shoreward and seaward boundaries.

A key feature of the inner-shelf region is that it is typically dominated by alongshore flows due to the presence of a coastal boundary (Lentz and Fewings, 2012). Numerous mechanisms can drive alongshore flows, and different natural settings are often governed by multiple processes that span a diverse range of spatial and temporal scales. It has long been known that obliquely incident waves can force alongshore currents within the surf zone via spatial gradients in radiation stress

(Longuet-Higgins and Stewart, 1964), and a considerable amount of work has been devoted to this subject (e.g., Bowen, 1969; Longuet-Higgins, 1970; Thornton and Guza, 1986; Feddersen and Guza, 2003). Offshore of the surf zone, a wide variety of inner-shelf processes have been observed to drive alongshore flows, including winds, tides, buoyant plumes, and waves (Lentz and Fewings, 2012). Historically, most inner-shelf studies have focused on subtidal flow, averaging over intratidal timescales and processes. In such cases, the primary balance for the depth-averaged momentum equations has been shown to be dominated by wind stress, along-shelf pressure gradients, and bottom friction (e.g., Mitchum and Clarke, 1986; Lentz and Winant, 1986; Lentz, 1994; Lentz et al., 1999; Fewings and Lentz, 2010).

While often not as energetic as alongshore currents, cross-shelf flows govern the exchange of sediments, nutrients, contaminants, and biota between the coastal boundary and the open ocean (Brink, 2016). Cross-shelf transport processes are enabled by wave-driven Stokes drift and undertow (e.g., Lentz et al., 2008; Kumar et al., 2012); rip currents (e.g., Hally-Rosendahl et al., 2014; Suanda and Feddersen, 2015); thermally-driven exchanges (e.g., Molina et al., 2014; Ulloa et al., 2018); wind-driven circulation (e.g., Austin and Lentz, 2002; Lentz and Fewings, 2012; Horwitz and Lentz, 2016); shoaling and breaking of non-linear internal waves (e.g., Sinnett et al., 2016); and turbulence generated at the coastal (e.g., Nickols et al., 2012) and bottom (e.g., Trowbridge and Elgar, 2001; Feddersen and Williams, 2007) boundary layers. For coastal flows, it is generally assumed that the horizontal length scales are much larger than the vertical length scales (Burchard, 2002; Burchard et al., 2008); thus, the horizontal gradients of the turbulent fluxes are often neglected. Coastal boundaries, however, require further attention as spatial gradients in bottom roughness and water depth (bottom drag) can lead to substantial cross-shore gradients in the alongshore flow, and hence to enhanced turbulent mixing and lateral transport (Brink, 2016).

Considering the multi-layered structure of shelf circulation along with the shoreward diminishing length scales, there is a strong analogy with wall-bounded turbulent flow. Indeed,

Csanady (1972) referred to a shelf "coastal boundary layer", and Nickols et al. (2012) argue that the cross-shore structure of the along-shore velocity for the shelf might be described by a log profile as for the turbulent boundary layer. Yet, a description of the spatio-temporal structure of the coastal boundary layer, especially on intratidal timescales, is absent from existing inner-shelf literature. Accordingly, advancement on the dynamics within the inner-shelf and the associated cross-shelf transport of mass and momentum requires resolution of inner-shelf flows at scales ranging from the local water depth to the distance from shore.

1.2 Coral reef hydrodynamics

Inner-shelf flows regulate many ecological processes in coastal marine systems, and are especially vital for coral reefs environments. Coral reefs build intricate three-dimensional structures that support large numbers of marine species (Roberts et al., 2002), protect low-latitude shorelines against coastal flooding and erosion by dissipating wave energy (Ferrario et al., 2014; Quataert et al., 2015), and provide important ecosystem services of great economic value (Pratchett et al., 2008), including food security for millions of people around the world (Gove et al., 2016). The turbulent processes associated with wave and current flow over these irregular boundaries are at the foundation of littoral hydrodynamics, with the bed shear stress as the key parameter affecting dissipative and dispersive mechanisms.

Hydrodynamic forces influence many reef ecosystem processes, including their growth, health, and metabolism (Lowe and Falter, 2015). For example, reef-scale circulation patterns determine larval retention and dispersal rates (Cowen and Sponaugle, 2009; Wolanski and Kingsford, 2014), and play a primary role in regulating the supply of nutrients (Falter et al., 2004) and the transport of heat (Davis et al., 2011; Pineda et al., 2013; Zhang et al., 2013) between reef and the adjacent ocean. At smaller scales, the turbulent processes associated with wave and current flow over coral reefs modulate nutrient uptake and release rates (Atkinson and Bilger,

1992; Baird and Atkinson, 1997; Wyatt et al., 2012), particulate capture by coral (Sebens et al., 1998; Hughes and Grottoli, 2013) and reef heterotrophs (Yahel et al., 1998; Genin et al., 2009; Wyatt et al., 2010), and contribute to the overall health of the benthic community (Baird and Atkinson, 1997; Atkinson et al., 2001; Hearn et al., 2001; Monismith, 2007).

For coastal reef systems, most of the work has focused on wave-driven circulation resulting from wave breaking and the ensuing wave setup (Monismith, 2007; Lowe and Falter, 2015). While some studies have examined the role of tidal modulation on wave setup (Lugo-Fernandez et al., 1998; Taebi et al., 2011; Becker et al., 2014) and the hydrodynamics of tide-dominated reef platforms and atolls (Lowe et al., 2015; Green et al., 2018), the hydrodynamics of tidally-driven alongshore flows has received little attention. This raises the question of what is the semidiurnal flow response for coral reef shelves where the tidal pressure gradient is the dominant forcing mechanism.

Previous research at the Makua forereef on the western coast of O'ahu, Hawai'i indicates that the alongshore flow at the 12 m isobath is described on semidiurnal timescales by a balance between the local acceleration, the barotropic pressure gradient, and the bottom drag (Arzeno et al., 2018). However, a spatio-temporal description of the flow structure and the resulting nearshore circulation is lacking. This is in part because reef scale circulation patterns are intrinsically tied to their rough and complex morphologies, and accurately predicting the flow and drag forces over such irregular morphologies remains a major challenge (Rosman and Hench, 2011; Lowe and Falter, 2015; Lentz et al., 2017).

1.3 AUV methods

Over the last two decades unmanned autonomous underwater vehicles (AUVs) have enabled the resolution of spatio-temporal flow velocities in coastal and inner-shelf waters (e.g., Fong and Jones, 2006; Boyd et al., 2010; Jaramillo and Pawlak, 2010; Rogowski and Terrill,

2015). The portability, economy, and maneuverability offered by AUVs has made possible new capabilities in spatial hydrodynamic mapping. Capable of independently completing a pre-programmed mission, AUVs provide a viable, and often preferable, alternative to traditional ship-based techniques. Furthermore, AUVs can cruise at low and constant elevations over the seabed, making them particularly well suited for sampling bed roughness in environments such as coral reefs, where roughness features can change abruptly over short distances (Jaramillo and Pawlak, 2011).

The REMUS-100 (Remote Environmental Measuring UnitS, Hydroid Inc) is a compact (160 cm in length, 19 cm in diameter), light-weight (37 kg), torpedo-shaped AUV designed for operation in coastal environments (Brown et al., 2004; Moline et al., 2005). These propeller-driven vehicles use tail fins and rudders for steering and diving, and can operate at depths of up to 100 m. Subsurface navigation is typically achieved by employing an on-board dead-reckoning navigation system based on a downward-looking acoustic Doppler current profiler (ADCP) configured as a Doppler velocity log (DVL) for bottom-tracking, and a combination of inertial and magnetic sensors. The DVL bottom-tracking is aided by long baseline (LBL) acoustics, which triangulate the vehicle's position using acoustic signals from widely spaced fixed acoustic transponders (Paull et al., 2014). The navigation algorithm then integrates the measurements from each sensor to give continuous, high-rate estimates of the vehicle's position, orientation, and velocity.

RDI manufactured DVLs are very similar to the commonly used broadband RDI Workhorse ADCPs, and can be used to measure both the vehicle speed (via bottom-tracking) and velocity profiles in the water column (Fong and Jones, 2006). Obtaining water column velocities from a moving platform requires at least two measurements: a water track ping, which measures the relative velocity of the instrument to the water, and a bottom track ping, which measures the relative velocity of the instrument to the bottom (Fong and Monismith, 2004). The velocity of the instrument is thus removed from the raw DVL estimate of the different layers in the water column (depth bins). This difference, in the absence of any acceleration between the pings, results in the

water velocities in an earth-based reference frame.

It is worth noting, however, that extracting viable velocity measurements from a moving platform comes with its own set of challenges. Because of the inherent error in individual DVL velocity samples, AUV-based measurements often rely on spatial averaging to deduce useful estimates of flow velocities (Fong and Jones, 2006). In addition, velocity measurements from AUVs are subject to wave-induced biases and other unexplained biases (Fong and Jones, 2006). In coastal flows, for example, systematic errors of several centimeters per second can become limiting because coastal currents can be comparable in magnitude, especially in the cross-shore direction.

1.4 Research questions

The aim of this research is to examine the hydrodynamics of the inner-shelf region and its turbulence characteristics, focusing on tidally-driven alongshore flows on intratidal timescales in coral reef environments. Furthermore, the present work enables and validates new modes of observational research by combining the use of mobile, autonomous assets with traditional methods for fixed instrumentation.

Specifically, this research addresses the following questions:

- **What is the efficacy of using AUV-based velocity observations for resolving the hydrodynamic properties of coastal and inner-shelf flows?**

  Despite the fact that AUV-based current velocity profiling has been possible for over a decade, research work assessing the validity of such measurements is still scarce. Of particular concern are systematic errors in the velocity measurements, which cannot be eliminated or reduced via averaging, and complicate the measurement of flow velocities. In Chapter 2, a theoretical model is developed to describe how AUV-based current measurements are influenced by a surface wave field. The model quantifies a wave-induced

velocity bias as a function of the local wave conditions, and the vehicle's depth and velocity using a first-order expansion of the linear wave solution. Consistent with a previously observed phenomenon (Fong and Monismith, 2004; Fong and Jones, 2006), we report on the presence of an additional bias in the direction of the vehicle motion. The work considers velocity measurements made using a REMUS-100 AUV outfitted with an upward- and downward-looking four beam 1200 kHz RD Instruments DVL, but the analysis applies to any small AUV (vehicle size $\ll$ wavelength) immersed in a wave field.

- **Can existing wave-turbulence decomposition methods be modified to quantify the turbulence structure and dominant scales associated with the lateral ($\overline{u'v'}$) Reynolds stresses?**

  In the coastal ocean, the effects of surface gravity waves complicate the measurement of the turbulent stresses. This is because the oscillating wave velocities are typically orders of magnitude greater than the turbulent fluctuations, and often overlap with the turbulent motions in frequency space. Research on the subject of wave-bias removal has been mostly limited to observations of vertical momentum fluxes ($\overline{u'w'}$ and $\overline{v'w'}$). In contrast, there has been little discussion about the turbulence statistics associated with the lateral momentum fluxes ($\overline{u'v'}$) in the nearshore and inner-shelf literature. At present, direct measurements of inner-shelf turbulence are scarce, and the role of the lateral turbulent stresses in cross-shelf transport is not well understood. Chapter 3 describes a new approach based on the variance method to estimate lateral Reynolds stresses from ADCP-based velocity observations in the presence of surface gravity waves, and offers new insights into the temporal variability and vertical structure of the lateral stresses in tidally-dominated coral reef environments. The experimental data used in Chapter 3 were collected at the Makua reef on the western coast of O'ahu, Hawai'i in tidally-driven, unstratified flow under moderate swell conditions.

- **How do cross-shore variations in bathymetry and roughness affect the resulting along-**

shore reef-scale flow response?

Coral and rocky reefs, common to low latitude coastlines, are characterized by highly irregular and inhomogeneous bathymetry with widely varying roughness scales. Accurately predicting the flow and drag forces over such irregular morphologies remains a major challenge. Chapter 4 presents AUV-based spatial velocity measurements along with time series data of the alongshore pressure gradient to examine the cross-shore structure and evolution of a tidally-driven alongshore flow over a fringing coral reef shelf on the western coast of O'ahu, Hawai'i. In Chapter 4, we formulate a simple 1D flow model that incorporates the effects of waves on the bottom drag, and allows the estimation of an average drag coefficient. We then investigate the hydrodynamically relevant roughness scales for coral reef environments via spatial measurements of benthic roughness.

1.5 Thesis outline

This thesis is organized in the form of a series of manuscripts that were prepared for publication in peer-reviewed journals (Chapters 2–4). In order for these chapters to stand as individual publishable units, some repetition of introductory material was necessary. Chapter 2 examines the details of using an AUV to measure flow velocities in the coastal ocean, where the ubiquitous presence of surface waves introduce a bias that is related to Stokes drift. Chapter 3 describes and evaluates a new approach based on the variance method to estimate lateral Reynolds stresses from ADCP-based velocity observations; we then use the proposed technique to offer new insights into the temporal variability and vertical structure of the lateral Reynolds stresses in tidally-dominated coral reef environments. Chapter 4 examines the cross-shore structure and evolution of a tidally-driven alongshore flow over a fringing coral reef shelf on the western coast of O'ahu, Hawai'i.

Chapter 2

ADCP Bias and Stokes Drift in AUV-Based Velocity Measurements

2.1 Introduction

The advent of small, manually deployable autonomous underwater vehicles (AUVs) equipped with Doppler velocity logs (DVLs) has revolutionized the way in which we monitor marine environments. The portability and economy offered by AUVs provides the opportunity for extensive hydrodynamic mapping in a variety of environments, some of which were previously unattainable by traditional ship-based techniques. For example, AUVs have been used for high-resolution hydrographic surveys in deep water Stansfield et al. (2001, 2003) and submarine canyons (Sumner et al., 2013), for turbulence microstructure observations in the continental shelf (Goodman and Wang, 2009), to observe plume dispersion in coastal waters (Rogowski et al., 2014) and over coral reefs (Jones et al., 2008), and to measure velocity profiles in shallow lakes and riverine environments (Brown et al., 2011). In each of these cases, AUVs have provided an efficient solution for collecting spatial data including flow velocities.

This dramatic increase in the amount of AUV-based data has motivated the need for

effective measurement practices and the assessment of error sources that affect the reliability of the measurements. Of particular concern are systematic errors in the velocity measurements, which cannot be eliminated or reduced via averaging and can complicate the measurement of the flow field. In coastal flows, for example, systematic errors of several centimeters per second can become important because coastal currents can be comparable in magnitude, especially in the cross-shore direction.

AUV subsurface navigation is typically achieved using on-board dead-reckoning systems based on DVLs and a combination of inertial sensors (accelerometers and/or gyroscopes) and a magnetic compass. DVLs use acoustic measurements to determine the vehicle's velocity relative to the seabed. Dead-reckoning navigation is aided by long baseline (LBL) acoustic positioning, which triangulates the position of the vehicle using acoustic signals from widely spaced fixed acoustic transponders (Paull et al., 2014). The navigation algorithm then integrates the measurements from the navigation sensors to give high-rate estimates of the position, orientation and velocity of the vehicle.

DVLs determine a vehicle's velocity vector using multiple (typically three or four) downward acoustic beams oriented at angles relative to each other, commonly in a convex arrangement. The Doppler shift in the bottom reflection from each beam is processed to determine the velocity component in the beam direction. With four angled beams, the three-dimensional velocity vector for the vehicle can be calculated along with an error estimate. DVLs can also be configured as acoustic Doppler current profilers (ADCP) to measure water velocities. In this case, Doppler shifts are calculated from water column reflections within discrete range intervals (bins) along each beam. Velocity components along each beam are then combined to obtain a profile of the three-dimensional water velocity vector. Since the beams diverge with distance from the DVL (or ADCP), the effective sampling volume similarly increases.

To construct velocity profiles in an earth based reference frame from a moving platform, the velocity of the instrument relative to the bottom must be removed from the raw water column

velocity estimate. Fong and Monismith (2004) examined the accuracy of a DVL bottom tracking system using concurrent high-resolution kinematic GPS data and found that average vessel speeds were in excellent agreement over multiple transects of several hundred meters in length. Because of the inherent error in individual ADCP velocity samples, AUV-based measurements often rely on spatial averaging to deduce useful estimates of water current velocities (Fong and Jones, 2006).

In this paper we focus on two unrelated types of bias errors that affect AUV-based velocity estimates. First, we examine a wave-induced bias that is closely related to Stokes drift. Second, consistent with a previously observed phenomenon (Fong and Monismith, 2004; Fong and Jones, 2006), we report on the presence of an additional bias in the direction of the vehicle motion. This work considers velocity measurements made using a REMUS-100 AUV (Hydroid Inc.) outfitted with a four beam 1200 kHz RD Instruments DVL (similar to RD Instruments Workhorse ADCP). The REMUS-100 is a compact (160 cm in length, 19 cm in diameter), light-weight (37 kg), torpedo-shaped AUV designed for operation in coastal environments (Brown et al., 2004; Moline et al., 2005; Amador et al., 2015). The analysis here, however, applies to any small AUV (vehicle size $\ll$ wavelength) immersed in a wave field.

In section 2.2, we show how AUV-based current measurements may be influenced by perturbations in the vehicle trajectory caused by the wave field. We develop a theoretical framework to quantify a wave-induced velocity bias as a function of the local wave conditions, and the vehicle's depth and velocity. In section 2.3, we describe our field observations and present analysis of a series of tests in wave forced, fringing coral reef environments to examine the effects of spatial averaging in AUV-based velocity measurements. We compare the expected uncertainty estimates to root mean square deviations (RMSD) of depth-averaged, normalized velocity differences, to show that wave-induced uncertainties dominate the random error present in our data. In section 2.4, we calculate ensemble-averaged along- and cross-track velocity differences ($\langle \Delta V \rangle = \langle V_{\mathrm{AUV}} - V_{\mathrm{ADCP}} \rangle$) from fixed ADCP measurements to investigate the accuracy of AUV-based water velocity measurements and to explore the presence of velocity biases. Results

are discussed and summarized in sections 2.5 and 2.6, respectively.

2.2 Background

Although the REMUS-100 can be programmed to maintain a prescribed depth and speed, surface waves have the potential to influence its dynamics. In practice, the wave field will perturb the vehicle's speed and vertical displacement to a degree, especially in shallow water, in routes near the sea surface, and in the presence of large waves (e.g., Goodman et al., 2010; Sgarioto, 2011; Amador et al., 2015; Haven and Terray, 2015). Here we show how the influence of the wave velocity field on the vehicle trajectory can lead to a bias in spatially-averaged velocity measurements, and we develop a theoretical framework to quantify this bias.

2.2.1 Vehicle trajectory

Consider an AUV traversing a monochromatic wave field, operating at some constant average depth, Z_0, as shown in Figure 2.1. Let a represent the wave amplitude, h the local depth, σ the wave radian frequency, k the wavenumber, and $c = \sigma/k$ the phase speed. We assume inviscid, irrotational flow and that the vehicle closely follows the horizontal and vertical water displacements produced by surface gravity waves. Hence, the velocity of the vehicle is given by

$$u_{auv}(x,z,t) = U + u_w\,, \tag{2.1}$$

$$w_{auv}(x,z,t) = w_w\,, \tag{2.2}$$

where U is the constant horizontal cruising speed of the vehicle (relative to the water) and

$$u_w = a\sigma\frac{\cosh\left(k(z+h)\right)}{\sinh(kh)}\cos(kx-\sigma t)\,, \tag{2.3}$$

$$w_w = a\sigma\frac{\sinh\left(k(z+h)\right)}{\sinh(kh)}\sin(kx-\sigma t)\,, \tag{2.4}$$

are the components of wave orbital velocity from linear theory in Cartesian coordinates with x horizontal and z vertical. Time-integrating (2.1) and (2.2), it follows that the trajectory of the vehicle is described (to first order) by

$$x_{auv} = X_0 + Ut - a\frac{\sigma}{\omega}\frac{\cosh\left(k(Z_0+h)\right)}{\sinh(kh)}\sin\left(kX_0 - \omega t\right), \tag{2.5}$$

$$z_{auv} = Z_0 + a\frac{\sigma}{\omega}\frac{\sinh\left(k(Z_0+h)\right)}{\sinh(kh)}\cos\left(kX_0 - \omega t\right), \tag{2.6}$$

where ω is the Doppler shifted frequency and X_0, Z_0 denote the initial horizontal position and the mean vertical position of the vehicle, respectively (see details in Appendix A). Note that the horizontal velocity of the vehicle relative to the surface wave phase introduces a Doppler shift, $\omega = \sigma - kU$, which modulates the influence of the wave field on the vehicle. This vehicle-wave interaction brings about two processes that lead to a velocity bias in spatially-averaged velocity measurements.

First, the vehicle's velocity relative to the waves acts to modify its vertical motion; this is evident from equation (2.6). Note that when $U = 0$, $\omega = \sigma$, the vehicle path matches the orbital trajectory of a fluid parcel at that location, and the average (over one wave cycle) horizontal velocity measured at the vehicle's location is the Stokes drift velocity. When $U \neq 0$, the vehicle's vertical excursions are modified relative to the fluid trajectory, so that the average horizontal velocity measured along the vehicle path then differs from the Stokes drift velocity. We refer to the vehicle path as "quasi-Lagrangian" since it includes a component that is related to the Lagrangian Stokes drift, but is modified by the vehicle's cruising speed. The spatial average of the quasi-Lagrangian vertical motions then result in a velocity bias in the direction of wave propagation because the vehicle samples faster velocities at the top of its trajectory than it does at the bottom of its trajectory. As $U \to \pm\infty$, $\omega \to \pm\infty$, the vehicle's speed precludes interactions with the wave field, completely suppressing the amplitude of its vertical motions with $z_{auv} \to Z_0$, so that the wave-induced bias vanishes.

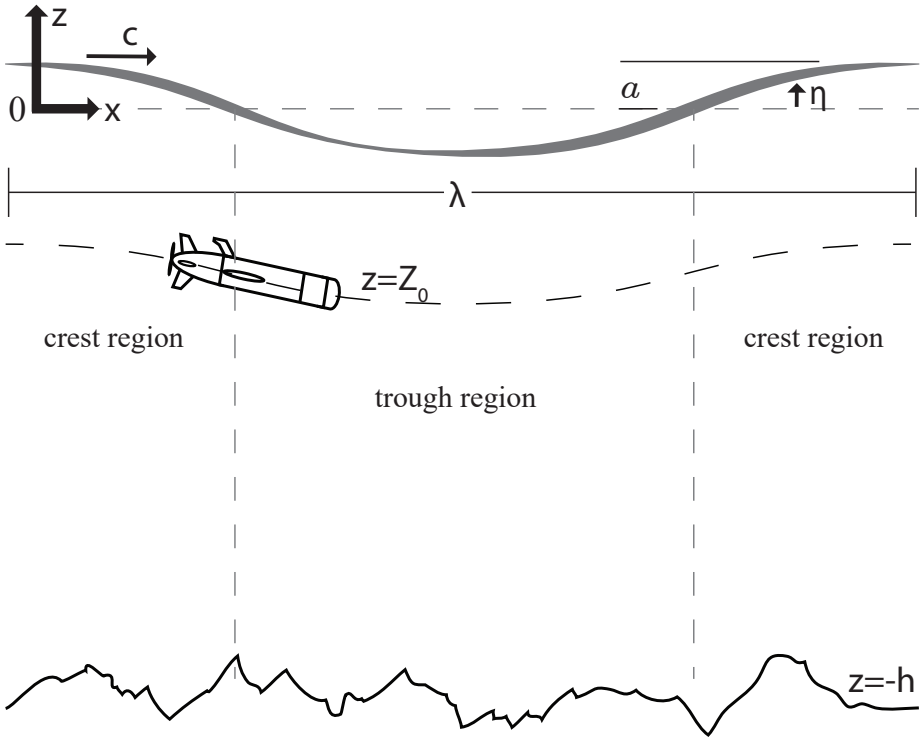

Figure 2.1: AUV traversing a monochromatic wave field. Note the coordinate system ($z = 0$ at the mean sea surface $\overline{\eta}$), the crest ($\eta > 0$) and trough ($\eta < 0$) regions of the wave, and key parameters: wave amplitude (a), wave length (λ), wave speed (c), water depth (h), and vehicle depth (Z_0).

The second effect arises due to changes in temporal sampling of crest versus trough regions. As shown in Figure 2.1, the sign of the surface vertical displacement, η, defines the crest and trough regions. In the vehicle reference frame, the surface wave is described by

$$\eta_{auv} = a\cos(kx_{auv}(t) - \sigma t)\,, \tag{2.7}$$

where $x_{auv}(t)$ is given by (2.5). We find the times for the zero crossings where

$$kx_{auv}(t) - \sigma t = \pm\frac{\pi}{2}\,. \tag{2.8}$$

Solving for these crossings allows us to compare the vehicle's temporal sampling of crest versus trough regions (see Figure 2.2).

An observer at a fixed location (Eulerian perspective) would spend an equal amount of time on either region of the wave. However, the interaction between the vehicle and the wave field acts to prolong the vehicle's time in the crest. Figure 2.2 shows the fraction of time the vehicle spends under the crest region per wave cycle as a function of the non-dimensional vehicle cruising speed. It is observed that the vehicle oversamples the wave crests, thus leading to aliasing of average velocity measurements in the direction of wave travel. This effect becomes more prominent as U increases towards the wave phase speed. A vehicle traveling exactly at the wave phase speed ($u_{auv} = c$) would ride on a crest and would thus sample only shoreward motion. As $U \to \pm\infty$ the vehicle-wave interaction becomes inconsequential, and the vehicle spends an equal amount of time in all parts of the wave. Finally, because wave motions decay as a function of depth, the influence of the wave field on the vehicle will be more prominent for sampling routes near the sea surface (Amador et al., 2015).

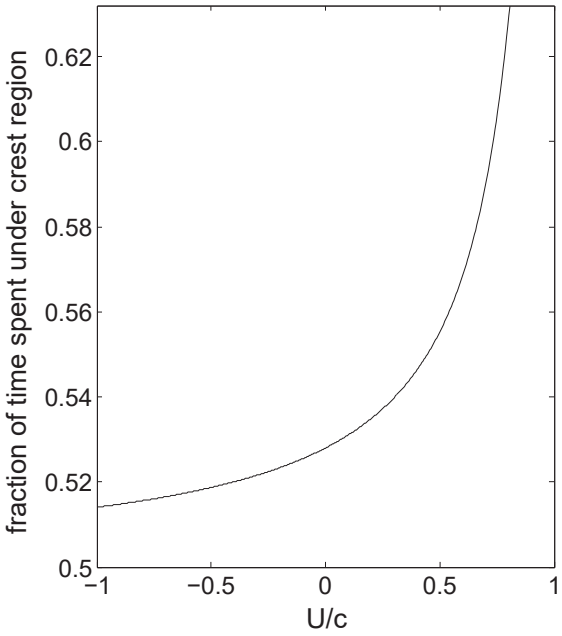

Figure 2.2: Fraction of time spent under the crest region of the wave per wave cycle as a function of the non-dimensional vehicle cruising speed (U/c), for vehicle depth $Z_0 = -3$ m and local wave conditions: wave amplitude $a = 1$ m, wave period $T = 10$ s, and depth $h = 12$ m.

2.2.2 Wave-induced bias

We can now compute the horizontal (u) velocity profile, u_{Lq}, relative to the earth as measured by an onboard ADCP. This velocity is termed a quasi-Lagrangian measurement, because it is a function of the interaction between the AUV motion and the Lagrangian flow at the AUV position, all extrapolated to the ADCP measurement location. We denote the height of the range cell (above or below the AUV) by Δz. Then

$$u_{Lq} = u_w\left(x_{auv}(t), z_{auv}(t) + \Delta z; t\right) , \tag{2.9}$$

where the vehicle trajectory, $x_{auv}(t)$ and $z_{auv}(t)$, is given by (2.5) and (2.6), respectively. Expanding (2.9) to include first order-variations in both fluid velocity components and time-averaging

over one wave cycle (see Appendix A), we arrive at an expression for the wave-induced bias

$$\overline{u}_{Lq} = a^2 k \frac{\sigma^2}{\omega} \frac{\cosh\left(2k(Z_0+h)+k\Delta z\right)}{2\sinh^2\left(kh\right)}. \tag{2.10}$$

Figure 2.3 shows the wave-induced bias ($\overline{u}_{Lq}$) normalized by the Stokes drift ($\overline{u}_{St}$) at the vehicle depth (Z_0) for different vehicle velocities in deep water waves with period $T = 10$ s. The black dashed line illustrates the solution of (2.10) when $U = 0$, the gray dashed line represents the non-dimensional depth of the vehicle, and the gray bold line shows the normalized Stokes drift profile. As expected, the measured velocity matches the Stokes drift at the vehicle's depth (i.e., $\overline{u}_{Lq}/\overline{u}_{St,Z_0} = 1$) when $U = 0$. However, the measured profile deviates from Stokes drift with varying depth because the velocity at each depth is sampled using particle paths at the vehicle depth, which differ from the local particle paths that result in the actual vertical variation in the Stokes drift (Amador et al., 2015). In other words, for $U = 0$, the wave-induced bias is greater than the Stokes drift below the vehicle depth, Z_0, because the orbital paths of the range cells are greater than the particle orbits below the vehicle depth. The opposite is true for velocity measurements obtained above Z_0.

As discussed in section 2.2.1, the vehicle's horizontal velocity relative to the wave phase modifies the wave-induced bias—the solid black lines presented in Figure 2.3 illustrate this effect. Note that the wave-induced bias is enhanced when the vehicle moves in the direction of wave propagation ($U > 0$) because the Doppler shifted frequency decreases. Conversely, when the vehicle moves against the waves ($U < 0$), the Doppler frequency increases and the wave-induced bias is diminished.

2.3 Field data

We present data from AUV hydrodynamic surveys over coral reefs at two different locations off the coast of O'ahu, Hawai'i. The description of the field observations in the next

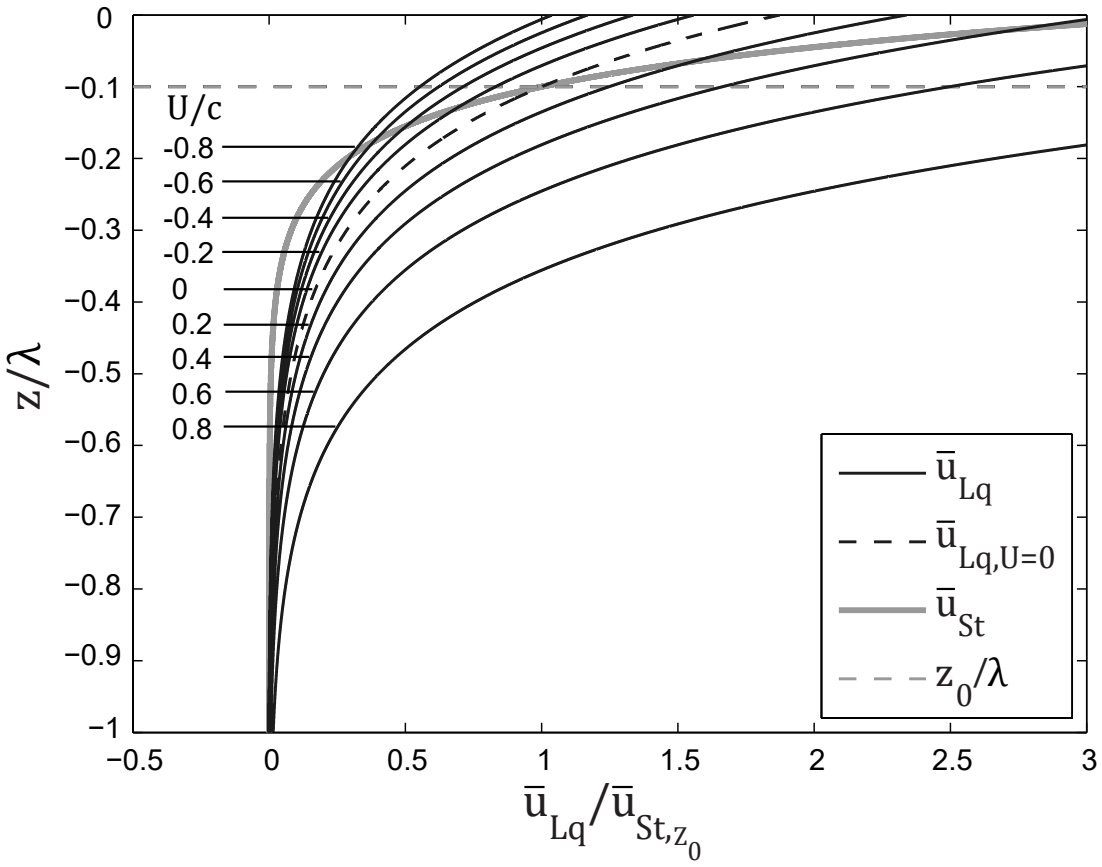

Figure 2.3: Wave-induced bias ($\overline{u}_{Lq}$) as a function of non-dimensional depth (z/λ) for different vehicle velocities in deep water waves with period $T = 10\,\mathrm{s}$. Results have been normalized by the Stokes drift velocity ($\overline{u}_{St}$) at the vehicle depth ($Z_0/\lambda = 0.1$). The black and gray dashed line illustrate the solution of (2.10) when $U = 0$, and the non-dimensional depth of the vehicle, respectively. The gray bold line shows the normalized Stokes drift profile.

two paragraphs follows from Amador et al. (2015) with minor modifications.

Field experiments were carried out near Mokuleia and at the Kilo Nalu Observatory (Pawlak et al., 2009), located on the north and south shores of Oahu, respectively. The location of the study sites and the bathymetry of the survey regions are shown in Figure 2.4. Currents are predominantly alongshore and vary semidiurnally on both reef systems. Observations at each site include a series of AUV surveys targeting the spatial structure of the flow field and water properties (temperature, salinity, optical backscatter). Each study site featured bottom-mounted, upward-looking four beam 1200 kHz RD Instruments Workhorse ADCPs deployed at depths in the range of 11 – 13 m and located within the AUV survey domain. The fixed ADCPs were programmed to sample in 0.25 m bins with a blanking distance of 0.5 m, and measured velocity profiles and bottom pressure at 1 Hz. Wave conditions for each set of observations were dominated by narrow-banded long-period swell with light winds and minimal short-period wave energy. The observations span a range of wave heights for which the theoretically predicted bias effects, $\overline{u}_{Lq}$, vary significantly. Key parameters have been summarized in Table 2.1.

AUV surveys consisted of mow patterns in both along- and cross-shore directions spanning a significant portion of the tidal cycle. To assess DVL performance, each survey included legs in opposite directions, measuring water velocities in close proximity to fixed-point current measurements gathered by upward looking ADCPs. REMUS DVLs were configured to sample in 1 m bins with a blanking distance of 1 m and a sampling frequency of approximately 0.67 Hz. The vehicle was programmed to maintain an average depth of 3 m and 2 m below the surface for the Kilo Nalu and the Mokuleia experiments, respectively, as described in Table 2.1. For all the experiments, the vehicle was set to cruise at a velocity of 2 m s^{-1}.

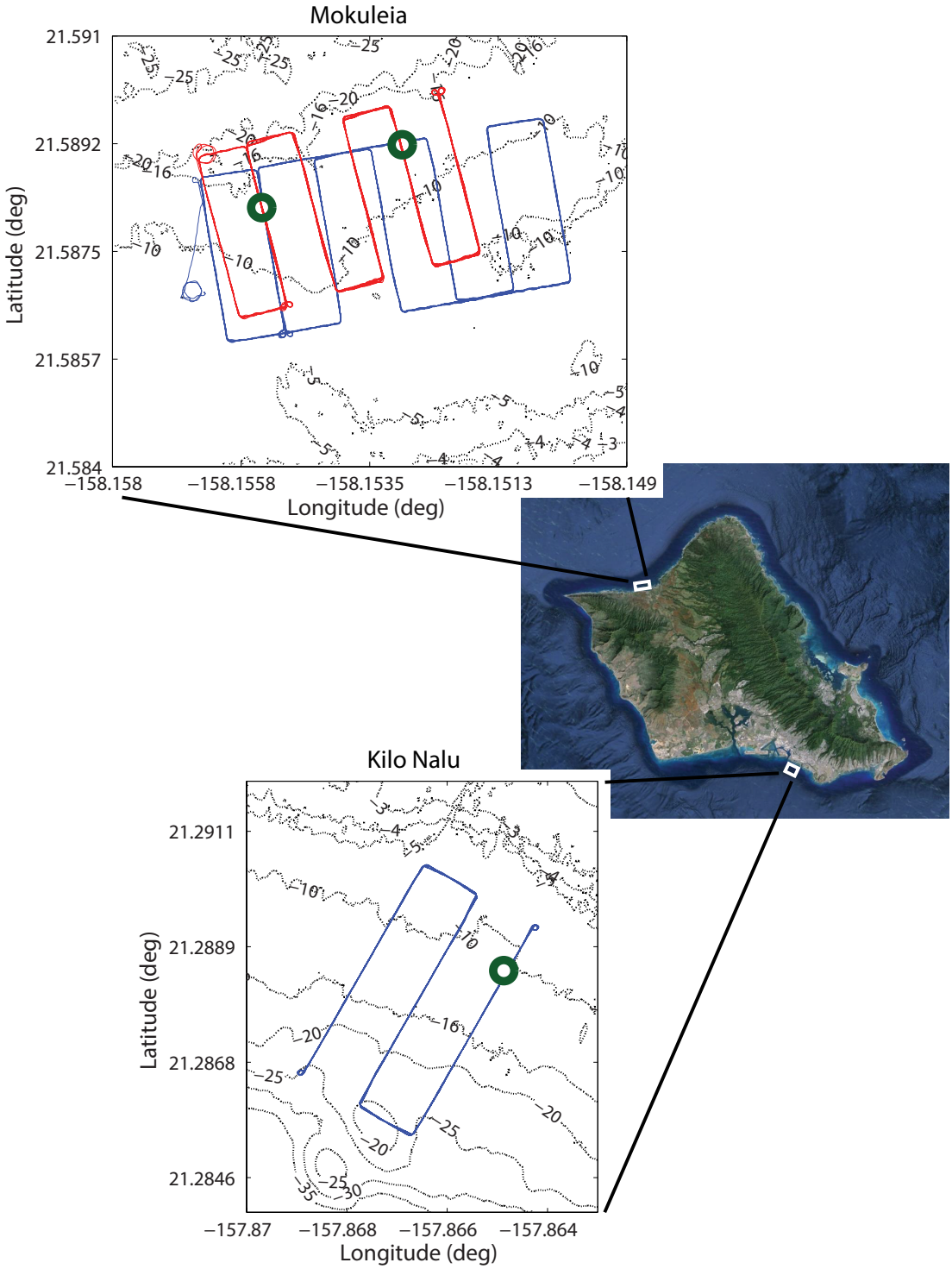

Figure 2.4: Study area and survey regions overlaid with LIDAR bathymetry. The red and blue lines show the tracks followed by the AUV during the hydrodynamic surveys. Bold green circles denote the location of the upward-looking fixed ADCPs.

Table 2.1: Local wave conditions and transect information.

Experiment	Deployment dates	H_{sig} (m)	T_p (s)	D_p (deg)	Number of transects	AUV orient. (deg)	AUV depth (m)	local depth (m)
Kilo Nalu I (cross-shore)	29 Jun 2010	0.8	11.4	206	7 shoreward 8 seaward	30 210	2.9	11.7
Kilo Nalu II (cross-shore)	06 Jul 2010	0.8	9.7	171	7 shoreward 8 seaward	30 210	2.9	11.3
Mokuleia I (cross-shore)	11 Dec 2010	1.2	11.2	349	8 shoreward 7 seaward	170 350	1.9	12.7
Mokuleia II (alongshore)	11 Dec 2010	1.3	11.0	351	8 upcoast 7 downcoast	79 261	1.9	13.0
Mokuleia III (cross-shore)	15 Dec 2010	1.3	12.2	346	7 shoreward 13 seaward	166 345	1.9	13.2
Mokuleia IV (cross-shore)	15 Dec 2010	1.4	12.7	345	7 shoreward 7 seaward	164 345	1.9	11.2
Mokuleia V (cross-shore)	17 Dec 2010	0.8	10.2	349	7 shoreward 13 seaward	162 345	1.9	12.8
Mokuleia VI (cross-shore)	17 Dec 2010	0.7	10.3	344	7 shoreward 7 seaward	164 345	1.9	10.9

2.3.1 Fixed ADCP data

To understand how the fixed ADCP averaging interval affects the analysis, we examined a series of depth-averaged, velocity realizations centered on AUV transect times. Figure 2.5a shows the root mean square deviation (RMSD) of depth averaged, non-dimensional velocity differences

$$\left(\frac{\overline{V}_{\bar{t}}-\overline{V}_{20}}{V_\sigma}\right)_{\text{RMSD}} = \sqrt{\frac{1}{N}\sum_{i=1}^{N}\left(\frac{\overline{V}_{\bar{t}}-\overline{V}_{20}}{V_\sigma}\right)_i^2}, \tag{2.11}$$

in the direction of wave propagation as a function of non-dimensional time, $\bar{t}/T_p$. Here, T_p represents the observed peak wave period for each 20 min window, $\bar{t}$ is a varying interval for time-averaging, $\overline{V}_{20}$ is the time-averaged velocity over a 20 minute interval, and N is the number of ensembles. Normalizing by the velocity standard deviation of each 20 minute realization (V_σ) accounts for the effects of varying wave conditions. The underlying assumption here is that for

Eulerian measurements (such as fixed ADCP measurements), a $\bar{t} = 20$ min averaging interval can effectively eliminate the influence of the wave velocities on the mean velocity.

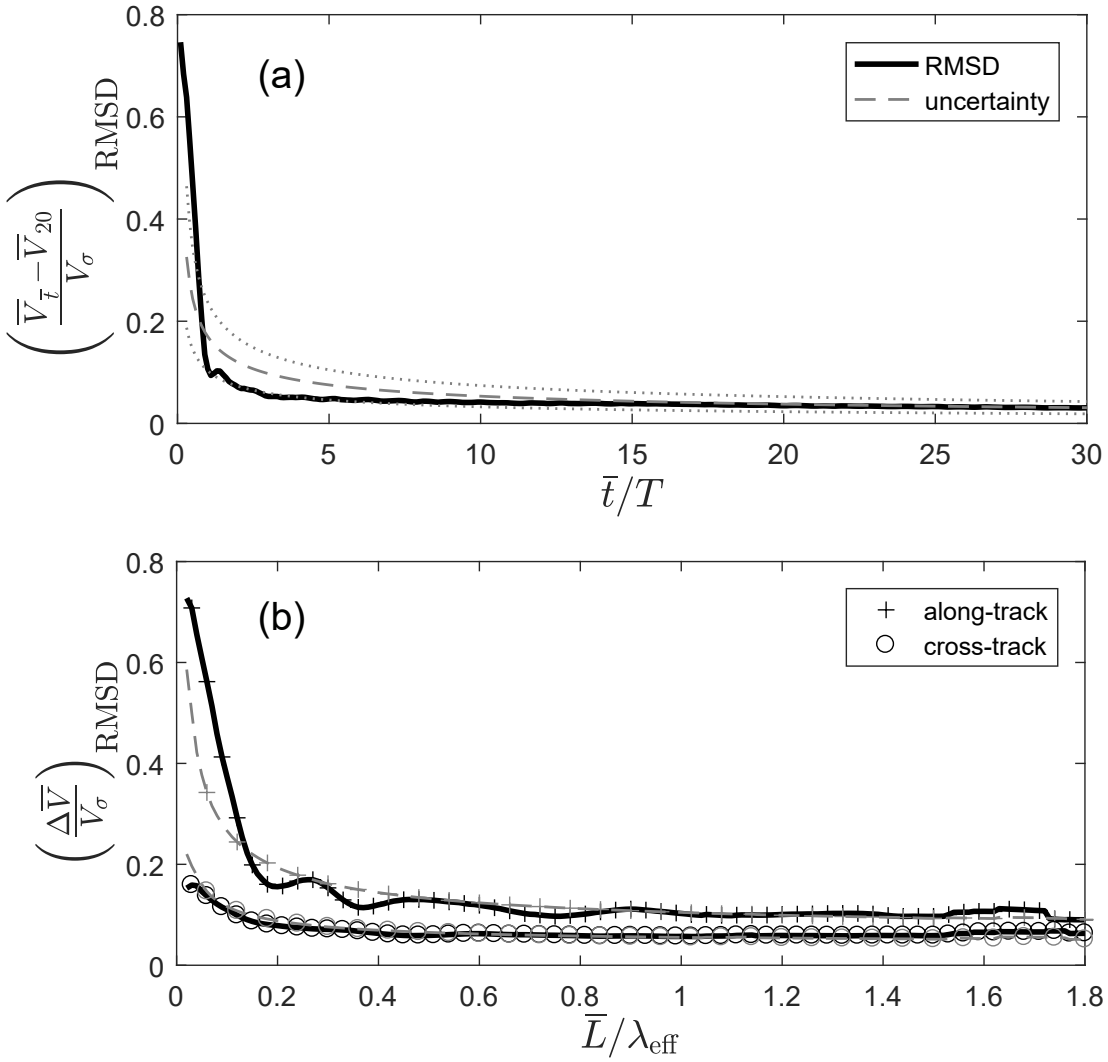

Figure 2.5: (a) Root mean square deviation (RMSD) of depth-averaged, fixed ADCP velocity differences, normalized by the wave velocity standard deviations (solid black line) and expected uncertainty estimates (dashed gray line) as a function of non-dimensional time, $\bar{t}/T_p$. Gray dotted lines delimit the standard deviation of the expected uncertainty estimates. (b) RMSD values of non-dimensional, depth-averaged velocity differences (solid black lines) and expected uncertainty estimates (dashed gray lines) for all cross-shore transects as a function of non-dimensional averaging length, $\overline{L}/\lambda_{\mathrm{eff}}$. Circles and crosses represent cross- and along-track quantities, respectively.

We further compare the RMSD values to estimates of the expected uncertainty in time-averaged, fixed ADCP velocity measurements in Figure 2.5a. Errors in the ADCP measurements

are expected to be normally distributed about the mean flow. The expected uncertainty is calculated as a wave-induced uncertainty normalized by the standard deviation of the velocity for each 20 minute realization. The wave-induced uncertainty is estimated by dividing the standard deviation of the velocity (dominated by wave motion for these data) for each time window by the square root of the effective degrees of freedom. Degrees of freedom are calculated using an estimated integral time scale following Emery and Thomson (1997). Note that the wave-induced uncertainty implicitly includes random instrument errors, which can be estimated by computing the standard deviation of the error velocity (single-ping error), and should decay with the square root of the number of measurements being averaged (RD Instruments, 1996).

Ideally, the ADCP averaging interval should be comparable to the AUV transect times (1 – 2 min) and should eliminate wave orbital velocities. As evidenced in Figure 2.5a, wave velocities are significantly suppressed within the first few wave cycles. We see that the expected uncertainty estimate (dashed gray line) captures the behavior of the RMSD values (solid black line), indicating that the observed deviations are adequately described by normally distributed measurement errors associated with random instrument noise and wave-induced uncertainties.

ADCP-derived velocity profiles used in our calculations were time-averaged over an interval of $\bar{t} = 10T_p$ ($\sim$ 1.5 – 2.5 min). Here, random instrument errors are negligible in the uncertainty estimate because wave velocities ($V_\sigma \sim 12 - 25$ cm s^{-1}) are an order of magnitude greater than the ADCP single-ping error (~ 2 cm s^{-1}), and because the effective number of degrees of freedom is always less than the number of measurements. Based on this analysis, we expect fixed ADCP errors to be in the range of ~ 0.7 cm s^{-1} to ~ 2 cm s^{-1}, depending on wave conditions.

2.3.2 AUV data

AUV-based velocity measurements rely on spatio-temporal averaging to reduce noise and to obtain useful estimates of the current velocities. However, it is not immediately clear

what the adequate averaging length should be, especially when averaging under the influence of non-monochromatic waves. To examine the effects of spatial averaging, depth-averaged velocity differences ($\Delta\overline{V} = \overline{V}_{\mathrm{AUV}} - \overline{V}_{\mathrm{ADCP}}$) were calculated in a cross- and along-track reference frame and as a function of the averaging length ($\overline{L}$). We focus below on the standard deviation and the expected uncertainty of these velocity differences over multiple transects to identify an optimal averaging length. It should be noted that the averaging length is limited by total transect length and that velocities calculated over very long averaging lengths may suffer from changes due to spatial variability.

Figure 2.5b shows the RMSD of depth averaged, non-dimensional velocity differences

$$\left(\frac{\Delta\overline{V}}{V_\sigma}\right)_{\mathrm{RMSD}} = \sqrt{\frac{1}{N}\sum_{i=1}^{N}\left(\frac{\Delta\overline{V}}{V_\sigma}\right)_i^2}, \tag{2.12}$$

in solid black lines and estimates of the total expected uncertainty in dashed gray lines for all cross-shore transects, N, as a function of non-dimensional averaging length, $\overline{L}/\lambda_{\mathrm{eff}}$. The effective wavelength, λ_{eff}, was calculated for each transect using the corresponding Doppler shifted peak wave frequency. ADCP-derived, time-averaged velocities ($\overline{V}_{ADCP}$) and standard deviations (V_σ) were calculated for each transect over an interval of 10 peak wave periods. As noted in section 2.3.1, normalizing by the ADCP-derived standard deviations accounts for the effects of varying wave conditions.

The total expected uncertainty is calculated as the square root of the sum of the squares (RSS) of the fixed ADCP measurement uncertainty (over 10 wave periods) and the AUV measurement uncertainty, normalized by the wave velocity standard deviation. Similar to the fixed ADCP uncertainty, the AUV measurement uncertainty implicitly includes random DVL errors, and is similarly calculated as the wave-induced uncertainty divided by the square root of the effective number of degrees of freedom. Again, the wave-induced uncertainties are typically one order of magnitude greater than random DVL errors because the velocity standard deviations

(~ 10 – 26 cm s^{-1}) measured by the AUV are significantly larger than DVL single-ping errors (~ 4 cm s^{-1}), and the effective number of degrees of freedom is always less than the number of measurements.

As seen in Figure 2.5b, the RMSD and the expected uncertainty of the along-track velocity differences decay within one effective wavelength ($\overline{L} \sim \lambda_{eff}$), consistent with the reduction of wave-induced velocities via spatial averaging. Note that both the RMSD values and the expected uncertainty of the velocity differences are significantly lower in the cross-track direction because, for cross-shore transects, the wave field is generally aligned in the along-track direction. Furthermore, the RMSD values of the cross- and along-track differences level off as the relative averaging length increases, indicating a "minimum uncertainty" in our measurements. This feature, whose minimum is bounded by the fixed ADCP measurement uncertainty (at 10 peak wave periods), is also captured by the expected uncertainty estimate, suggesting that normally distributed measurement errors associated with wave-induced uncertainties are responsible for the observed behavior. In addition, we note that spatial variations due to shear and turbulence along the vehicle track may play a more prominent role in the measurement uncertainty with increasing averaging lengths, as progressively larger scales begin to affect the RMS velocities.

Based on this analysis, AUV-based velocity profiles were calculated over an averaging length, $\overline{L}$, equivalent to the effective wave length, λ_{eff}. The effective wavelength ranged from ~ 110 m to ~ 180 m, depending on the velocity of the AUV relative to the waves and the local conditions. The estimated uncertainties ranged from ~ 1.8 cm s^{-1} to ~ 4.5 cm s^{-1} per transect for the along-track velocity differences and ~ 0.8 cm s^{-1} to ~ 1.5 cm s^{-1} per transect for the cross-track velocity differences in cross-shore transects. AUV-based velocity profiles were obtained using the downward-looking DVL, and centered at fixed ADCP locations (within ~ 10 m) in all data sets.

2.3.3 Wave spectra

The wave-induced bias calculated in (2.10) for monochromatic waves can be more accurately calculated considering a spectral distribution of the wave field ($S_{\eta\eta}$), so that the quasi-Lagrangian velocity is rewritten as

$$\overline{u}_{Lq} = \int_{f_a}^{f_b} \int_{\theta_a}^{\theta_b} k \frac{\sigma^2}{\omega} \frac{\cosh\left(2k(Z_0+h)+k\Delta z\right)}{\sinh^2(kh)} S_{\eta\eta}\, \mathrm{d}\theta \mathrm{d}f, \tag{2.13}$$

where

$$\int_0^{\infty} \int_{-\pi}^{\pi} S_{\eta\eta}(f,\theta)\, \mathrm{d}\theta\, \mathrm{d}f = \langle \eta^2 \rangle, \tag{2.14}$$

and $\langle\,\rangle$ is an ensemble-averaging operator. Here, $f_a = 0.03$ Hz and $f_b = 0.5$ Hz represent the limits of the sea-swell frequency band under consideration; θ defines the direction of wave propagation; and $\theta_b - \theta_a = \pi/3$, centered on the transect mean orientation. The Extended Maximum Entropy Method (EMEP) (Hashimoto, 1997) was used to estimate directional wave spectra from fixed ADCP data (10 min pressure and velocity time-series).

2.4 Analysis and results

To investigate bias errors in AUV-based measurements, spatially-averaged ($\overline{L} = \lambda_{eff}$) velocity profiles were calculated using downward-looking DVL data and rotated into along- and cross-track components for each transect (Amador et al., 2015). ADCP-derived velocity profiles were time-averaged ($\overline{t} = 10T_p$) and also rotated into along- and cross-track components. Velocity differences ($\Delta V = V_{\mathrm{AUV}} - V_{\mathrm{ADCP}}$) were calculated over a range of depths above the fixed ADCPs first range cell, and excluded regions near boundaries (11% of range to boundary) to avoid acoustic sidelobe interference issues. The wave-induced bias ($\overline{u}_{Lq}$) was calculated using a fixed ADCP-derived directional spectrum as described in section 2.3.3.

We focus below on an example drawn from two sets of transects gathered at the Mokuleia

study site on December 11, 2010. Figure 2.6 shows ensemble-averaged velocity differences ($\langle \Delta V \rangle = \langle V_{\mathrm{AUV}} - V_{\mathrm{ADCP}} \rangle$) for 14 cross-shore (a-b) and 14 alongshore (c-d) transects. The expected wave-induced bias ($\overline{u}_{Lq}$), calculated using (2.13), has also been plotted here for reference.

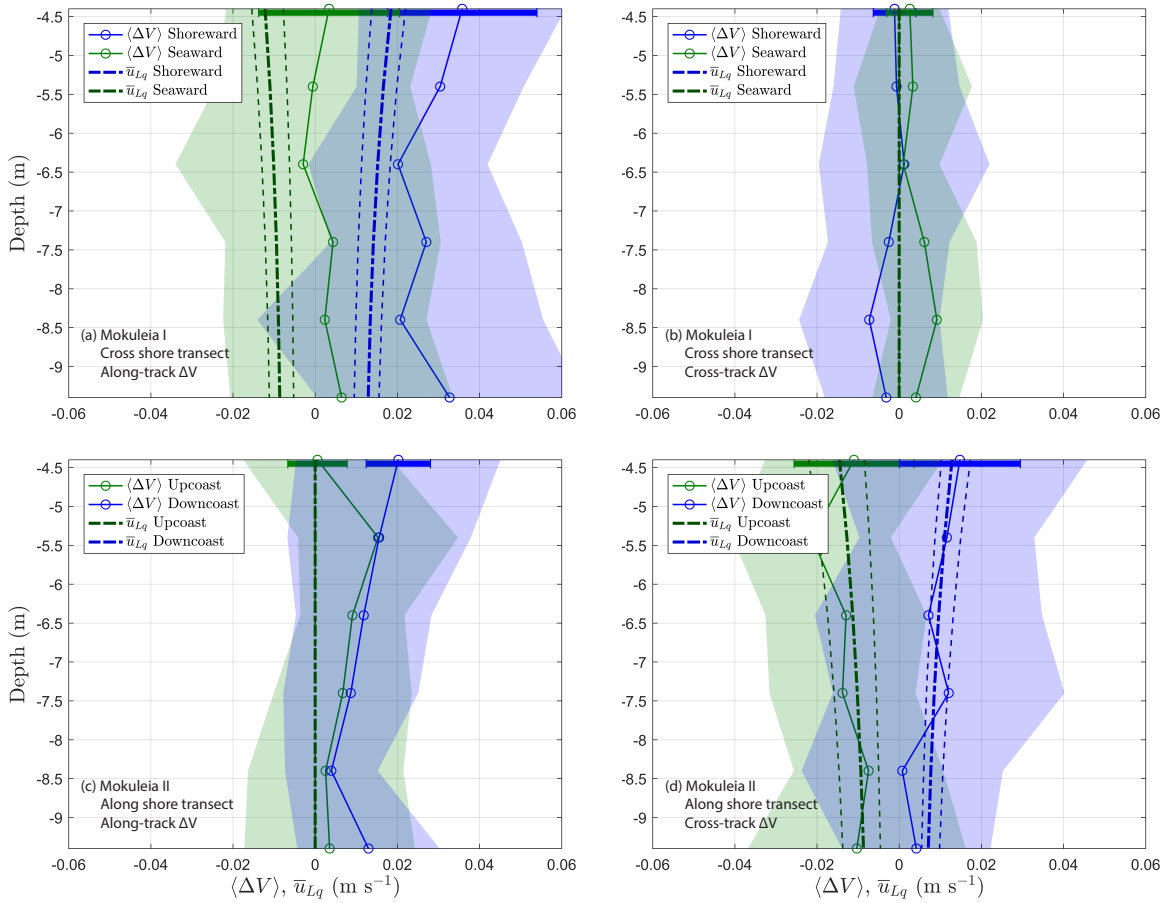

Figure 2.6: Ensemble-averaged velocity differences ($\langle \Delta V \rangle = \langle V_{\mathrm{AUV}} - V_{\mathrm{ADCP}} \rangle$), and wave-induced bias ($\overline{u}_{Lq}$) on a cross- and along-track reference frame. Shaded error bands represent one standard deviation of the velocity difference, and solid error bars at the top of each profile indicate the calculated uncertainties (similar at all depths) in the ensemble-averaged profiles. Thin dashed lines capture the range of values used when calculating $\overline{u}_{Lq}$ for each individual transect.

Considering the effects of a wave-induced bias only, we anticipate that $\langle \Delta V \rangle \approx \pm \overline{u}_{Lq}$ when the measured velocity component is aligned with the direction of wave propagation. Here, the relative wave direction determines the sign of $\overline{u}_{Lq}$. The wave-induced bias should be zero for velocity components that are perpendicular to the direction of wave propagation.

The top panels in Figure 2.6 show the observed velocity differences for (a) along- and (b) cross-track components in cross-shore transects. For the shoreward legs, the observed along-track ΔV profiles (Figure 2.6a) show a positive bias that exceeds the predicted wave-induced bias. The seaward legs exhibit a weaker, slightly positive bias. A comparison between the measured and the expected values (dashed lines in Figure 2.6a) reveals that both ΔV profiles lie to the right of the theoretical prediction. In other words, REMUS-based velocity measurements show a bias in the direction of vehicle motion relative to the wave-induced bias; we refer to this deviation as the forward residual bias ($V_{\text{res}} = \Delta V - \overline{u}_{Lq}$). As expected, the observed cross-track velocity differences (Figure 2.6b) in both shoreward and seaward transects do not show an appreciable bias. Vector diagrams in Figure 2.7a illustrate the observed velocity differences (ΔV) in cross-shore transects as vector sums of the wave-induced ($\overline{u}_{Lq}$) and residual (V_{res}) velocities.

The bottom panels in Figure 2.6 show the observed (c) along- and (d) cross-track velocity differences in alongshore transects. Measurements of cross-track ΔV for alongshore transects (Figure 2.6d) are well predicted by the theoretical model with wave-induced biases appearing in the direction of wave travel for both upcoast (westward for Mokuleia) and downcoast transects (eastward for Mokuleia). For the along-track velocity component (Figure 2.6c), however, a forward bias appears for both transect directions that is unaccounted for by wave bias theory. Vector diagrams again summarize the contributions of the wave-induced and forward residual biases for the alongshore transects in Figure 2.7b.

The results observed in Figure 2.6 are representative of experiments conducted in a range of current and wave conditions (see Table 2.1) at both field sites. Figure 2.8 shows depth-averaged velocity differences as a function of the theoretical cross-track, depth-averaged wave-induced bias for all cross-shore transects considered in this study. Gray dots and black crosses illustrate individual transects and mission ensemble-averages, respectively. The black dashed line in Figure 2.8a depicts a one-to-one relationship ($\Delta\overline{V} = \overline{u}_{Lq}$), for reference. On the left panel (Figure 2.8a), we see that the ensemble-averaged data points lie above the one-to-one relationship

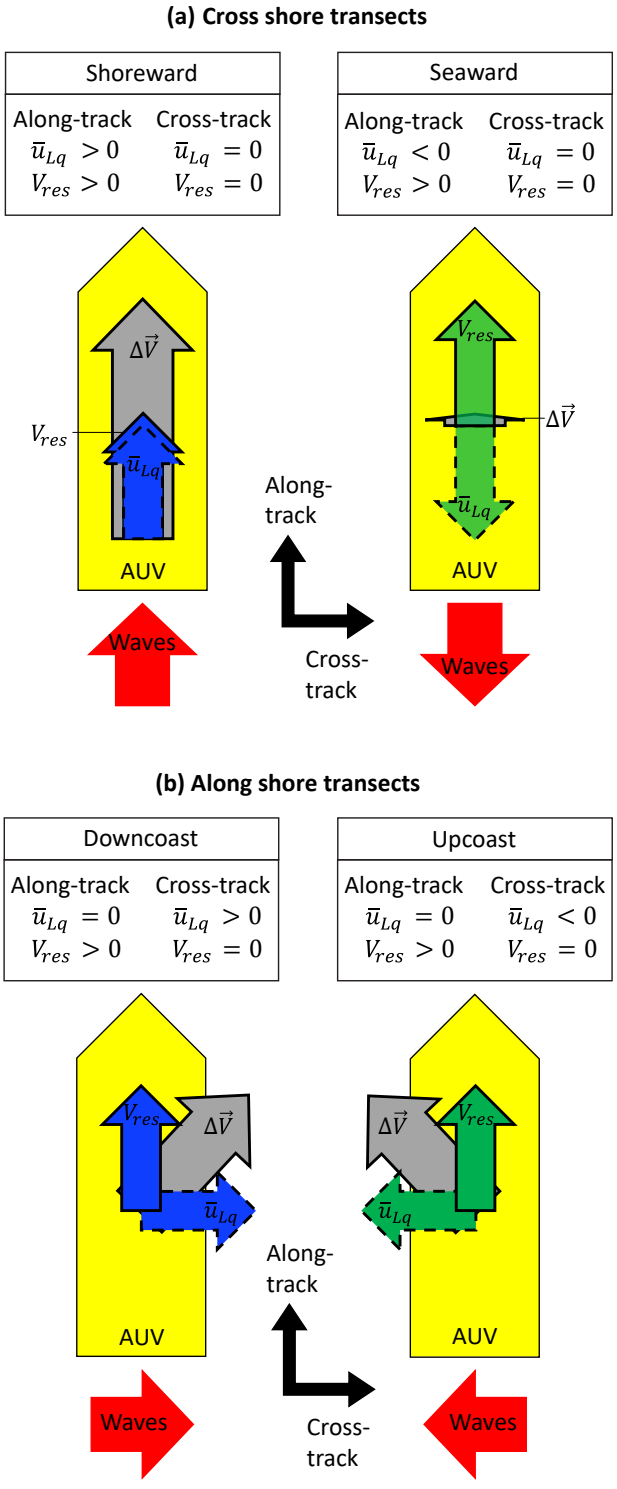

Figure 2.7: Observed velocity difference vector ($\Delta\vec{V}$) and bias components ($\overline{u}_{Lq}$, V_{res}) in a cross- and along-track reference frame for (a) cross- and (b) alongshore transects. Bias velocity components are shown in blue (shoreward and downcoast legs) and green (seaward and upcoast legs) as in Figure 2.6.

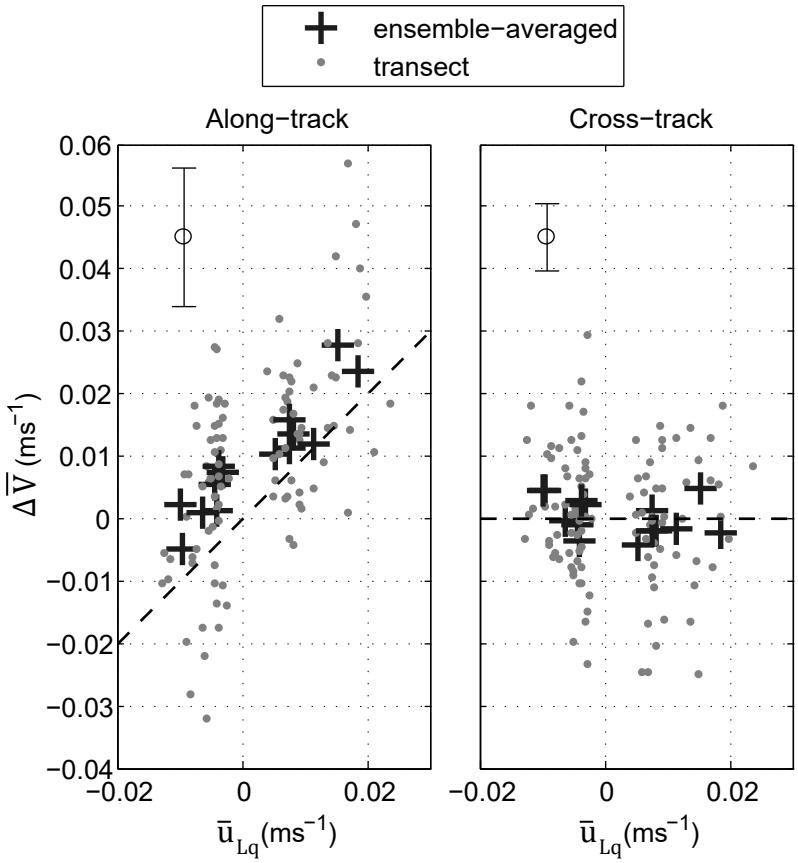

Figure 2.8: Depth-averaged velocity differences ($\Delta\overline{V}$) as a function of the expected cross-track, depth-averaged wave-induced bias ($\overline{u}_{Lq}$) for all cross shore transects considered in this study. Vertical error bars at the top left corner represent the average along- and cross-track uncertainty estimate of all ensembles.

(i.e., along-track velocity differences exceed the theoretically expected values). In contrast, the right panel (Figure 2.8b) shows the cross-track velocity differences for all cross-shore transects. In spite of the scatter in individual measurements, it is evident that the average cross-track velocity differences in both shoreward and seaward transects do not show an appreciable bias.

2.5 Discussion

The theory presented here describes the motion of a vehicle within a spectral wave field and the implications of quasi-Lagrangian dynamics on AUV-based velocity measurements. The

resulting effect is related to Stokes drift, but is modified by the vehicle's velocity relative to the wave speed. In this case, the wave-induced motions lead to vertical oscillations of the AUV and of the DVL sampling volumes, with preferential sampling of the crest regions; this results in a velocity bias in the direction of wave propagation. Observations show significant biases that are dependent on relative wave direction, in agreement with the predictions of the theory, but also reveal the presence of a persistent offset in the direction of vehicle motion. This residual forward bias is consistent with observations in other studies (e.g., Fong and Monismith, 2004; Fong and Jones, 2006; Jaramillo and Pawlak, 2010), which have also reported a forward velocity bias in both AUV and shipboard measurements even in the absence of waves.

The clearest illustration of the residual bias ($V_{\text{res}} = \Delta V - \overline{u}_{Lq}$) is apparent in the along-track, alongshore velocity shown in Figure 2.6c. Here, the wave direction is perpendicular to the vehicle track, and the residual velocity is persistently in the direction of vehicle motion (along-track positive for all plots in Figure 2.6). Furthermore, results in Figure 2.8 confirm the presence of a residual bias that is independent of the relative wave direction. We can conclude, therefore, that the forward residual bias is associated with a separate process independent of the wave-induced bias described by the theory.

2.5.1 Forward residual bias

The residual bias in the direction of vehicle motion warrants a closer inspection of the bottom tracking velocity estimates. An underestimation of the vehicle velocity by the bottom tracking system could lead to the observed forward velocity bias in th e along-track velocity measurements. This was examined and dismissed by Fong and Monismith (2004) by comparing bottom tracking velocities with RTK GPS position estimates. Here, because the vehicle is submerged, GPS positioning is not available. Bottom track velocities were compared with velocities derived from the LBL navigation system, following Joyce (1989). Averaged over transects, differences between bottom tracking and LBL velocities showed no correlation

with transect averaged velocity differences, ΔV, indicating that bottom tracking errors are not responsible for the observed biases.

The forward residual bias is shown in Figure 2.9 as a function of the vertical distance from the vehicle (range) based on an ensemble-average of along-track velocity differences for the entire data set. Although the scatter is notable, the profile shows a bias of ~ 1 cm s^{-1} that is fairly uniform with distance from the transducer, over the range considered. It is possible that acoustic "ringing" of the DVL mount may be responsible, at least in part, for the observed residual bias. Ringing occurs when the transmitted pulse excites the transducer head and causes it to resonate at the transmit frequency. The DVL then processes both the return signal from the water and the ringing signal biasing the velocity data in the direction of the vehicle motion. In this case, one would expect a forward residual bias that is proportional to the vehicle velocity.

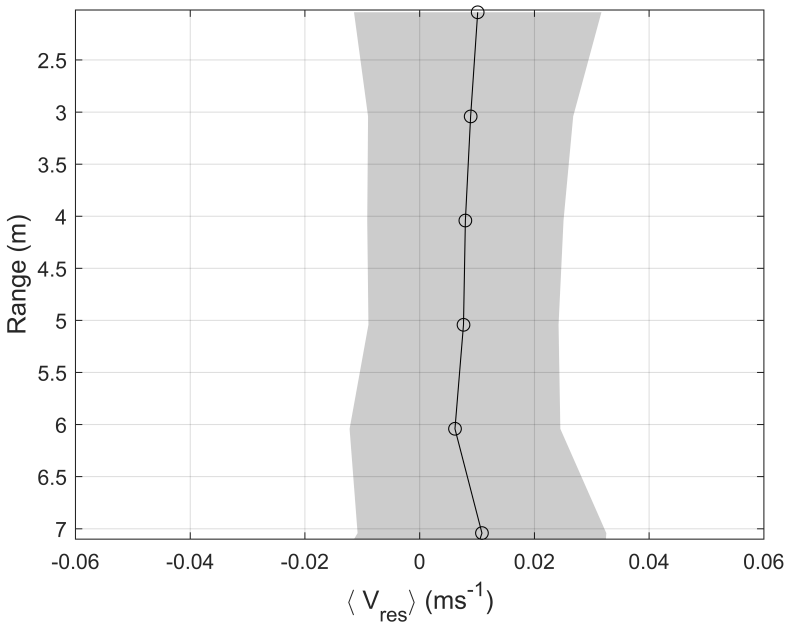

Figure 2.9: Average residual bias obtained by removing the wave-induced bias from the along-track velocity differences ($\langle V_{\rm res}\rangle = \langle \Delta V - \overline{u}_{Lq}\rangle$). The sample standard deviation is shown by the shaded region.

Conclusive confirmation of the source for the residual bias would require extensive additional surveys to be conducted at varying vehicle speeds and in greater depths in order to

resolve a dependence on platform velocity over a longer profile. With a relatively narrow range of practical cruising speeds (1 – 2 m s^{-1} for the REMUS-100), a large number of repeated transects would be needed at each speed to sufficiently reduce measurement uncertainties. For the present data set, it was not possible to verify acoustic ringing as an explanation for the additional bias, since vehicle speeds were maintained at 2 m s^{-1}. Acoustic ringing effects are expected be intensified near the transducer which should lead to a decaying bias profile. For the low backscatter tropical reef environment, the decay rate would likely be weaker, however.

In addition to ringing and bottom tracking errors, a velocity bias error can occur due to a misalignment between the DVL and the forward axis of the vehicle. Misalignment errors, estimated following Joyce (1989), were found to be negligible. Other potential sources for error in ADCP measurements include spatial and temporal variations in velocity (shear, turbulence, waves), errors in instrument orientation (pitch, roll, heading), side lobe interference, variations in sound speed, Doppler noise, velocity ambiguity errors, and timing errors (González-Castro and Muste, 2007). These error sources were dismissed as sources of persistent bias since they either contribute to random error or they are not applicable to the AUV configuration.

2.5.2 Additional comments

The analysis of the wave-induced bias assumes that the AUV follows the wave motion closely, neglecting any relative inertia. In reality, AUV motion will deviate from the wave motion for higher frequencies. A comparison of pressure spectra measured by the vehicle and the fixed ADCPs for the observations presented earlier indicated that the vehicle follows closely the dominant motions produced by the spectral wave field. Field data shows that the dominant spectral energy content was typically confined to a narrow band within the range of 10 s $\lesssim T \lesssim$ 15 s for all observations. Shorter period wave energy was minimal, although the analysis reveals that the vehicle begins to deviate from the wave motions for wavelengths smaller than around 60 m ($\lambda \approx 60$ m, $T \approx 7$ s, for $h \approx 11$ m), suggesting that the vehicle's inertia will play a role in partially

filtering the higher frequency waves.

Although small $O(1–5)$ cm s^{-1}, the wave-induced and residual biases are not inconsequential and can be comparable to water velocities associated with steady and low-frequency flow features. For example, bias errors may be significant when measuring cross-shore exchange flows and attempting to resolve the spatial structure of vortical features in the inner shelf, where flow speeds may be on the order of 1–10 cm s^{-1}. Also, velocity biases may affect the measurement of horizontal velocity shears, complicating the calculation of flow parameters such as vorticity, salt and momentum fluxes, and the Richardson number (Fong and Monismith, 2004).

In principle, the wave induced bias can be corrected, provided that the in situ wave field is known. Here, we only provide wave-induced bias estimates based on directional wave spectra measured by bottom-mounted, fixed ADCPs in close proximity to the AUV and over a time window that exceeds the AUV averaging time. However, recent work by Haven and Terray (2015) has shown that it is possible to measure sea surface spectra and mean wave direction from an underway AUV equipped with an on-board ADCP and inertial sensors. This new capability could provide a more accurate way to measure and correct for the wave-induced bias in AUV-based measurements, with the additional advantage of being independent of supplementary wave information. In the absence of field measurements, modeled wave conditions can provide an estimate of the sea surface spectra.

2.6 Summary

The trajectory for a small AUV moving under surface waves can be altered due to the interactions between the vehicle and the wave field. These changes in trajectory introduce a quasi-Lagrangian bias in AUV-based velocity measurements that is related to Stokes drift.

Here, we have developed a theoretical framework to describe the motion of the AUV within a spectral wave field based on a first order expansion of the linear wave solution. Using

this framework we quantify the wave-induced bias as a function of the local wave conditions, and the vehicle's depth and velocity. The analysis shows that the vehicle's velocity relative the wave phase speed acts to enhance or suppress the bias mechanism by modifying the vehicle's vertical excursions and its relative spatiotemporal sampling of trough versus crest regions.

Theoretical predictions are in good agreement with observations from AUV surveys carried out in conjunction with current velocity measurements from bottom mounted ADCPs. AUV-based velocity profiles were calculated over an averaging length equivalent to the effective wave length ($\lambda_{\text{eff}} \sim 110$ – 180 m) and compared with time-averaged ($10T_p \sim 1.5$ – 2.5 min), fixed ADCP measurements. Ensemble-averaged velocity differences ($\langle \Delta V \rangle = \langle V_{\text{AUV}} - V_{\text{ADCP}} \rangle$) calculated in a cross- and along-track reference frame, and obtained in a range of wave conditions confirm the presence of a wave-induced bias consistent with theory but also reveal an additional, persistent bias in the direction of the vehicle motion that is unaccounted for by wave effects. It is speculated that the unexplained residual may be associated with acoustic ringing effects. Together, the bias errors are comparable in magnitude to steady flow velocities for inner shelf regions and thus must be considered for AUV-based measurements in these environments.

2.7 Acknowledgments

This work was carried out with funding from the Office of Naval Research, via awards N00014-13-1-0340 and N00014-12-1-0221. The authors would like to express their sincere thanks to Mark Merrifield, Carly Fetherolf, Chris Kontoes, Chris Colgrove and Kimball Millikan for their assistance with field operations in support of the work described here. Eugene Terray provided valuable feedback in the development of the theoretical model. The manuscript also benefited from the helpful suggestions of three anonymous reviewers. A preliminary version of the work described here was originally presented at the IEEE/OES 11th Current, Waves and Turbulence Measurement Workshop (CWTM) held in St. Petersburg, Florida, 3 March 2015 and

appeared in the unrefereed conference proceedings (Amador A., Pawlak G., and Jaramillo S., 2015).

The present Chapter, in full, is a reprint of published work featured in the Journal of Atmospheric and Oceanic Technology (Amador A., Jaramillo S., and Pawlak G., 2017). The dissertation author was the primary investigator and author of this paper.

Chapter 3

ADCP-based Estimates of Lateral Turbulent Reynolds Stresses in Wavy Coastal Environments

3.1 Introduction

Accurate estimation of the turbulent Reynolds stresses is essential for quantifying coastal ocean dynamics and mixing. Turbulence plays a key role in the transport of momentum, mass and heat, and affects a range of coastal processes including oceanic bottom boundary layer dynamics (Trowbridge and Lentz, 2018), wave dissipation, and nearshore circulation (Brink, 2016). Enhanced mixing of nutrients due to turbulent processes also contributes to the health of the coral reef benthic community (Baird and Atkinson, 1997; Atkinson et al., 2001; Monismith, 2007), to the dispersal and distributions of biological material (Jones et al., 2009; Sevadjian et al., 2010), and has important implications for nearshore water quality.

Vertical profiles of Reynolds stresses can be obtained from ADCPs using the variance method (Lohrmann et al., 1990; Stacey et al., 1999a) which makes use of the difference of

along-beam velocity variances. In the coastal ocean, however, the effects of surface gravity waves complicate the measurement of the turbulent stresses. This is because the oscillating wave velocities are typically orders of magnitude larger than the turbulent fluctuations, and often occur in the same frequency band as the stress-carrying turbulent motions (Trowbridge, 1998; Trowbridge and Elgar, 2001; Kirincich and Rosman, 2011). Thus, small uncertainties in sensor tilt or the effects of a sloping bottom can introduce velocity correlations that dominate the covariance spectrum, potentially biasing the Reynolds stress estimates (Trowbridge, 1998). Moreover, unsteady advection of turbulence by wave orbital motion can alter the shape of the observed frequency cospectrum by aliasing lower frequency turbulent energy into the wave band (Lumley and Terray, 1983; Gerbi et al., 2008; Rosman and Gerbi, 2017; Trowbridge et al., 2018). This leads to an apparent decrease in the observed spectral density in frequencies below the wave band, and also results in biased stress estimates.

A variety of wave-turbulence decomposition techniques have been proposed to estimate turbulent fluxes in the presence of waves (e.g., Trowbridge, 1998; Shaw and Trowbridge, 2001; Feddersen and Williams, 2007; Bricker and Monismith, 2007; Gerbi et al., 2008; Bian et al., 2018). For instance, velocity differencing (e.g., Trowbridge, 1998) and adaptive filtering (e.g., Shaw and Trowbridge, 2001; Rosman et al., 2008) strategies use adjacent velocity measurements to remove wave biases from the Reynolds stress signal. These methods assume that wave velocities are correlated or coherent over spatial scales that are much larger than those associated with turbulent fluctuations; hence, motions that correlate between the measurements are assumed to be due to waves, while motions that do not correlate are attributed to turbulence. On the other hand, cospectra-fit (CF) methods (e.g., Gerbi et al., 2008; Kirincich et al., 2010) fit a semi-empirical model of boundary layer turbulence derived by Kaimal et al. (1972) to the observed cospectrum at frequencies smaller than those of surface gravity waves to estimate the turbulent stresses. While originally developed for acoustic Doppler velocimeters (ADVs), these techniques have been successfully adapted for ADCP measurements (e.g., Whipple et al., 2006; Rosman et al., 2008;

Kirincich et al., 2010); thus, extending the applicability of the variance method to enable vertical Reynolds stress estimates in wavy environments.

Research on wave-bias removal from turbulence estimates has been mostly limited to observations of vertical momentum fluxes ($\overline{u'w'}$ and $\overline{v'w'}$). In contrast, there has been little discussion about the turbulence statistics associated with the lateral momentum fluxes ($\overline{u'v'}$) in the nearshore and inner shelf literature. For coastal flows, it is generally assumed that the horizontal length scales are much larger than the vertical length scales (Burchard, 2002; Burchard et al., 2008); thus, the horizontal gradients of the turbulent fluxes are often neglected. As a result, lateral mixing processes may not be represented accurately in fine-scale coastal ocean models and are unlikely to be resolved in larger scale models. Coastal boundaries, however, require further attention as spatial gradients in bottom roughness and water depth (bottom drag) can lead to substantial cross-shore shear in the alongshore flow, and hence to enhanced turbulent mixing and lateral transport (Brink, 2016). At present, direct measurements of inner shelf turbulence are scarce, and the role of the lateral turbulent stresses in cross-shelf transport is not well understood.

The work presented here aims to offer new insights into the temporal variability and vertical structure of the lateral Reynolds stresses in tidally-dominated coral reef environments. In this paper, we describe and evaluate a new approach based on the variance method to estimate lateral Reynolds stresses from ADCP-based velocity observations in the presence of surface gravity waves. The proposed method uses a variation of Kirincich et al.'s (2010) procedure for isolating the turbulent motions at frequencies lower than those of surface waves. The performance of the proposed method is assessed by comparing the ADCP-based Reynolds stress estimates with ADV-based estimates. The experimental data used in this study were collected at the Makua reef on the western coast of O'ahu, Hawai'i (Figure 3.1) in tidally-driven, unstratified flow under moderate swell conditions.

The work here is presented as follows. The observations and methods are introduced in section 3.2 including a detailed description of the proposed ADCP-based stress calculation

method. In section 3.3, we take an ensemble averaged view of the turbulent properties of the flow. The phase ensemble averaging procedure is described first (section 3.2.4), followed by an inspection of ensemble-averaged turbulent cospectra (section 3.3.1) and of the associated turbulent length scales (section 3.3.3). We then evaluate the performance of the proposed method by comparing results with ADV measurements, and characterize the vertical structure of the turbulent Reynolds stresses as a function of tidal phase (section 3.3.4). Three simple eddy viscosity models for the lateral Reynolds stress component are proposed and tested (section 3.3.5). Potential limitations of the proposed method and implications for cross-shore turbulent transport are discussed in section 3.4.

3.2 Materials and procedures

3.2.1 Field deployment

Field observations were carried out offshore of Makua (21.510°, -158.236°) on the west coast of O'ahu, Hawai'i (Figure 3.1) in September 2013. The study specifically targeted the resolution of flow hydrodynamics over the forereef region in varying wave and current conditions. Field data from fixed instrumentation were collected as described in Arzeno et al. (2018) (see also Chapter 4). A brief summary of the field experiment is presented next.

Isobaths at the Makua forereef are oriented roughly north-south and aligned with the coastline. Bathymetry features a low slope region extending to about 600 m from the shoreline with an average depth of 6 m, and a fairly constant cross-shore seafloor slope of about 3.5% between the 6 and 24 m isobaths; beyond this limit, the coral reef shelf drops off sharply in the offshore direction. The Makua forereef exhibits generally periodic, shore-normal spur and groove formations between the 6 and 16 m isobaths. The bottom substrate is primarily composed of rough reef interspersed with pockets of sandy coral rubble and scattered patches of coral colonies.

Two 1200 kHz Teledyne RD Instruments (RDI) Workhorse ADCPs were deployed on

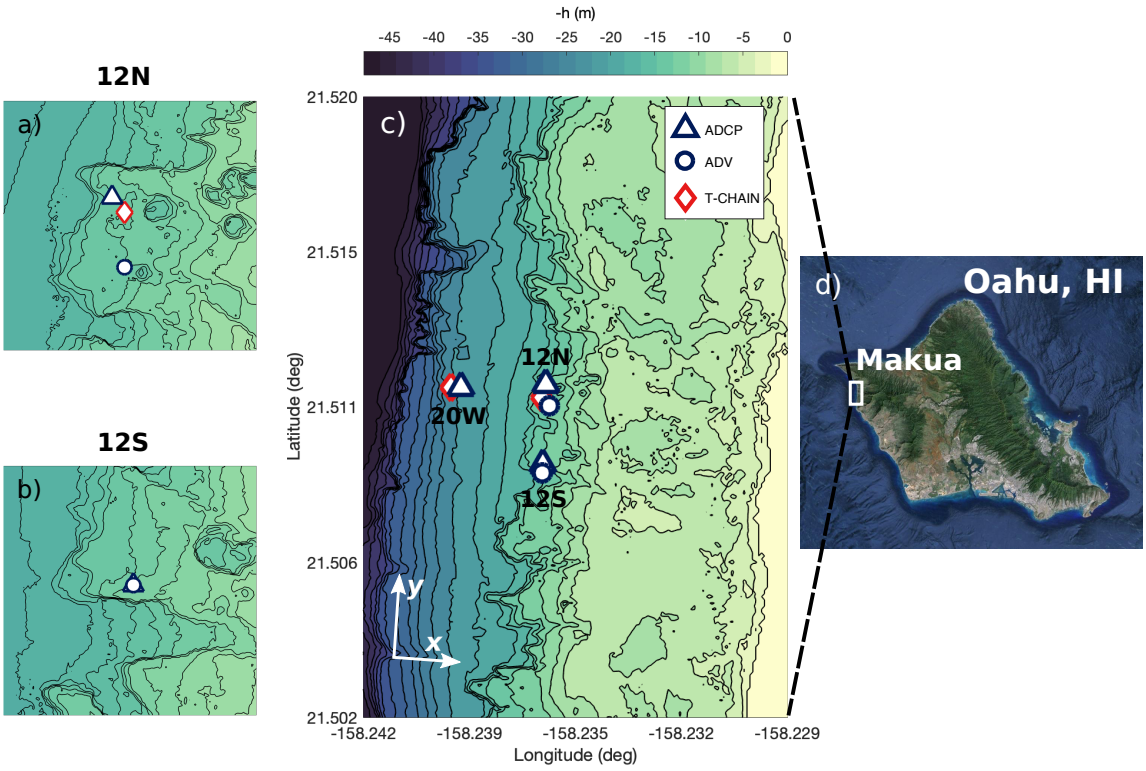

Figure 3.1: (a) 12N mooring, (b) 12S mooring, (c) Makua study site and instrument array with LIDAR bathymetry, and (d) satellite image (Google Earth) of O'ahu, Hawai'i. The notations 12N, 12S, and 20W denote the location (i.e., north, south, west) of the observational array near the 12 m and 20 m isobaths. The coordinate system (x, y) defines the cross- and alongshore directions, respectively, and is roughly aligned with the principal axis of the flow.

rigid frames near the 12 m isobath (Figure 3.1) to resolve the velocity fluctuations associated with the forereef turbulent flow. These bottom-mounted ADCPs (hereafter referred to as 12N and 12S) were moored about 260 m apart, and configured to sample in 0.25 m bins with a blanking distance of 0.8 m and a sampling frequency of 0.5 Hz using water sampling mode 12 (fast ping mode). Both 12N and 12S y (3–4 beam) axes were nearly aligned with the principal axis of the depth-averaged flow, and leveled with respect to the local bathymetry (Table 3.1). A third 300 kHz ADCP (hereafter referred to as 20W) was deployed roughly 270 m offshore of 12N near the 20 m isobath (Figure 3.1), and was configured to sample water velocities at 0.5 Hz in 1.25 m bins with a blanking distance of 3.25 m. ADCPs were programmed to record pressure at the bed and raw velocities in beam coordinates continuously, so that Reynolds stress estimates could be computed during post-processing. Thermistor chains (T-chains) located near the 12N and 20W ADCPs (Figure 3.1) measured temperature at 2 Hz from 0.30 m above the bed to 1 m below the surface in 1 and 2 m intervals, respectively. Table 3.1 provides additional details about the ADCP array setup.

Table 3.1: ADCP setup.

ADCP	Mode	Depth (m)	Pitch (deg)	Roll (deg)	Orientation* (deg)
12N	12	13.2	$-1.4°$	$-3.1°$	$-1.2°$
12S	12	11.7	$-3.6°$	$-2.0°$	$3.9°$
20W	1	21.5	$0.8°$	$-0.6°$	$19.4°$

*Orientation of the y (3–4 beam) axis relative to the principal axis of the depth-averaged flow (positive counterclockwise).

Three 6 MHz Nortek Vector acoustic Doppler velocimeters (ADVs) were deployed on a 3 m vertical spar located 70 m south of ADCP 12N (Figure 3.1). The ADVs were configured to sample at 16 Hz in 16 min bursts every hour. The upper-most probe was oriented upward with a sampling volume located 3 meters above the bed (m.a.b); two downward-looking probes sampled water velocities 1.5 m.a.b with a horizontal separation distance of 1 m. An additional upward-looking 6 MHz Nortek Vector ADV was mounted on a vertical bar collocated with ADCP 12S (Figure 3.1). The latter was configured to sample approximately 1.4 m above the bed at 16

Hz in hourly bursts of 12 min.

The observational period featured weak swell conditions (Figure 3.2a) with minimal short-period wave energy (Figure 3.2b), and generally light winds (not shown). Significant wave heights (H_{sig}) and peak periods (T_{p}) were calculated from ADCP pressure data using spectral analysis and linear wave theory. Tidal variations from pressure measurements at the 12N, 12S and 20W ADCPs (Figure 3.2c) show a dominant semidiurnal tidal signal, and a discernible spring-neap tidal cycle. Conditions were marked by strong semidiurnal alongshore velocities (Figure 3.2d) with significantly weaker cross-shore currents (Figure 3.2e). Salinity contributions to density were negligible over the observational period (Arzeno et al., 2018). Arzeno et al. (2018) estimated gradient Richardson numbers (Ri) at the 12N T-chain (not shown), and determined that conditions were unstratified (Ri < 0.25) 99% of the time. Timeseries data of wind and water temperature difference are shown in Figure 3 in Arzeno et al. (2018).

3.2.2 Stress estimates from ADCP measurements

The variance method

The variance method (Lohrmann et al., 1990; Stacey et al., 1999a; Lu and Lueck, 1999) provides direct estimates of the turbulent Reynolds stresses from the ADCP along-beam velocities. Following Stacey et al. (1999a), the along-beam (radial) velocity equations of a vertically aligned (i.e., zero tilt), upward-looking, four-beam Janus ADCP are given by

$$\begin{aligned} b_1 &= u_1 \sin\theta + w_1 \cos\theta \\ b_2 &= -u_2 \sin\theta + w_2 \cos\theta \\ b_3 &= v_3 \sin\theta + w_3 \cos\theta \\ b_4 &= -v_4 \sin\theta + w_4 \cos\theta\,, \end{aligned} \tag{3.1}$$

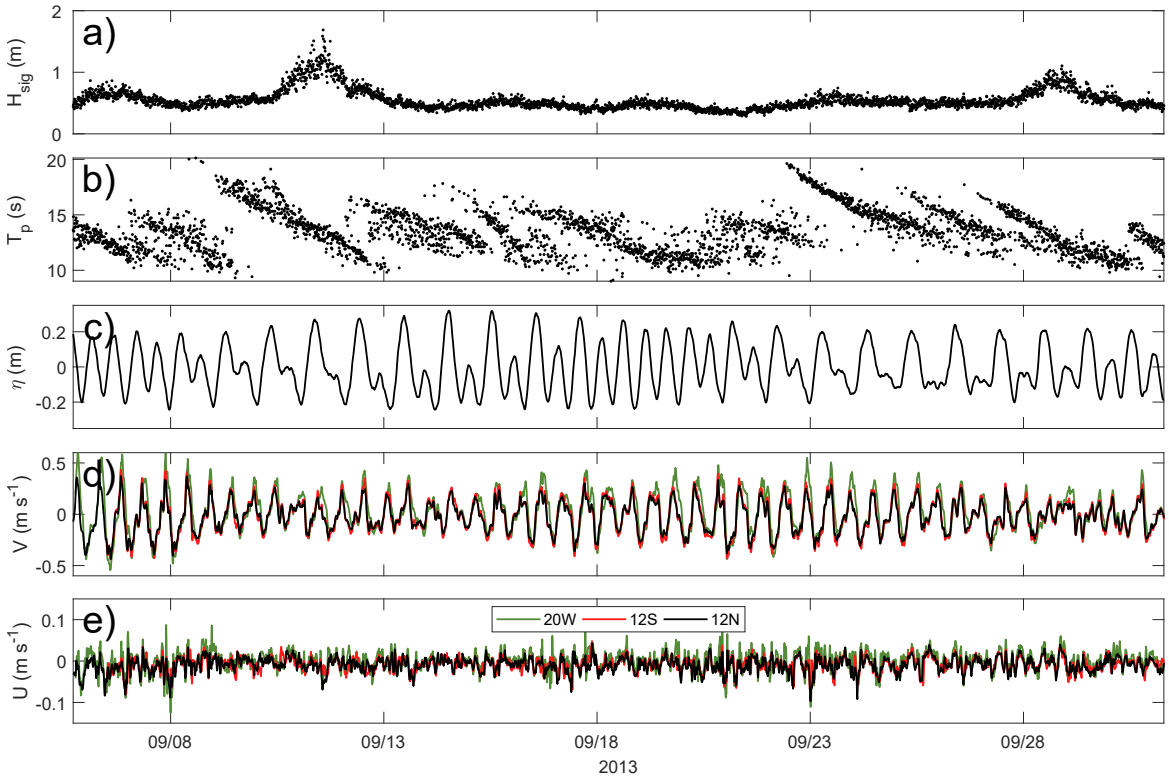

Figure 3.2: Wave, sea surface height, and current conditions at the Makua fore reef based on 20 min averages with 50% overlap. The figure includes time series of (a) significant wave height, (b) peak wave period, (c) sea surface displacement (d) depth-averaged along and (e) cross-shore velocity at 12N, 12S, and 20W. Adapted from Arzeno et al. (2018).

where the radial beam velocities b_i ($i = 1,2,3,4$) are positive towards the ADCP head; u, v, and w are the x, y, and z velocities in a right-handed coordinate system aligned with the ADCP reference frame; and $\theta = 20^\circ$ is the angle of the beams away from vertical. To calculate the Reynolds stresses, the along-beam velocities are decomposed into a time-averaged mean ($\overline{b_i}$) and fluctuating (b_i') part (e.g., $b_i = \overline{b_i} + b_i'$). The vertical components of the Reynolds stress (vertical flux of horizontal momentum) are obtained by differencing the along-beam velocity variances from opposing beam pairs

$$\frac{\tau_{xz}}{\rho} = -\overline{u'w'} = \frac{\overline{b_2'^2} - \overline{b_1'^2}}{4\sin\theta\cos\theta}, \tag{3.2}$$

$$\frac{\tau_{yz}}{\rho} = -\overline{v'w'} = \frac{\overline{b_4'^2} - \overline{b_3'^2}}{4\sin\theta\cos\theta}, \tag{3.3}$$

where ρ is density, and τ_{xz} and τ_{yz} are the vertical turbulent stress components. Similarly, we can extract estimates of the lateral Reynolds stress (horizontal flux of horizontal momentum) from a four-beam Janus ADCP by combining the along-beam velocity covariances of adjacent beam pairs

$$\frac{\tau_{xy}}{\rho} = -\overline{u'v'} = \frac{\overline{b_1'b_3'} - \overline{b_1'b_4'} - \overline{b_2'b_3'} + \overline{b_2'b_4'}}{4\sin^2\theta}. \tag{3.4}$$

The estimation of the lateral stress component ($\overline{u'v'}$) from (3.4) requires that turbulent motions maintain a level of spatial coherence across the adjacent beam pairs. In other words, the lateral turbulence must have length scales, λ_t, comparable to or greater than the separation length scale of the adjacent beam pairs ($\lambda_t > \sqrt{2}R\tan\theta$, where R is the vertical distance from the transducer head to the ADCP range cell) in order to be detectable by the adjacent beam covariances ($\overline{b_i'b_j'}$) (Dewey and Stringer, 2015). This is in contrast to the vertical stress ($\overline{u'w'}$, $\overline{v'w'}$) calculations, for which the instantaneous velocity fluctuations need not be coherent at opposing beam locations (Stacey et al., 1999a). The variance technique for the vertical stresses in (3.2) and (3.3) only requires that turbulence characteristics be stationary over the averaging interval and

statistically homogeneous to second order (i.e., $\overline{u_1'^2} = \overline{u_2'^2} = \overline{u'^2}$) at the scale of the ADCP beam spread (Lu and Lueck, 1999).

The applicability of the variance technique is limited by various sources of error, including measurement uncertainties, misalignment errors, and wave-induced biases. Moreover, turbulent motions with less than twice the vertical bin size are not detectable by the variance method (Stacey et al., 1999b). This may lead to the underestimation of turbulent stresses, especially under strongly stratified conditions (Kirincich et al., 2010). Observations by Arzeno et al. (2018) indicate vertically well mixed conditions at the Makua study site during the observational period; thus, we expect the effects of stratification to be negligible (see section 3.2.1). In section 3.2.2 we discuss methods to isolate the turbulence spectrum and remove wave-induced errors from ADCP-based Reynolds stress estimates. We also examine the effects of misalignment errors and measurement uncertainties in section 3.2.2.

Wave-turbulence decomposition

To compute ADCP-derived Reynolds stress estimates, raw along-beam velocities were segmented into 20 min windows with a 50% (10 min) overlap. Measurements from the top 11% of the water column were excluded to prevent acoustic sidelobe contamination. Along-beam velocities smaller than the ADCP error velocities were rejected and replaced with interpolated values. Data records (20 min intervals) in which the fraction of interpolated pings exceeded 15% of the total number of data points were excluded from the analysis.

Following the work of Kirincich et al. (2010), we rewrite the variance method in equations

(3.2)–(3.4) in spectral form as

$$Co_{u'w'}(f) = \frac{S_{b_1b_1}(f) - S_{b_2b_2}(f)}{4\sin\theta\cos\theta}, \tag{3.5}$$

$$Co_{v'w'}(f) = \frac{S_{b_3b_3}(f) - S_{b_4b_4}(f)}{4\sin\theta\cos\theta}, \tag{3.6}$$

$$Co_{u'v'}(f) = \frac{S_{b_1b_4}(f) - S_{b_1b_3}(f) - S_{b_2b_4}(f) + S_{b_2b_3}(f)}{4\sin^2\theta}, \tag{3.7}$$

where $S_{b_ib_i}(f)$ and $S_{b_ib_j}(f)$ represent along beam velocity spectra and adjacent beam cospectra, respectively. For each 20 min burst we compute the spectral quantities [$S_{b_ib_i}(f)$ and $S_{b_ib_j}(f)$] in (3.5)–(3.7) from quality-controlled, de-meaned along-beam velocities (e.g., $b_i' = b_i - \overline{b_i}$) using a single Hanning-tapered window, and derive estimates of the horizontal wave velocities (σ_w) and vertical wave velocity pseudo-spectra ($\hat{S}_{ww}$) from ADCP pressure data via linear wave theory.

We focus below on an example drawn from a 20 min burst at a single depth cell located 3.8 m above the bed to illustrate the wave-turbulence decomposition technique for the lateral stress cospectra (Figure 3.3). To isolate the low frequency (below the wave band) turbulent fluctuations from the surface gravity wave-induced motions, we apply a waveband cutoff frequency, f_{wc} (see vertical dot-dash line Figure 3.3). The waveband cutoff is defined by the frequency at which the pressure-based vertical velocity pseudo-spectrum, $\hat{S}_{ww}$ (Figure 3.3a), exceeds the mean along-beam velocity spectrum ($\overline{S_{b_ib_i}}$) (Kirincich et al., 2010; Gerbi et al., 2008). Below this cutoff ($f < f_{wc}$), the velocity cospectra (Figure 3.3b) are assumed to be dominated by turbulent motions. Below-wave band Reynolds stress estimates are thus obtained by integrating (3.5)–(3.7) at frequencies below the waveband [$\overline{u_i'u_j'}_{\mathrm{LF}} = \int_0^{f_{wc}} Co_{u_i'u_j'}\,\mathrm{d}f$] (Figure 3.3c). It is worth noting that the full spectrum integrals (i.e., the total covariance) of (3.5)–(3.7) yield equivalent values to those computed in (3.2)–(3.4) via the variance method.

If applied correctly, the spectral wave-turbulence decomposition technique described above should not suffer from the wave biases that affect the variance method because it relies only on the low-frequency (below the wave band) portion of turbulence cospectrum to estimate

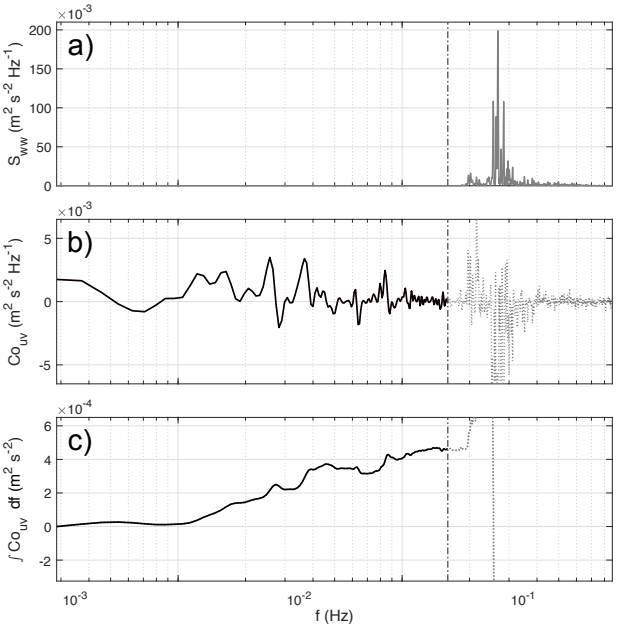

Figure 3.3: Wave-turbulence decomposition technique applied to a 20 min sample burst, 3.8 m above the seabed at ADCP 12N: (a) vertical velocity spectra pseudo-spectra ($\hat{S}_{ww}$) derived from pressure spectra, (b) lateral turbulent stress cospectra derived from (3.7), and (c) integrated turbulent stress cospectra (ogive curves). Vertical dot-dash lines indicate the wave cutoff frequency f_{wc}.

the turbulent stresses. However, the proposed technique avoids these wave biases at the expense of neglecting the turbulent stresses that reside within the wave band. Therefore, screening criteria were applied to ensure that most of the turbulent stress is contained below the wave cutoff frequency (f_{wc}) and to limit the kinematic effects of wave induced advection on the observed cospectra. These quality controlled, below-wave band covariances should be nearly the same as the actual Reynolds stresses, but slightly smaller. Screening procedures are described in section 3.3.2.

Alignment errors

In practice, the ADCP reference frame is often slightly misaligned from the "true" (x, y, z) coordinate system. Here, the true coordinate system refers to a reference frame that is vertically aligned with gravity and parallel to the principal axes of the flow. Instrument tilt angles or an

imperfect alignment with the principal axis of the flow can introduce biases in the estimation of variance method stresses, even in the absence of waves.

Assuming small angle rotations ($\sin\psi \sim \psi$, $\cos\psi \sim 1$) and retaining only the first order terms ($\psi^2 \ll 1$), we can derive an expression for the instrument velocities (u_I, v_I, w_I) in terms of the true velocities (u, v, w) (Rosman et al., 2008)

$$\begin{bmatrix} u_I \\ v_I \\ w_I \end{bmatrix} = \begin{bmatrix} 1 & \psi_H & -\psi_R \\ -\psi_H & 1 & \psi_P \\ \psi_R & -\psi_P & 1 \end{bmatrix} \begin{bmatrix} u \\ v \\ w \end{bmatrix}, \tag{3.8}$$

where ψ_P, ψ_R, and ψ_H are the instrument pitch, roll, and heading angles (in radians), respectively, and represent rotations about the "true" x, y, and z axes (positive counterclockwise). With this, the variance method equations (3.2)–(3.4) become

$$\frac{\overline{b_2'^2} - \overline{b_1'^2}}{4\sin\theta\cos\theta} = -\overline{u'w'} + \psi_R(\overline{w'^2} - \overline{u'^2}) + \psi_P\overline{u'v'} - \psi_H\overline{v'w'}, \tag{3.9}$$

$$\frac{\overline{b_4'^2} - \overline{b_3'^2}}{4\sin\theta\cos\theta} = -\overline{v'w'} + \psi_P(\overline{v'^2} - \overline{w'^2}) + \psi_H\overline{u'w'} - \psi_R\overline{u'v'}, \tag{3.10}$$

$$\frac{\overline{b_1'b_3'} - \overline{b_1'b_4'} - \overline{b_2'b_3'} + \overline{b_2'b_4'}}{4\sin^2\theta} = -\overline{u'v'} + \psi_H(\overline{u'^2} - \overline{v'^2}) + \psi_R\overline{v'w'} - \psi_P\overline{u'w'}. \tag{3.11}$$

For unstratified open-channel flows with smooth beds and high Reynolds numbers, Nezu and Nakagawa (1993) (see also Stacey et al., 1999a) give $\overline{v'^2} \approx 5.29u_*^2$, $\overline{u'^2} \approx 2.66u_*^2$, and $\overline{w'^2} \approx 1.61u_*^2$, where u_* is the friction velocity. If we further assume that $\overline{u'w'} \ll \overline{v'w'} \sim \overline{u'v'} \sim u_*^2$ and that turbulent intensities ($\overline{v'^2}$, $\overline{u'^2}$, $\overline{w'^2}$) and Reynolds stresses are in phase throughout the tidal cycle, then the alignment error for the vertical and lateral stress components reduces to $\varepsilon_{vw} \sim (3.7\psi_P \pm \psi_R)\overline{v'w'}$ and $\varepsilon_{uv} \sim (2.6\psi_H \pm \psi_R)\overline{u'v'}$ for the smooth wall case. Given our pitch, roll, and heading values, at worst this can result in biases (ε_{vw}) as high as 14% and 26% of the total $\overline{v'w'}$ stress for the 12N and 12S ADCPs, respectively (see Table 3.1 for rotation angles).

For the lateral stress, the estimated alignment biases (ε_{uv}) can be up to 11% and 21% of the total $\overline{u'v'}$ stress at the 12N and 12S ADCPs, respectively. For rough beds such as coral reefs, however, we anticipate a reduction in the level of anisotropy relative to the smooth wall case (Smalley et al., 2002; Nezu and Nakagawa, 1993). This is because bottom roughness tends to redistribute turbulent energy towards isotropy, thus reducing the difference between velocity variances ($\overline{u_i'^2} - \overline{u_j'^2} \to 0$). Alignment biases should therefore decrease for both the vertical and horizontal stresses as anisotropy decreases and turbulent intensities become more comparable.

Uncertainty in stress measurements

The uncertainty error in the stress measurements via (3.3) and (3.4) is defined by the variance of these equations (Stacey et al., 1999a). A number of techniques have been developed to quantify uncertainty in ADCP-derived Reynolds stress estimates. Here, we compute uncertainty estimates for both vertical and lateral below-wave band Reynolds stresses by adapting two different approaches developed by Williams and Simpson (2004) and Lu and Lueck (1999).

Following Williams and Simpson (2004), the variance of (3.3) and (3.4) is given by

$$\mathrm{var}(-\widehat{v'w'}) = \sigma_{vw}^2 = \frac{\mathrm{var}(\widehat{b_3'^2} - \widehat{b_4'^2})}{16\sin^2\theta\cos^2\theta}, \tag{3.12}$$

$$\mathrm{var}(-\widehat{u'v'}) = \sigma_{uv}^2 = \frac{\mathrm{var}(\widehat{b_1'b_3'} - \widehat{b_1'b_4'} - \widehat{b_2'b_3'} + \widehat{b_2'b_4'})}{16\sin^4\theta}, \tag{3.13}$$

where the hat operator represents an estimator of the expected value. These expressions can be expanded using the additive rule for covariances and the central limit theorem (e.g., $\mathrm{var}(\widehat{b_i'^2}) =$

$(1/N)\sum_{n=1}^{N} b_i'^2(n) = \mathrm{var}(b_i'^2)/N)$ to give

$$\sigma_{vw}^2 = \frac{\gamma_{vw}}{16N\sin^2\theta\cos^2\theta}\left[\mathrm{var}(b_3'^2) + \mathrm{var}(b_4'^2) - 2\mathrm{cov}(b_3'^2, b_4'^2)\right], \tag{3.14}$$

$$\begin{aligned}\sigma_{uv}^2 = \frac{\gamma_{uv}}{16N\sin^4\theta}\Big[&\mathrm{var}(b_1'b_3') + \mathrm{var}(b_1'b_4') + \mathrm{var}(b_2'b_3') + \mathrm{var}(b_2'b_4') \\ &- 2\mathrm{cov}(b_1'b_3', b_1'b_4') - 2\mathrm{cov}(b_1'b_3', b_2'b_3') + 2\mathrm{cov}(b_1'b_3', b_2'b_4') \\ &+ 2\mathrm{cov}(b_1'b_4', b_2'b_3') - 2\mathrm{cov}(b_1'b_4', b_2'b_4') - 2\mathrm{cov}(b_2'b_3', b_2'b_4')\Big],\end{aligned} \tag{3.15}$$

where $N = 600$ is the number of measurements in each burst, $\gamma_{u_iu_j}$ is a correction factor

$$\gamma_{u_iu_j} = 1 + 2\sum_{n=2}^{K} C_{bb}(1,n), \tag{3.16}$$

that accounts for the correlation of consecutive non-independent samples (Williams and Simpson, 2004), C_{bb} is a normalized autocovariance function for the square of the along-beam velocity fluctuations

$$C_{bb}(1,m) = \frac{\sum_{n=1}^{N-1}\sum_{m=n+1}^{N} b_i'^2(n), b_i'^2(m)}{\sum_{n=1}^{N}\mathrm{var}[b_i'^2(n)]}. \tag{3.17}$$

The upper limit $m = K \ll N$ in (3.16) is defined as the lag at which C_{bb} crosses the upper bound of its uncertainty level. For sufficiently large K values (typically > 30 s), the along-beam velocity fluctuations become uncorrelated and $C_{bb} \to 0$. To compute C_{bb}, we low-pass filter the along-beam fluctuations using the wave cutoff frequency (f_{wc}) to attenuate wave-induced velocities. The factor $\gamma_{u_iu_j}$ was similar for both vertical and lateral stresses, and varied between 14 and 10 for peak and slack velocities, respectively.

Reynolds stress uncertainty estimates were also computed directly from the data using a Monte Carlo type approach following Lu and Lueck (1999) (see also, Kirincich et al., 2010). In

this case, we rearrange (3.3) and (3.4) into an equivalent covariance form

$$\frac{\overline{b_4'^2} - \overline{b_3'^2}}{4\sin\theta\cos\theta} = \frac{\overline{(b_4' + b_3')(b_4' - b_3')}}{4\sin\theta\cos\theta}, \tag{3.18}$$

$$\frac{\overline{b_1'b_3'} - \overline{b_1'b_4'} - \overline{b_2'b_3'} + \overline{b_2'b_4'}}{4\sin^2\theta} = \frac{\overline{(b_1' - b_2')(b_3' - b_4')}}{4\sin^2\theta}, \tag{3.19}$$

and randomly shift the sum (or difference) velocity time series by a lag (or lead) greater than the along-beam velocity decorrelation timescale. Similar to (3.17), we compute the along-beam velocity decorrelation timescale estimates using along-beam low-pass filtered velocity fluctuations (below the wave band). Decorrelation timescales ranged between 15–80 s for slack and peak velocities, respectively. Histograms of lagged covariance estimates are constructed for each 20-min burst by computing the below-waveband covariances for 1000 random lags. Stress uncertainties are then calculated as the 2σ significance levels of these lagged, below-wave band covariance histograms.

Figure 3.4 shows quality controlled (see section 3.3.2) uncertainty estimates for variance method stresses, defined here as two standard deviations (2σ), as a function of the below-wave band Reynolds stress estimates ($\overline{u_i'u_j'}_{\mathrm{LF}}$). Binned average uncertainties obtained via methods outlined by Lu and Lueck (1999) (black circles) and Williams and Simpson (2004) (white squares) were in close agreement for all datasets. Consistent with previous observations (e.g., Williams and Simpson, 2004; Rosman et al., 2008; Kirincich et al., 2010), mean uncertainties increase with the magnitude of the stress. Using a least squares fit, the minimum uncertainty levels for vertical and lateral stresses were estimated as 2.1×10^{-5} m^2 s^{-2} and 5.5×10^{-5} m^2 s^{-2}, respectively. The lateral stress uncertainties (Figure 3.4c,d) were, on average, ~ 2.8 times larger than their vertical counterparts (Figure 3.4a,b). This factor is likely due to the ADCP beam geometry, as the ratio of the values in the denominator of (3.3)–(3.4) yields $(\sin\theta\cos\theta)/(\sin^2\theta) \approx 2.75$ for $\theta = 20^\circ$.

As noted by Nidzieko et al. (2006), accurate ADCP estimates of Reynolds stress are possi-

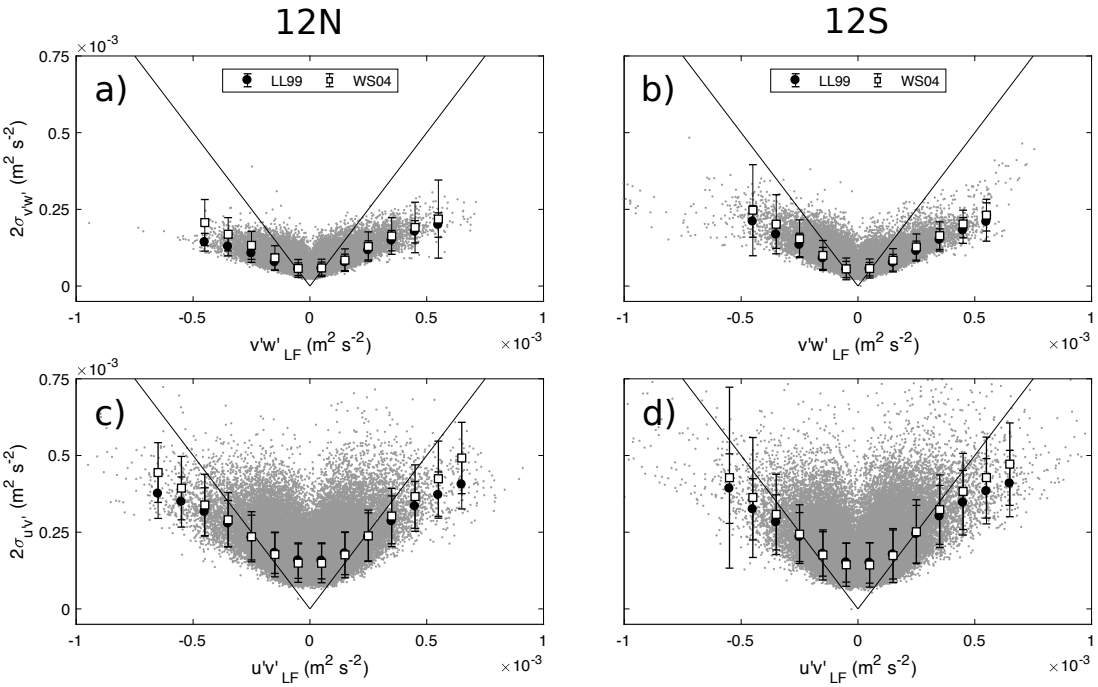

Figure 3.4: Raw (gray dots) and binned-averaged cospectra uncertainty estimates ($2\sigma_{u_i'u_j'}$) via methods proposed by Lu and Lueck (1999) (black circles) and Williams and Simpson (2004) (white squares), plotted against the zero-lag, below-wave band covariance ($\overline{u_i'u_{jLF}'}$) for (a),(c) 12N and (b),(d) 12S ADCPs. Uncertainty estimates are defined as two standard deviations (2σ). Error bars indicate the standard deviation for each bin average. Stress levels become larger than the uncertainty estimates below the solid lines.

ble when the stress estimates are discernible from the background noise. Results in Figure 3.4c,d show that, for most bursts, individual lateral stress estimates are highly uncertain. This in contrast to the vertical stress measurements, which clearly have a lower noise floor and exhibit lower uncertainties overall (Figure 3.4a,b). In section 3.3, we use phase ensemble averaging to increase the signal-to-noise ratio of our lateral stress estimates.

3.2.3 Stress estimates from ADV measurements

ADV-derived Reynolds stress estimates were computed directly from velocity cospectra below the wave band, following the wave-turbulence separation method outlined in section 3.2.2, to enable comparisons with ADCP values. ADV velocities were rotated into the right handed (x, y, z) coordinate system shown in Figure 3.1, so that u and v velocities were aligned with the depth-averaged cross- and alongshore flow, respectively (w was upward positive). Velocity data was de-spiked and poor data quality points with correlations < 0.7 were rejected (Feddersen and Williams, 2007). Data gaps with less than 8 consecutive invalid data points (0.5 s) were linearly interpolated. Reynolds stress estimates were computed hourly using an averaging interval equivalent to the ADV sampling window (16 min and 12 min for 12N and 12S ADVs, respectively).

3.2.4 Phase ensemble averaging

Given the regularly periodic alongshore velocities resulting from the dominant semidiurnal tidal pattern observed at Makua (see Figure 3.2), it is convenient to examine the turbulent properties of the flow as a function of tidal phase. We therefore employ an ensemble averaging approach to increase the reliability of ADCP-derived turbulent quantities and provide a more representative measure of the vertical structure and temporal evolution of the turbulent stress estimates. The phase ensemble averaging procedure is similar to the one described by Arzeno

et al. (2018), with some minor modifications. In this case, we extract the tidal phase (ϕ) for each site (12N, 12S) from depth-averaged alongshore velocity signal via complex demodulation (Thomson and Emery, 2014) using a filter centered on the M_2 tidal frequency band (12.42 h). The tidal phase (ϕ) is defined so that the interval between maximum depth-averaged northward currents follows linearly from 0° to 360° in 5 degree increments for each tidal cycle. Cross- and alongshore velocity measurements, vertical shear, sea surface height, turbulence cospectra, and Reynolds stress estimates are then phase-averaged over 50 tidal cycles using 10 degree phase blocks.

3.3 Results

3.3.1 Turbulence cospectra and roll-off wavenumbers

We can examine the turbulence cospectra to gain some insight into the quality of the Reynolds stress estimates and to calculate the roll-off wavenumber (k_0), which is associated with the horizontal length scale of the dominant stress-carrying eddies ($\lambda_0 = 2\pi/k_0$). Here, we consider ADCP-based variance-preserving cospectra ($kCo_{u_iu_j}$) and ogive curves ($Og_{u_iu_j}$) for both vertical and lateral stress components. The ogive curves represent the cumulative integral of the turbulence cospectra. The location of the roll-off wavenumber (k_0) is represented by the peak in the variance-preserving cospectrum or, equivalently, by the inflection point in the ogive curve.

To estimate k_0, observed frequency cospectra [$Co_{u_iu_j}(f)$] are computed using (3.6)–(3.7) and converted to wavenumber cospectra [$Co_{u_iu_j}(k)$] using a frozen turbulence approximation $2\pi f = k|v_c|$, where v_c represents the local mean horizontal velocity of the flow for each 20 min burst. We omit data within the wave band using the wave-turbulence decomposition technique described in section 3.2.2, and only consider cases when $\sigma_w/|v_c| < 2$. To minimize the effects of noise in individual cospectra, integrated cospetra (ogive curves) are normalized by the below-wave

band covariance

$$Og_{u_iu_j}(k) = \frac{\int^k Co_{u_iu_j}(\hat{k})\,\mathrm{d}\hat{k}}{\overline{u_i'u_j'}_{\mathrm{LF}}},$$

and grouped together by depth cell (z) and tidal phase (ϕ) using 10 degree phase blocks (see section 3.2.4). Phase ensemble averages of multiple $Og_{u_iu_j}(k)$ realizations reduce the effects of spectral noise, and enable smoother cospectral estimates. This allows the estimation of a representative roll-off wavenumber (k_0) as a function of tidal phase (ϕ) and depth (z) without assuming any particular cospectral shape via the inflection point in the ogive ensemble (composed of 20–40 individual realizations). The inflection point is determined from a least squares spline fit to the ogive data. Anomalous ogive curves with a standard deviation exceeding the standard deviation of the ensemble by more than a factor of three are classified as outliers and rejected from the analysis (see section 3.3.2).

Figure 3.5 shows ensemble-averaged estimates of the non-dimensional variance-preserving cospectra (Figure 3.5a,b,c,d) and the associated ogive curves (Figure 3.5e,f,g,h) as a function of nondimensional wavenumber (k/k_0) for the 12N and 12S ADCPs. Prior to averaging, all of the individual ogive curves and variance-preserving cospectra (kCo) are grouped into logarithmically spaced normalized wavenumber (k/k_0) bins. The resulting spectral distributions collapse according to the roll-off wavenumber, a quantity that varies with tidal phase in this case (see Figure 3.7).

The observed cospectral estimates can be compared to more familiar Kaimal et al. (1972) model

$$Co^*_{u_i'u_j'}(k)/\overline{u_i'u_j'} = \left(\frac{7}{3\pi}\sin\frac{3\pi}{7}\right)\frac{1/k_0}{1+(k/k_0)^{7/3}}. \tag{3.20}$$

The Kaimal model is a semi-theoretical prediction of the one-dimensional turbulence cospectra derived from observations of the atmospheric boundary layer. While previous studies have successfully applied the Kaimal model in a variety of oceanographic settings as a tool to filter out wave contributions from vertical turbulent cospectra (e.g., Feddersen and Williams, 2007;

Gerbi et al., 2008; Kirincich et al., 2010), the validity of using (3.20) for characterizing the lateral turbulent cospectra is questionable because its spectral distribution is not known a priori. Hence, the plots in Figure 3.5 show the variance preserving and ogive curves derived from the non-dimensional Kaimal model (gray curves) for reference only.

Normalized variance-preserving plots for both the vertical (Figure 3.5a,b) and lateral (Figure 3.5c,d) stress components show good overall agreement with the Kaimal model at the 12N and 12S sites. In all cases, the observed variance preserving cospectra show slight deviations from the model at low and high wavenumbers, and lower covariance near the peak ($k/k_0 = 1$). These deviations are likely the result of either random inaccuracies in the estimation of k_0 or spectral scatter around k_0, in combination with the effects of spectral noise. Note also the that lateral stress cospectra exhibit higher uncertainties (Figure 3.5c,d) than the vertical stress cospectra (Figure 3.5a,b), consistent with results obtained in section 3.2.2. Further, the nondimensional ogive curves (Figure 3.5e,f,g,h) also fall close to the Kaimal model. Interestingly, the observed ogive curves for the lateral stress cospectra (Figure 3.5g,h) exhibit a somewhat steeper slope around their inflection point ($k/k_0 = 1$) relative to the ogive curves for the vertical stress cospectra (Figure 3.5e,f), which suggests that the lateral stress cospectra may contain more energy at higher frequencies than the vertical stress cospectra.

3.3.2 Screening criteria

Recent results by Rosman and Gerbi (2017) indicate that the observed below-waveband turbulent cospectra remains relatively unaffected by wave orbital motion when rms wave orbital velocities (σ_w) are less than twice the current speed $\sigma_w/|v_c| < 2$, and when the wave orbital excursion is smaller than the length scale of the stress-carrying eddies $\sigma_w k_0/\omega_w < 0.5$, where ω_w represents the wave radian frequency. Under such conditions, over 80% of the turbulence covariance is expected to reside in frequencies below the wave peak, and about 60% of the total stress covariance should be contained at frequencies below the turbulence roll-off frequency

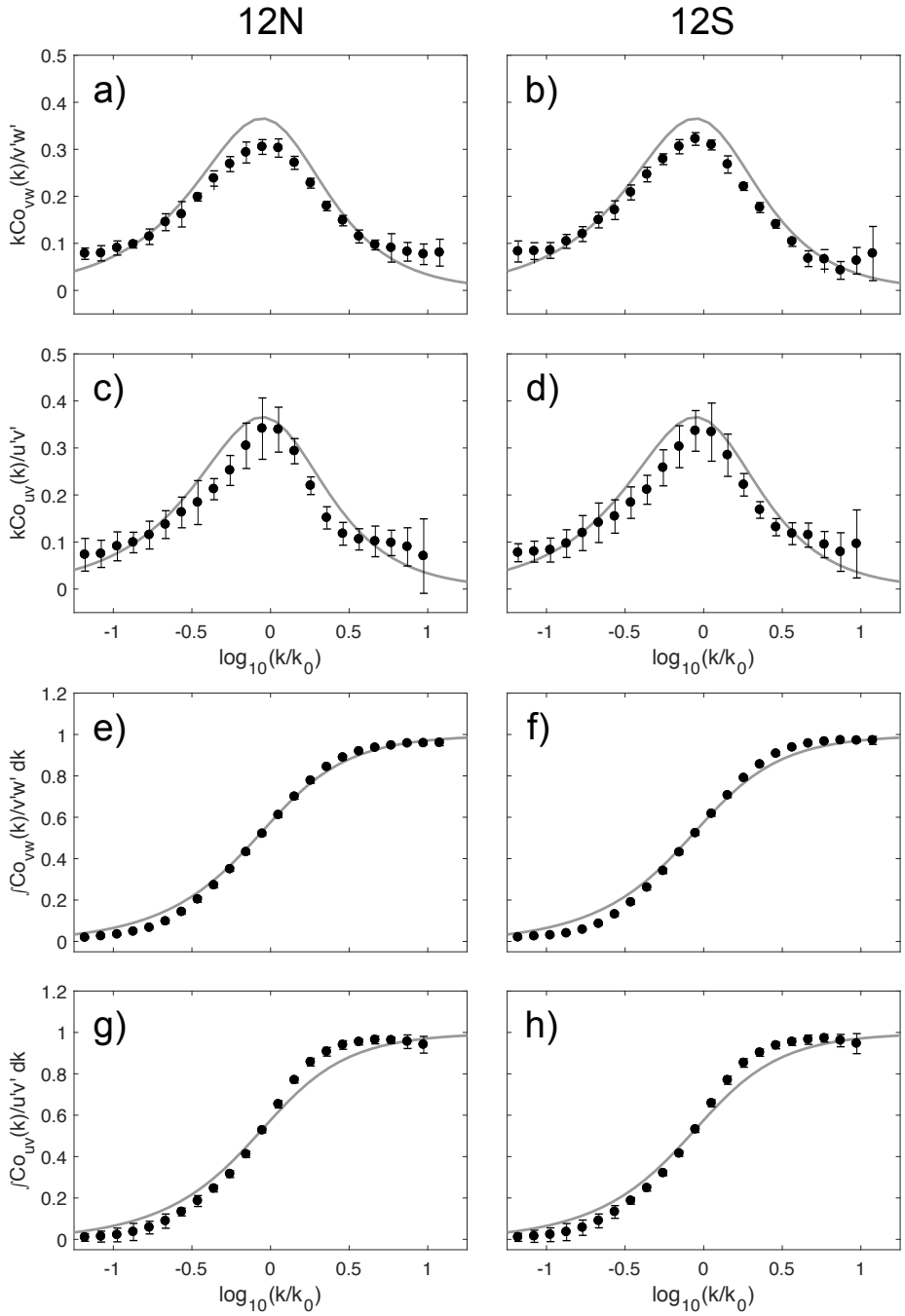

Figure 3.5: Normalized variance-preserving cospectra (a,b,c,d) and ogive curves (e,f,g,h) as a function of normalized wavenumber (k/k_0) for the 12N (left panels) and 12S (right panels) ADCPs. Panels (a,b,e,f) and (c,d,g,h) show results for vertical and lateral stress cospectra, respectively. Black dots represent bin averages of all the observations. Vertical error bars show the 95% confidence intervals estimated using a bootstrapped method. The solid gray curves show the Kaimal model (3.20) for reference.

($f_0 = k_0|v_c|/2\pi$), assuming a Kaimal spectrum (3.20) (Rosman and Gerbi, 2017). To ensure that most of the turbulence covariance is contained below the wave cutoff frequency (f_{wc}), we therefore restrict our observations to instances when $\sigma_w/|v_c| < 2$ and $\sigma_w k_0/\omega_w < 0.5$. In addition, as noted in section 3.3.1, we reject bursts if the normalized ogive curve standard deviation is three times greater than that of the phase ensemble.

Histograms in Figure 3.6a,c show that most of the bursts (73% and 77% for 12N and 12S, respectively) lie below the $\sigma_w/|v_c| < 2$ threshold. Histograms in Figure 3.6b,d show the distribution of quality controlled data ($\sigma_w/|v_c| < 2$ and $\sigma_w k_0/\omega_w < 0.5$) as a function of $\sigma_w k_0/\omega_w$ for the vertical ($\overline{v'w'}$) and lateral ($\overline{u'v'}$) stress components. It should be noted that applying the $\sigma_w k_0/\omega_w < 0.5$ criteria a posteriori does not increase the amount of rejections by more than 2% for either stress component. On the other hand, the ogive standard deviation criteria (described above in section 3.3.1) further limits the amount of valid vertical and lateral stress measurements, respectively, to 62% and 54% of the total bursts at 12N, and to 66% and 58% of the total bursts at 12S.

3.3.3 Turbulence length scales

As described in section 3.3.1, the roll-off length scales (λ_0) are estimated empirically from phase-averaged ogive curves (below the waveband) using the frozen turbulence hypothesis, and represent the horizontal (in the direction of the mean current) length scale of the dominant stress-carrying eddies.

Figure 3.7 shows the depth-averaged roll-off lengthscales ($\lambda_0 = 2\pi/k_0$) derived from vertical (Figure 3.7a) and lateral (Figure 3.7b) turbulent cospectra as a function of tidal phase (ϕ) for both 12N (black) and 12S (red) ADCPs. Several features are evident from our depth- and tidally-averaged estimates of $\lambda_0 vw$ and $\lambda_0 uv$. In all cases, the roll-off lengthscales show a similar behavior with tidal phase, varying approximately in phase with the mean alongshore flow (see Figure 3.9e,f). For both sites, the depth-averaged roll-off wavelengths were roughly two to three

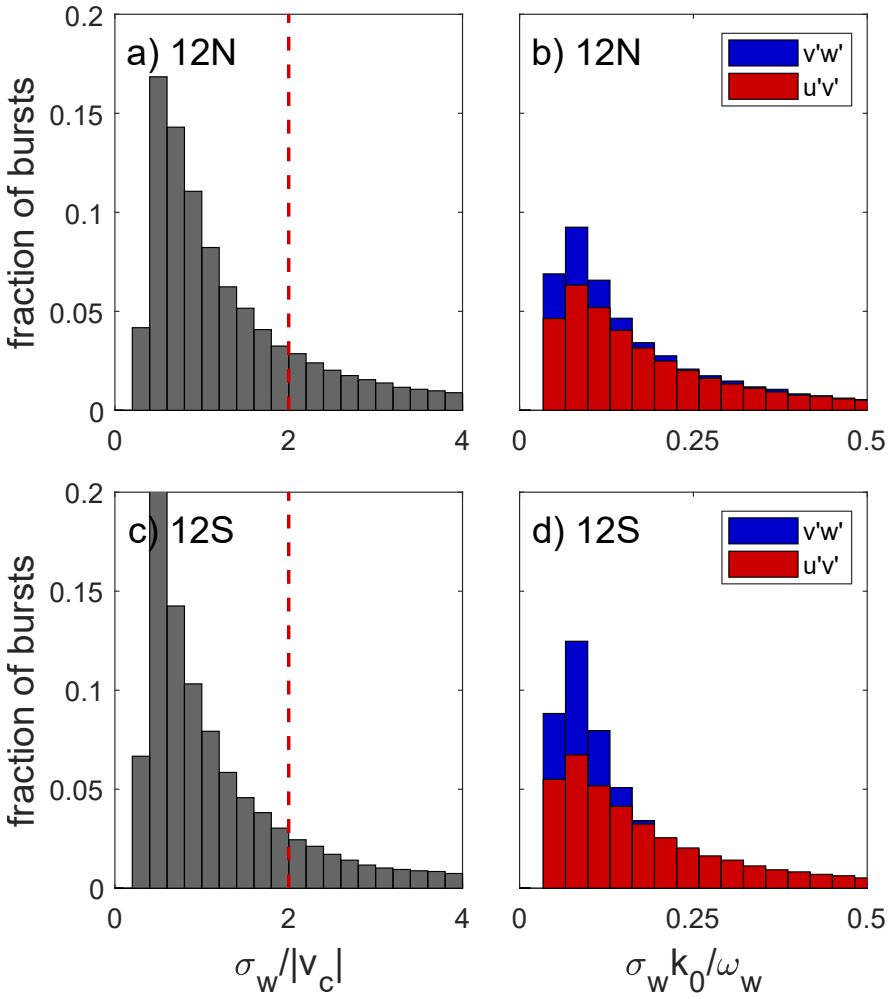

Figure 3.6: Screening criteria for the spectral wave-turbulence decomposition method for (a)–(b) 12N and (c)–(d) 12S ADCPs. Panels (a) and (c) show histograms of the wave advection to current speed ratio ($\sigma_w/|v_c|$) for the observational period. Panels (b) and (d) show histograms of the ratio of wave orbital excursion to estimated turbulence length scale ($\sigma_w k_0/\omega_w$) for quality controlled bursts with $\sigma_w/|v_c| < 2$ and $\sigma_w k_0/\omega_w < 0.5$ for the vertical (blue) and lateral (red) stress components.

times larger than the depth of the water column, with timescales of around 2–3 min. Comparisons between $\lambda_0 vw$ and $\lambda_0 uv$ indicate that the turbulent eddies associated with the vertical stress cospectra (Figure 3.7a) were coherent over longer lengthscales (between $20\% - 50\%$ longer) than those associated with the lateral stress cospectra (Figure 3.7b) at max currents ($\phi \approx 0^\circ$, $\phi \approx 180^\circ$). For slack water ($\phi \approx 90^\circ$, $\phi \approx 270^\circ$), the turbulent lengthscales were found to be comparable.

Throughout the tidal cycle, a similar behavior is observed for both $\lambda_0 vw$ and $\lambda_0 uv$, suggesting a correspondence between the vertical ($\lambda_0 vw$) and lateral ($\lambda_0 uv$) turbulent lengthscales. Furthermore, our findings suggest that $\lambda_0 uv \sim \lambda_0 vw \sim h$, where h is the local water depth. Alternatively, these large-scale turbulent motions might be related to the dominant roughness features [e.g., spur and groove formations (see Chapter 4)]. It might be anticipated that $\lambda_0 uv$ should scale with the length scale for lateral changes in velocity. Spatial velocity measurements at Makua (Chapter 4), however, reveal that the alongshore flow changes over lateral scales L_x that are much greater than the observed turbulence length scales. This implies that the turbulent motions associated with bottom-driven turbulence likely dominate the transport of vertical and lateral turbulent fluxes.

3.3.4 Reynolds stress estimates

To assess the performance of ADCP-based Reynolds stress estimates, a comparison with independent, collocated ADV measurements was carried out at 12N and 12S using phase-averaged data (see section 3.2.4). In Figure 3.8, we show the observed below-wave band stress estimates (LF) and cospectra-fit method (Gerbi et al., 2008; Kirincich et al., 2010) estimates (CF) for the vertical (Figure 3.8a,b,e,f) and horizontal (Figure 3.8c,d,g,h) stress components. Note that we cannot assume that the cospectral shape given by (3.20), typically applied for vertical stresses, should apply to lateral stress. While results in Figure 3.5c,d,g,h suggest that the Kaimal model adequately describes the low-wavenumber cospectra resulting from the lateral turbulent fluctuations, CF results for $\overline{u'v'}$ cospectra should be interpreted with caution. Comparisons were

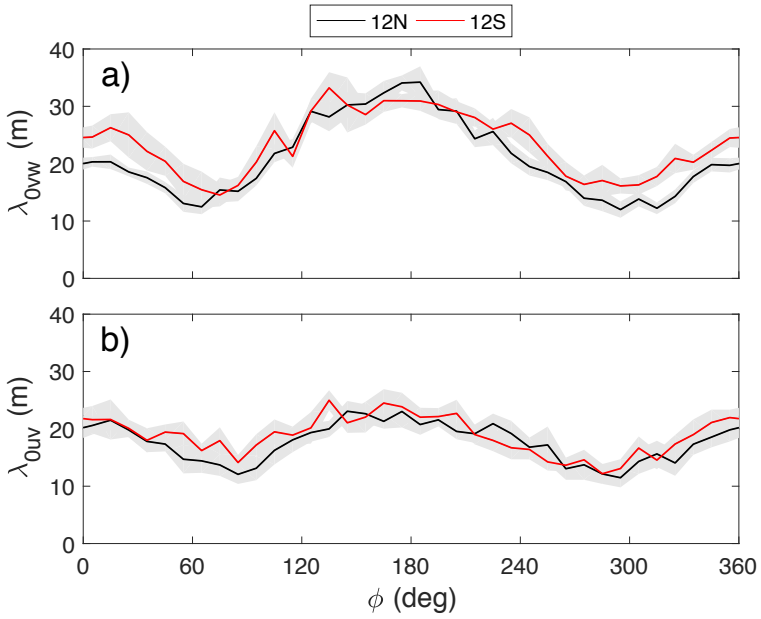

Figure 3.7: Depth- and tidally-averaged roll-off lengthscales ($\lambda_0 = 2\pi/k_0$) derived from the (a) vertical and (b) lateral stress cospectra at the 12N (black) and 12S (red) ADCPs. Shaded regions illustrate the 95% bootstrapped confidence intervals.

carried out using vertically-averaged ADCP data from four depth bins centered around the ADV sampling volume.

As shown in Figure 3.8, ADCP-based vertical and lateral stress estimates compare favorably with ADV estimates at both sites. Below wave-band (LF) and model-derived (CF) stress estimates yield comparable results, providing additional support to the assertion that most of the turbulent covariance is contained below the wave band. In general, the vertical stress comparisons (Figure 3.8b,f) exhibit higher correlations than the lateral stress comparisons (Figure 3.8d,h). This is consistent with results obtained in section 3.2.2, which show that lateral stress calculations are prone to higher uncertainty levels than the vertical stresses. Also, more scatter is observed for both the vertical and lateral stress comparisons at 12N (Figure 3.8b,d) relative to 12S (Figure 3.8f,h). The higher scatter observed at 12N can be attributed to the separation distance between the ADCP and the ADV sensors. For 12N this separation distance was approximately 70 m, whereas for 12S the instruments were virtually collocated (see Figure 3.1).

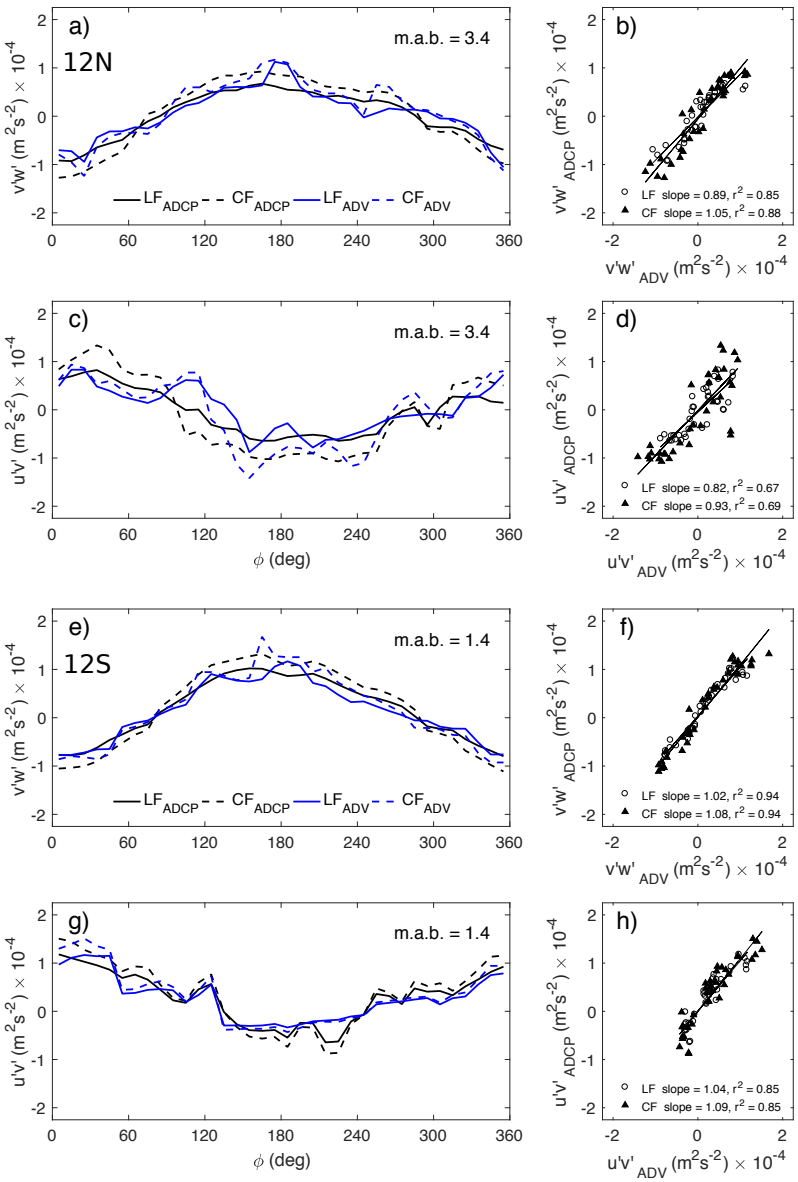

Figure 3.8: Ensemble phase-average comparisons of ADV (blue lines) and ADCP (black lines) based LF (solid lines) and CF (dashed lines) methods for (a,e) vertical ($\overline{v'w'}$) and (c,g) lateral ($\overline{u'v'}$) turbulent stress estimates 3.4 and 1.4 meters above the bed (m.a.b.) at 12N (a,c) and 12S (e,g), respectively. Right panels (b,d,f,g) show the corresponding linear regressions, slopes, and correlation coefficients (r^2) between the ADCP and ADV for ensemble phase-averaged LF and CF stress estimates.

Figure 3.9 shows phase-averaged results for the sea surface height (η), and the vertical structure of the flow and of the below-wave band Reynolds stress estimates as a function of ADCP range cell for the 12N (Figure 3.9a,c,e,g,i,k) and 12S (Figure 3.9b,d,f,h,j,l) moorings. As described in section 3.2.4, the tidal phase is defined so that the depth averaged alongshore flow adheres to the shape of a cosine function ($\cos\phi$), with maximum northward and southward currents occurring around $\phi \approx 0^\circ$ and $\phi \approx 180^\circ$, respectively. Here, we have extended the phase (ϕ) axis by a half cycle to better illustrate variations around the maximum northward currents. We accept the velocity and stress estimates as valid if their phase-ensemble averaged magnitudes exceed the $2\sigma/\sqrt{M}$ uncertainty levels, where σ is the standard deviation of the ensemble and M is the number of statistically independent samples. Estimates that exceed this threshold are excluded and masked in gray in Figure 3.9.

As shown in Figure 3.9a,b,e,f, the sea surface height (η) and the alongshore velocities (V) are out of phase by about 45 degrees throughout a tidal cycle. As noted by Arzeno et al. (2018), there was poor coherence ($\mathrm{Coh}^2 = 0.55$) between the sea surface displacement and the velocity signal over the observational period; this accounts for the observed increase in scatter in η (Figure 3.9a,b). The alongshore velocities at 12S were observed to be slightly higher (by about 10% at max velocities) than at 12N. Previous work at Makua has suggested that a large ($\sim$ 3 m) bathymetric step located approximately 25 m south of the mooring site could have resulted in a local acceleration of the flow at 12S (Arzeno et al., 2018). For both sites, the cross-shore velocities (U) are about one order of magnitude smaller than the alongshore velocities, and exhibit a bottom intensified offshore flow (Figure 3.9c,d) as the alongshore flow switches from northward to southward ($\phi \approx 90^\circ$).

Consistent the theory for wall-bounded turbulent flows, the below-wave band vertical ($\overline{v'w'}$) Reynolds stress estimates (Figure 3.9i,j) are in phase with the alongshore velocities (V), and exhibit maximum magnitudes near the bottom for southward flow at both sites, coincident with the region of maximum vertical shear $S = ((\partial V/\partial z) + (\partial U/\partial z))^{1/2}$ (Figure 3.9g,h). For

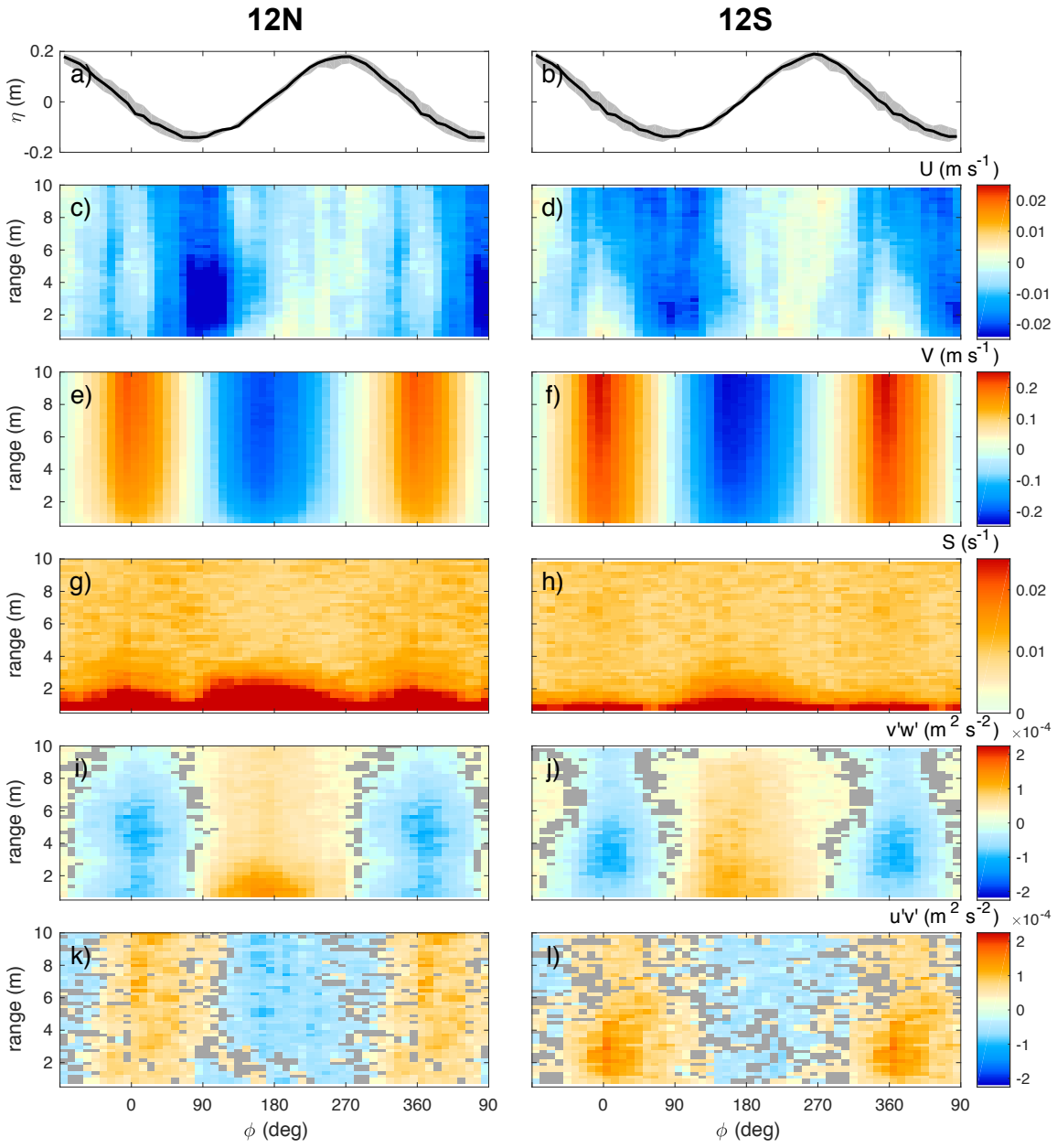

Figure 3.9: Phase-ensemble averages of (a)–(b) sea surface height; (c)–(d) cross- and (e)–(f) alongshore velocities; (g)–(h) vertical shear magnitude; (i)–(j) vertical and (k)–(l) lateral below-wave band Reynolds stress estimates for (left) 12N and (right) 12S ADCPs. Shaded regions in (a)–(b) show the 95% confidence intervals. Regions where the standard error exceeds the magnitude of the phase-averaged values are masked in gray on (i)–(l).

northward flow, however, the maximum vertical stress magnitudes occur away from the bed, at a range of about 5 and 3 m.a.b. for 12N and 12S, respectively. Note that, for northward flow ($315^\circ \lesssim \phi \lesssim 45^\circ$), the magnitude of the vertical shear (S) does not exhibit a corresponding increase (Figure 3.9g,h). This deviation suggests that vertical Reynolds stresses were modified by advection. We emphasize that these advective patterns are tidally coherent, and appear to have a characteristic vertical structure that varies as a function of tidal phase. It is therefore likely that the heterogeneous bathymetry in the vicinity of the ADCP locations (Figure 3.1) is playing an important role in producing the observed structural features of the fluctuating flow. Consistent with the present findings, prior field studies conducted in reef morphologies with highly variable bathymetry, have noted that advective acceleration can provide a non-negligible contribution to the local momentum budget (e.g., Rogers et al., 2015; Arzeno et al., 2018). This issue will be revisited in section 3.4.

Results in Figure 3.9l, show an intensification in lateral stress ($\overline{u'v'}$) matching the location of maximum vertical stress for northward flow, and a relatively uniform vertical structure for southward flow at 12S. On the other hand, the lateral stress distributions at 12N exhibit a nearly uniform vertical structure across all phases, with a slight intensification in $\overline{u'v'}$ toward the surface for northward flow (Figure 3.9k). From Figure 3.9i–l, it is apparent that the vertical and lateral stress components are comparable in magnitude. Furthermore, estimates of $\overline{u'v'}$ (Figure 3.9i,j) appear to be roughly in phase with $\overline{v'w'}$ and V, suggesting that the lateral stress estimates ($\overline{u'v'}$) could be related to the bottom-generated turbulence. This idea is explored further in the next section.

3.3.5 Model for lateral Reynolds stress

Following the turbulent-viscosity hypothesis (Pope, 2000), we relate the depth-averaged lateral Reynolds stresses to the cross-shore gradient of the mean alongshore velocity field

$$\widehat{u'v'} = -\nu_t \frac{\partial V}{\partial x}, \tag{3.21}$$

where ν_t is a turbulent eddy viscosity, $\partial V/\partial x$ is the cross-shore gradient of the depth-averaged alongshore flow, and $\widehat{u'v'}$ is a lateral stress. To quantify the cross-shore gradient of the alongshore flow, we use depth- and spatially-averaged velocity measurements from three autonomous underwater vehicle (AUV) surveys conducted at the Makua forereef on 6–8 September 2013, as described in Chapter 4. Briefly, AUV-based alongshore velocities are spatially-averaged using a cross-shore averaging length of 120 m. Because the AUV data covers roughly 60% of the tidal cycle, the depth-averaged alongshore flow is reconstructed for the full tidal cycle by fitting a sinusoid with the AUV data over a range of cross-shore locations. The cross-shore gradient of the alongshore flow ($\partial V/\partial x$) is then computed at ADCP locations from the reconstructed velocity field (Figure 3.10a). Analysis in Chapter 4 indicates that $\partial V/\partial x$ is caused by cross-shore variations in bottom drag.

From dimensional considerations, the eddy viscosity, ν_t, should be proportional to the product of a characteristic turbulent length scale λ_t and a turbulent velocity u_t. Here, we consider three simple alternatives to represent the eddy viscosity:

$$\nu_{t1} = \alpha_1 \left|\overline{v'w'}\right|^{1/2} \lambda_{0uv}, \qquad \nu_{t2} = \alpha_2 \left|\frac{\partial V}{\partial x}\right| \lambda_{0uv}^2, \qquad \nu_{t3} = \alpha_3 \left(C_D V^2\right)^{1/2} h, \tag{3.22}$$

where $\alpha_{1,2,3}$ is a proportionality constant of order unity (in Figure 3.10, $\alpha_{1,2,3} = 1$), C_D is a nondimensional drag coefficient for depth-averaged flow, h is the local water depth.

The resulting eddy viscosity models for ADCP 12N are plotted in Figure 3.10b as a

function of tidal phase. The first formulation in (3.22) (solid blue line in Figure 3.10b) assumes an eddy viscosity that is modulated by vertical stress, with a characteristic turbulent velocity given by $u_t \sim \left|\overline{v'w'}\right|^{1/2}$. The second formulation in (3.22) (dashed blue line in Figure 3.10b) assumes a conventional mixing length approach, in which the turbulent velocity is driven by lateral shear $u_t \sim |\partial V/\partial x|\lambda_{0uv}$. Similar to ν_{t1}, the third formulation in (3.22) (dash-dotted blue line in Figure 3.10b) scales with the bottom turbulence $u_t \sim V\sqrt{C_D}$. Note that for both ν_{t1} and ν_{t2}, the turbulent lengthscale is given by $\lambda_t \sim \lambda_{0uv}$, a measured quantity determined from the lateral stress cospectra (see Figure 3.7b). In contrast, the turbulent lengthscale for ν_{t3} is given by the local water depth $\lambda_t \sim h$. Note also that $\nu_{t1,3}$ are roughly in phase with the alongshore flow, whereas ν_{t2} lags $\nu_{t1,3}$ as it varies more closely with $|\partial V/\partial x|$.

Figure 3.10c shows a comparison between the modeled ($\widehat{u'v'}_{1,2,3}$) (blue lines) and measured ($\overline{u'v'}$) lateral stress estimates for ADCP 12N (thick black line). The modeled lateral stresses are obtained by substituting (3.22) in (3.21), with order one constants chosen at $\alpha_1 = \alpha_2 = \alpha_3 = 1$. Analysis in Chapter 4 gives a drag coefficient $C_D = 0.0081 \pm 0.0025$ in the vicinity of ADCP locations, which is used here. The water depths at 12N and 12S are 13.2 and 11.7 m, respectively, as shown in Table 3.1.

From Figure 3.10c, it is apparent that the shapes of the predicted lateral stress profiles agree well the observational data, with correlation coefficients (r^2) of 0.89, 0.81, and 0.84 for $\widehat{u'v'}_1$, $\widehat{u'v'}_2$, and $\widehat{u'v'}_3$, respectively. Similar results were obtained for ADCP 12S (not shown), with slightly higher correlation coefficients in all cases: 0.92, 0.85, and 0.89 for $\widehat{u'v'}_1$, $\widehat{u'v'}_2$, and $\widehat{u'v'}_3$, respectively. A statistical comparison (Hittner et al., 2003; Zou, 2007; Diedenhofen and Musch, 2015) of the correlation coefficients associated with $\widehat{u'v'}_1$ and $\widehat{u'v'}_2$ showed the relationships to be significantly different (p-value< 0.001). No statistically significant differences were found between the correlation values corresponding to $\widehat{u'v'}_1$ and $\widehat{u'v'}_3$ (p-value> 0.05). The similarity among the correlations is not surprising, given that both $\partial V/\partial x$ and $\overline{v'w'}$ are largely determined by V. The difference between $\widehat{u'v'}_2$ and the other quantities ($\overline{u'v'}$, $\widehat{u'v'}_1$, $\widehat{u'v'}_3$) is primarily associated

with the slight phase shift in $\partial V/\partial x$ (note that $\widehat{u'v'}_2$ is more heavily weighted towards $\partial V/\partial x$). Overall, these results suggest that there is a stronger association between $\overline{u'v'}$ and $\widehat{u'v'}_{1,3}$.

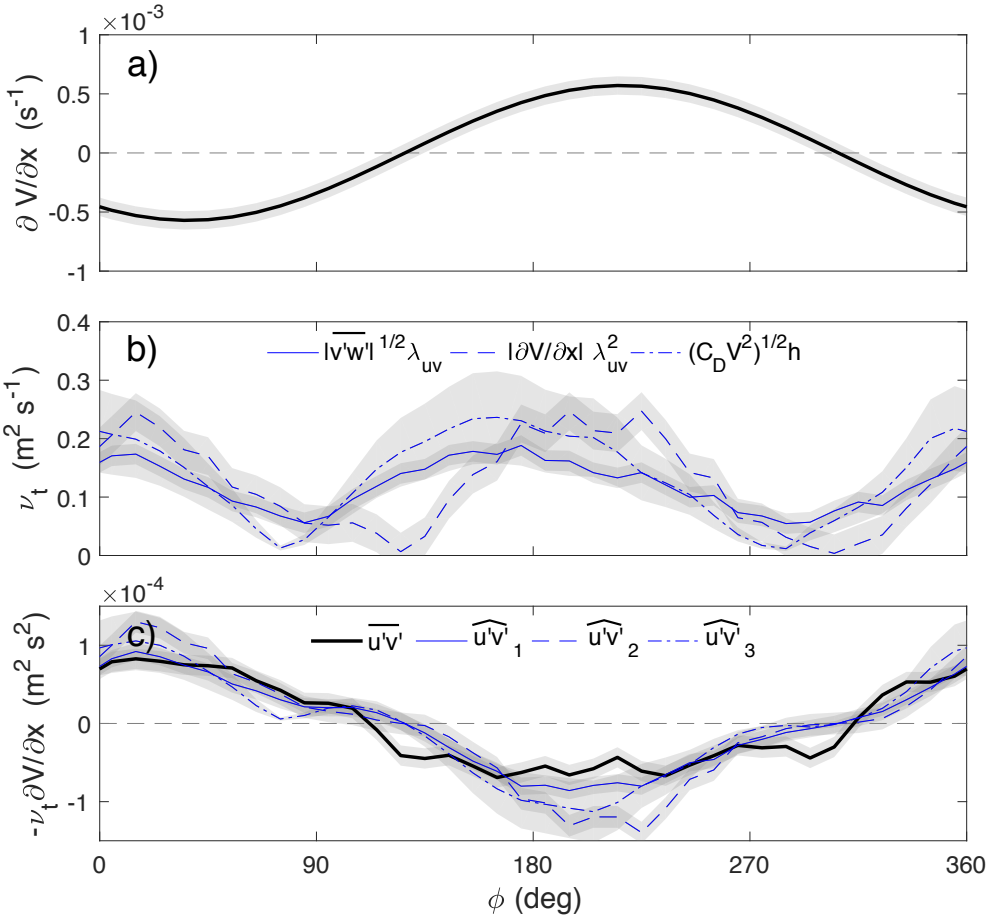

Figure 3.10: (a) Cross-shore gradient of the depth-averaged alongshore flow at the 12 m isobath from AUV spatial velocity measurements; (b) three eddy viscosity models in (3.22); and (c) corresponding lateral stress models (3.21) (blue lines) along with the phase- and depth-averaged lateral Reynolds stress estimates for the 12N ADCP (thick black line). Shaded regions indicate the 95% confidence intervals calculated via bootstrapping and error propagation, as described by Emery and Thomson (1997).

3.4 Discussion and conclusions

The present study represents one of the first attempts to quantify the vertical structure of the lateral Reynolds stresses in the coastal ocean. In this work, we have extended the ADCP

variance method using a rearrangement of the beam variance equations to create an expression for $\overline{u'v'}$, and modified existing wave-turbulence decomposition strategies (Kirincich et al., 2010) to enable robust estimates of the below-wave band lateral Reynolds stresses ($\overline{u'v'}$) in the presence of surface gravity waves. Assessment of the proposed method via comparisons with independent ADV-based stress estimates at the 12N and 12S moorings showed good quantitative agreement over the tidal cycle (Figure 3.8), confirming that ADCPs can effectively resolve lateral turbulent fluxes and isolate them from wave-induced errors. Furthermore, results in Figure 3.5 indicate that most of the turbulent covariance is explained by low frequencies (below the wave band) turbulent motions. Therefore, below-wave band estimates of $\overline{v'w'}$, k_{0vw}, and of $\overline{u'v'}$, k_{0uv}, determined empirically from the phase-averaged cospectra, can be interpreted and assessed with confidence as reasonably accurate representations of the actual phase-averaged values. Note, however, that these estimates represent local values obtained by point sensors and are not necessarily representative of reef-scale averages due to the highly irregular and complex reef topography (Trowbridge and Lentz, 2018). We discuss below limitations in the proposed method as well as the implications of the results.

3.4.1 Method limitations

The applicability of the variance method for lateral stress measurements (3.4) is particularly limited by the instrument orientation relative to the flow direction (section 3.2.2) and by the measurement uncertainty (section 3.2.2). In this study, both the orientation of the ADCPs (12N, 12S) relative to the alongshore flow and the hydrodynamic conditions were particularly well suited for testing our technique and for elucidating the vertical structure of the lateral Reynolds stresses. Instrument misalignment leads to cross-contamination among the beam velocities (Dewey and Stringer, 2015), and complicates the extraction of the "true" $\overline{u'v'}$ stress term. Alternatively, one could calculate lateral stresses directly from the fluctuating part of the Cartesian u and v velocities; however, this would require the assumption of spatial homogeneity, and would further increase

the size of the minimum observable turbulent length scales (section 3.2.2). As for the uncertainty errors, it was found that lateral stress uncertainties were higher than the stress estimates for a significant fraction of the bursts, and about 2.8 times higher than the vertical stress uncertainties (Figure 3.4). However, phase ensemble averaging substantially reduced the lateral stress uncertainties, resulting in standard errors well below the estimated Reynolds stresses for the majority of the ensembles (Figure 3.9k,l).

The spectral wave-turbulence decomposition technique described in this study is also limited by the properties of the wave field because the unsteady advection of turbulence by wave orbital velocities can alter the shape of the observed cospectrum. To ensure viable stress estimates and limit the kinematic effects of wave orbital motion, we restricted our observations to instances when $\sigma_w/|v_c| < 2$ and $\sigma_w k_0/\omega_w < 0.5$. Analysis by Rosman and Gerbi (2017) predicts that under such conditions, at least 80% of the turbulent covariance is expected to reside at frequencies below the wave peak. However, it is important to bear in mind that these screening criteria effectively bias our observations towards times of more energetic flows and weaker waves (Kirincich et al., 2010; Kirincich, 2013). As a result, it is unknown whether the influence of energetic surface waves affects the magnitude and vertical structure of the observed lateral stresses, though wave forcing is expected to enhance the near-bed vertical stresses and increase bottom drag (Lentz et al., 2018; Scully et al., 2018).

3.4.2 Implications of the results

Results presented in Figure 3.9i–l illustrate the vertical structure of the tidally-averaged turbulent Reynolds stresses resulting from well-mixed (unstratified), tidally-driven flow over rough coral reef bathymetry for weak swell conditions ($H_s \lesssim 0.6$ m) (Figure 3.2). Observations of the vertical stress (Figure 3.9i,j) show that $\overline{v'w'}$ does not coincide with regions of vertical shear (S) over a significant fraction of the tidal cycle. This is indicative of local imbalances between production and dissipation of turbulent kinetic energy, and suggests non-negligible

contributions from advective transport. Indeed, Arzeno et al. (2018) has reported that advective acceleration plays an important role in the local momentum budget at Makua, and is necessary for budget closure at 12S. Recent studies have shown that irregular roughness induces spatial gradients in the Reynolds stresses and promotes the production of turbulent kinetic energy in preferential regions, which requires the presence of secondary advective velocities (Mejia-Alvarez and Christensen, 2013; Barros and Christensen, 2014; Anderson et al., 2015). Notably, Rogers et al. (2015) suggested that a similar mechanism was likely responsible for the formation of secondary circulations over spur and groove morphology. Thus, it is likely that the complex, multi-scaled bathymetric nature of spur and groove formations results in Reynolds stress distributions that are highly variable in space, and lead to advective transport by virtue of secondary flows.

For the Makua site, the cross-shore structure of the mean alongshore velocity and the associated lateral shear are determined by cross-shore variations in bottom drag (Chapter 4). Work by Vermaas et al. (2011) and Willingham et al. (2014) indicate that lateral variations in bottom roughness and the resultant wall stress distribution induce a corresponding lateral shear, which facilitates a lateral momentum exchange via $\overline{u'v'}$. This is consistent with results in Figure 3.9k,l, which show a detectable lateral stress ($\overline{u'v'}$) signal that is sustained by a cross-shore gradient in the alongshore velocity (Figure 3.10a) and that extends throughout the water column.

Using the estimated turbulent quantities ($\overline{v'w'}$, $\overline{u'v'}$, λ_{0uv}), the lateral gradient of the depth-averaged alongshore velocity ($\partial V/\partial x$), and assuming a turbulent-viscosity framework (3.21), we tested three simple eddy viscosity (ν_t) formulations (3.22) to help elucidate the underlying mechanisms responsible for generating the observed lateral stresses. The first two formulations (ν_{t1}, ν_{t2}) were based on estimated turbulent quantities, whereas the third one (ν_{t3}) was based on a solely parametric formulation. Although all three models satisfactorily reproduce the observed depth-averaged lateral stresses (Figure 3.10c), the results indicate that the proposed bottom generated turbulence models ($\widehat{u'v'}_1$, $\widehat{u'v'}_3$) are marginally better than the lateral mixing length model ($\widehat{u'v'}_2$) at capturing the phase variations in the estimated lateral stresses. The idea

that bottom-driven turbulence modulates $\overline{u'v'}$ is also consistent with the experimental results in Figure 3.7, which show that the stress-carrying turbulent length scales are on the order of the local water depth $O(10\text{ m})$ and not on the scale of the coastal boundary layer $O(1000\text{ m})$; thus, implying a potential connection between the bottom-driven turbulence and horizontal turbulence. Further research is required to examine more closely the links between $\overline{v'w'}$, $\overline{u'v'}$, and ν_t in flow over rough topography.

Finally, with regard to cross-shelf transport, the role of the lateral Reynolds stresses can be compared to cross-shore advective transport via a Péclet number

$$Pe = \frac{UL_x}{\nu_t} \sim 10^2, \tag{3.23}$$

where $L_x \sim 10^3$ m is the cross-shore distance to the ADCPs, and $U \sim 10^{-2}$ m s^{-1} and $\nu_t \sim 10^{-1}$ m^2 s^{-1} from our observations (see Figures 3.9c,d and Figures 3.10b). From (3.23) we can conclude that, at Makua, the lateral transport by turbulent mixing is negligible in comparison to the lateral advective transport over the course of the tidal cycle. However, it is worth noting that, at Makua, the lateral turbulent diffusivity is in phase with the alongshore flow, and usually out of phase with the cross-shore tidal velocities; hence, lateral turbulent diffusion may dominate over cross-shore advective transport when the tidal cross-shore velocities are at their minimum. Moreover, turbulent diffusion is an irreversible mixing process, as opposed to advective transport, which is a dispersive and reversible process. Furthermore, if we allow the eddy viscosity to scale as ν_{t3} in (3.22) (assuming $\lambda_{0uv} \sim h$), then we may rewrite (3.23) as

$$Pe_3 = \frac{U}{\alpha_3 C_D^{1/2} V \beta},$$

where $\beta = h/L_x$ is the cross-shore seafloor slope. For the observed conditions at Makua ($\alpha_3 = 1$, $C_D \sim 0.01$, $\beta \sim 0.04$, $V \sim 10^{-1}$ m s^{-1}), this gives $Pe_3 = 25$. This suggests that lateral transport by turbulent mixing could be relevant to an important subset of coral reef shelves: those with

sufficiently steep slopes and rough bottoms, which are typical features of many fore-reefs around the world (e.g., Lewis and Hutchinson, 2001; Rosman and Hench, 2011; Quataert et al., 2015).

3.5 Summary

In this Chapter we have described a new approach to estimate lateral turbulent Reynolds stresses ($\overline{u'v'}$) using ADCPs in wavy coastal environments. We have developed an expression for $\overline{u'v'}$ using a rearrangement of the ADCP beam variance equations (Lohrmann et al., 1990; Stacey et al., 1999a), and adapted existing wave-turbulence decomposition strategies (Gerbi et al., 2008; Kirincich et al., 2010) to isolate the lateral turbulent motions at frequencies below those of surface gravity waves. The performance of the proposed method was evaluated via comparisons with independent ADV-based stress estimates at two sites. Comparisons showed good quantitative agreement over the tidal cycle, indicating that ADCPs can resolve lateral turbulent fluxes via ensemble-averaging. Assessment of ensemble-averaged turbulence cospectra indicates that the proposed approach is effective in isolating the low frequency (below the wave band) turbulent stresses from wave-induced errors.

The vertical structure of the tidally-averaged turbulent Reynolds stresses was examined as a function of tidal phase in an unstratified, tidally-driven flow over a rough coral reef seabed in weak swell conditions. Observations and analysis indicate that the lateral stresses are sustained by the cross-shore (lateral) gradient of the mean alongshore flow, and driven by bottom-generated turbulence. Scaling considerations suggest that cross-shore transport by lateral turbulent mixing could be relevant to coral reef shelves with steep cross-reef slopes and rough bottoms.

3.6 Acknowledgments

This work was funded by the Office of Naval Research via award N00014-13-1-0340, by the Chancellor's Research Excellence Scholarship (formerly FISP), and by the Army Corps of Engineers via a subcontract from the University of California, San Diego (PO 1036151). The authors thank Audric Collignon, Carly Quisenberry, Chris Kontoes, Joe Gilmore, and Christina Comfort for their assistance with field operations in support of the Makua experiments. This work also benefited from conversations with Kristen Davis, Falk Feddersen, and the CSIDE group.

Chapter 3 is currently being prepared for submission for publication (Amador A., Giddings S. N., and Pawlak G., 2020). The dissertation author was the primary investigator and author of this paper.

Chapter 4

Cross-Shore Structure of Tidally-Driven Alongshore Flow over Rough Reef Bathymetry

4.1 Introduction

The nearshore region acts as the interface between the coast and the open ocean, and is of great societal interest and value (Holman et al., 2015). Nearshore flows regulate many ecological processes in coastal marine systems, and are especially vital for coral reefs environments. Hydrodynamic forces influence many reef ecosystem processes, including their growth, health, and metabolism (Lowe and Falter, 2015). For example, reef-scale circulation patterns determine larval retention and dispersal rates (Cowen and Sponaugle, 2009; Wolanski and Kingsford, 2014), and play a primary role in regulating the supply of nutrients (Falter et al., 2004) and the transport of heat (Davis et al., 2011; Pineda et al., 2013; Zhang et al., 2013) between reef and the adjacent ocean. At smaller scales, the turbulent processes associated with wave and current flow over coral reefs modulate nutrient uptake and release rates (Atkinson and Bilger, 1992; Baird and

Atkinson, 1997; Wyatt et al., 2012), particulate capture by coral (Sebens et al., 1998; Hughes and Grottoli, 2013) and reef heterotrophs (Yahel et al., 1998; Genin et al., 2009; Wyatt et al., 2010), and contribute to the overall health of the benthic community (Baird and Atkinson, 1997; Atkinson et al., 2001; Hearn et al., 2001; Monismith, 2007).

A key feature of the nearshore region is that it is typically dominated by alongshore flows due to the presence of a coastal boundary (Lentz and Fewings, 2012). Numerous mechanisms can drive alongshore flows, and different natural settings are often governed by multiple processes that span a diverse range of spatial and temporal scales. It has long been known that obliquely incident waves can force alongshore currents in the surf zone via spatial gradients in radiation stress (Longuet-Higgins and Stewart, 1964), and a considerable amount of work has been devoted to this subject (e.g., Bowen, 1969; Longuet-Higgins, 1970; Thornton and Guza, 1986; Feddersen and Guza, 2003). Offshore of the surf zone, a wide variety of inner-shelf processes have been observed to drive alongshore flows, including winds, tides, buoyant plumes, and waves (Lentz and Fewings, 2012). Historically, most inner-shelf studies have focused on subtidal flow, averaging over intratidal timescales and processes. In such cases, the primary balance for the depth-averaged momentum equations has been shown to be dominated by the wind stress, the along-shelf pressure gradient, and the bottom stress (e.g., Mitchum and Clarke, 1986; Lentz and Winant, 1986; Lentz, 1994; Lentz et al., 1999; Fewings and Lentz, 2010).

For coastal reef systems, most of the work has focused on wave-driven circulation resulting from wave breaking and the ensuing wave setup (Monismith, 2007; Lowe and Falter, 2015). While some studies have examined the role of tidal modulation on wave setup (Lugo-Fernandez et al., 1998; Taebi et al., 2011; Becker et al., 2014) and the hydrodynamics of tide-dominated reef platforms and atolls (Lowe et al., 2015; Green et al., 2018), the hydrodynamics of tidally-driven alongshore flows has received little attention. This raises the question of what is the semidiurnal flow response for coral reef shelves where the tidal pressure gradient is the dominant forcing mechanism. Previous research at the Makua forereef on the western coast of O'ahu, Hawai'i

(Figure 4.1) indicates that the alongshore flow at the 12 m isobath is described on semidiurnal timescales by a balance between the local acceleration, the barotropic pressure gradient, and the bottom drag (Arzeno et al., 2018). We can expect, however, that bottom drag effects will vary with water depth such that the importance of bottom drag will diminish with increasing distance offshore and vice-versa. A spatio-temporal description of the flow structure and the resulting nearshore circulation is lacking. This is in part because reef scale circulation patterns are intrinsically linked to their rough and complex morphologies, and accurately predicting the flow and drag forces over such irregular morphologies remains a major challenge (Rosman and Hench, 2011; Lowe and Falter, 2015; Lentz et al., 2017).

We present autonomous underwater vehicle (AUV)-based spatial velocity measurements along with time series data of the alongshore pressure gradient to examine the cross-shore structure and evolution of a tidally-driven alongshore flow over a fringing coral reef shelf on the western coast of O'ahu, Hawai'i. The present study extends the work of Arzeno et al. (2018) to provide a reef-scale assessment of the hydrodynamics. The main objective of this paper is to examine how cross-shore variations in bathymetry and reef roughness affect the resulting depth-and spatially-averaged flow response. Furthermore, we seek to gain some insight into the hydrodynamically relevant roughness scales for coral reef environments via spatial measurements of benthic roughness. We will show that the primary balance proposed by Arzeno et al. (2018) describes the cross-shore structure and evolution of the depth-averaged alongshore flow, and allows the estimation of an average drag coefficient over the Makua reef shelf (in depths spanning from 24 to 6 m).

This paper is organized as follows. In section 4.2, we provide a general description of the study site, methods, and observations used in this study. In section 4.3, we analyze the fixed- and AUV-based field measurements, and formulate a simple 1D flow model that incorporates the effects of waves on the bottom drag. We compare predicted and observed results in section 4.4. Results are interpreted and summarized in sections 4.5 and 4.6, respectively.

4.2 Field measurements

4.2.1 Study site

The Makua reef site (21.510°, −158.236°) is located about 2 km south of Makua Beach on the leeward side of O'ahu, Hawai'i (Figure 4.1b). Bathymetric contours at Makua are oriented roughly north-south with a fairly constant cross-shore seafloor slope of about 4% between the 10 and 24 m isobaths; beyond this limit, the forereef bathymetry drops off sharply in the offshore direction. Towards the shore, the bathymetry slopes up more gradually at about 2% between the 9 m and 6 m isobaths, and then remains relatively flat at an average depth of 6 m for around 400 m. Shallower than 6 m, the inner reef flat diminishes steadily at 3% towards shore for about 200 m. The shoreline at Makua is primarily composed of carbonate sand and limestone rock (Fletcher et al., 2012). The bottom substrate inshore of the 15 m isobath is largely comprised of rough coral reef interspersed with sandy coral rubble. The forereef slope features generally shore-normal, alongshore periodic spur and groove formations (see Figures 4.1a and 4.3). The coral features give way to a smoother sandy bed at depths between 15 and 24 m.

Field observations were carried out on the Makua forereef in late summer 2013. A series of six REMUS-100 (Hydroid Inc.) AUV surveys, conducted over two consecutive spring tides, targeted the spatial evolution of the mean alongshore flow in response to tidal forcing and benthic roughness distributions using altimeter profiling. Field data from moored instrumentation were collected as described in Arzeno et al. (2018), and targeted the resolution of flow hydrodynamics over the forereef region in varying wave and current conditions. A brief summary of the observational array is presented next.

4.2.2 Fixed measurements

Two SBE 26 pressure sensors were deployed from 21 August to 30 September 2013 at depths of 12.2 and 13.6 m, separated by a distance of about 2 km in the alongshore direction (Fig-

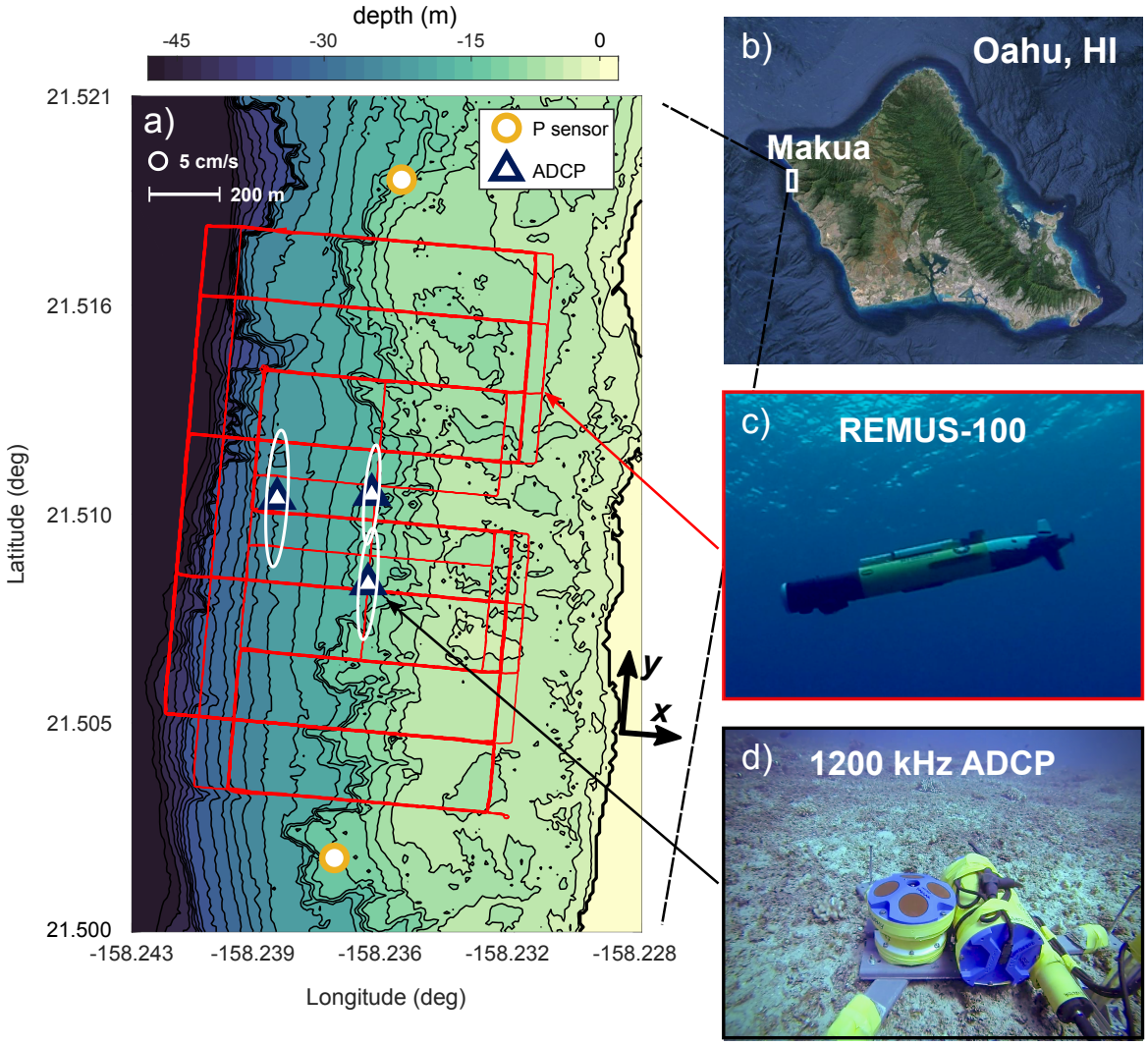

Figure 4.1: (a) Makua study site and survey region with SHOALS LIDAR bathymetry, (b) satellite image (Google Earth) of O'ahu, Hawai'i and the Makua study site location, (c) REMUS-100 AUV, and (d) 1200 kHz ADCP at 12S. Red lines in (a) show tracks followed by the AUV during hydrodynamic surveys. Locations for ADCP and pressure sensors are shown by blue triangles and yellow circles, respectively. Principal component ellipses (white) at ADCP locations show depth-averaged tidal velocity (radii of ellipses represent one standard deviation). The coordinate system (x, y) defines the cross- and alongshore directions, respectively, and is consistent with the principal axes of the flow (5° from true north).

ure 4.1a); both pressure sensors sampled continuously at 1 Hz. An array of bottom-mounted RDI Workhorse acoustic Doppler current profilers (ADCPs) (Figure 4.1d) and co-located thermistor chains (SBE 56, Seabird Electronics) were deployed for a period of four weeks beginning on 6 September 2013. This latter deployment included two 1200 kHz ADCPs (12N and 12S) moored 260 m apart near the 12 m isobath, and a third 300 kHz ADCP (20W) deployed 270 m offshore of 12N, near the 20 m isobath (see Figures 4.1a and 4.2). The inshore ADCPs (12N and 12S) sampled water velocities continuously at 0.5 Hz in 0.25 m bins beginning at 0.8 m above the bottom. The offshore ADCP (20W) was configured to sample at 0.5 Hz in 1.25 m bins beginning at 3.25 m above the bottom. Thermistor chains (T-chains) near 12N and 20W measured water temperatures in 1 and 2 m intervals, respectively, from 0.30 m above the bed to 1 and 2.6 m below the surface at 2 Hz.

Time series data from fixed instruments were averaged using 20-min intervals with a 50% overlap, and interpolated onto a common time base. ADCP velocity measurements were rotated into the cross- and alongshore (x, y) coordinate system shown in Figure 4.1a, which is roughly parallel with the principal axes of the flow (5° from true north). SBE 26 pressure gauge data were de-meaned to estimate sea surface deviations (η) about the mean sea level at each location. The alongshore pressure gradient was estimated as $g\Delta\eta/\Delta y$, where $g = 9.8$ m s^{-2} is gravitational acceleration, $\Delta\eta$ is the sea level difference, and $\Delta y \approx 1950$ m is the alongshore distance between the north and south pressure gauges (Figure 4.1a). We assume a hydrostatic balance in the vertical, with no significant instrument drifts (or deviations) over the deployment. Atmospheric pressure is assumed to be identical at the two sensors, and hence does not contribute to the gradient. Pressure sensors were located well outside of the surf zone, where the effects of wave-driven setup and setdown were not notable, and synchronized in time to resolve small phase differences in the sea surface signal. Significant wave heights (H_s) and peak wave periods (T_p) were estimated from SBE 26 pressure spectra over the sea-swell frequency band (3–22 s) using linear wave theory.

4.2.3 Hydrodynamic surveys

Spatial hydrodynamic surveys were conducted on 6–8 September 2013 with concurrent velocity observations from the fixed ADCP array to examine spatio-temporal variations in flow velocities. Surveys, carried out using a REMUS 100 (Hydroid Inc.) autonomous underwater vehicle (Figure 4.1c), consisted of mow patterns with repeated transects in both the cross- and alongshore directions in water depths ranging from 5 to 30 m (Figure 4.1a). The REMUS-100 AUV was outfitted with upward- and downward-looking 1200 kHz RDI Doppler velocity logs (DVLs) configured to sample water velocities in 1-m bins starting at 1 m above and below the vehicle's depth, at a sampling frequency of approximately 0.67 Hz. Hydrodynamic surveys spanned an alongshore distance of about 1600 m, with cross-shore transects ranging from about $-1300 < x < -400$ (where $x = 0$ at the shoreline, as shown in Figure 4.1a). The vehicle maintained a constant depth of 3 m below the sea surface and was set to cruise at 2 m s^{-1}. Table 4.1 provides additional details about the hydrodynamic surveys (H1–H3).

Previous studies of ship- and AUV-based velocity measurements have reported on the presence of a velocity bias in the direction of the vehicle motion (e.g., Fong and Monismith, 2004; Fong and Jones, 2006; Jaramillo and Pawlak, 2010; Amador et al., 2017). Moreover, surface gravity waves have been shown to affect the vehicle trajectory, and in turn the AUV-based velocity measurements, by introducing a quasi-Lagrangian bias in the direction of wave motion that is related to Stokes drift (Amador et al., 2017). Here, we focus on cross-track velocities from cross-shore transects, such that measurements are not affected by along-track biases. In addition, because incident wave angles (θ_w) (relative to the cross-shore) were small over H1–H3 sampling period (Table 4.1), wave-induced biases are expected to be negligible.

AUV-based velocity data collected during the H1–H3 surveys (see Table 4.1) were rotated into along- and cross-shore components for each transect, and spatially-averaged over 120 m. DVL data near the bottom and sea surface boundaries (around 11% of range to boundary) were rejected to avoid acoustic contamination by side lobe reflections. Velocity data were excluded

when DVL bottom-tracking errors exceeded 10 cm s^{-1}. Vertical averages of the alongshore velocity were then computed using spatially-averaged data (120 m) from cross-shore transects. Uncertainty in measurements for the alongshore velocity component were largely dominated by the alongshore component of wave-induced motions, as described by Amador et al. (2017). Standard errors for vertically- and spatially-averaged (120 m) alongshore velocity measurements ranged from 1 cm s^{-1} to 2.5 cm s^{-1} in deep (24 m) and shallow (5 m) survey regions, respectively, consistent with the effects of wave shoaling over the reef shelf. To account for missing data near the surface and bottom boundaries as well as in the region immediately in front of the DVL transducers, AUV-based depth-averaged velocities were corrected using an empirical scaling factor derived from the ADCP velocity profiles at 12N, 12S, and 20W, as described in Appendix B.

4.2.4 Bathymetry

In addition to the hydrodynamic surveys described above, additional AUV surveys were carried out on 22–24 August 2013 (R1–R3) targeting benthic roughness. The AUV was equipped with a custom narrow beam (2.5° beam width) altimeter (Imagenex Technology Corp.) that featured range (vertical) resolution of about 1 cm. Range data from the echosounder were collected at 18 Hz, yielding an along-track resolution of 8-10 cm at survey speeds of 1.5 m s^{-1}. For the benthic roughness surveys, the vehicle was programmed to maintain a constant altitude at a nominal height above bed of 4 meters. Over the three surveys, the vehicle covered the same region resolved by the hydrodynamic surveys (Figure 4.1a) using a mow pattern with leg spacings of roughly 25 to 50 m in the cross-shore direction and 100 m in the alongshore direction (see gray dots in Figure 4.3).

Along with roughness data collected from AUV surveys, bathymetry and roughness estimates were obtained using data from the publicly available 2013 NOAA Oahu topographic LIDAR data set (https://data.noaa.gov/dataset/dataset/2013-noaa-oahu-topographic-lidar). Briefly, bathymetric data is obtained from aircraft using laser ranging for depths that can extend beyond

50 m in clear waters (Irish and Lillycrop, 1999; Guenther et al., 2000). The data set extracted for the Makua region has an average density of 2.7 points per square meter between 0 and 40 m depth. Because of overlapping LIDAR swaths, the data coverage is not uniform in space, with alongshore averaged densities below 2 points per square meter between overlapping areas to as high as 6 points in areas closer to shore. LIDAR data was gridded onto a 2 m (x, y) square grid spanning the study region (Figure 4.1a) with an average of 10.8 points per bin contributing to the averaged depth.

4.2.5 Overview of observations

Details on conditions for the observational period are provided in Arzeno et al. (2018). As a brief summary, the four-week observational period (6 September to 3 October 2013) featured moderate swell conditions with minimal short-period wave energy, light offshore winds, a mixed-semidiurnal surface tide, and a dominant semidiurnal pressure gradient with strong semidiurnal alongshore velocities and significantly weaker cross-shore velocities. Alongshore currents at Makua were largely directed along isobaths, with faster flows occurring offshore (see tidal ellipses in Figure 4.1a). For the H1–H3 survey period, depth-averaged alongshore velocity amplitudes observed at the 12 and 20 m moorings were around 0.3 m s^{-1} and 0.4 m s^{-1}, respectively (see Figure 3 in Arzeno et al. (2018)); and tidal amplitudes (η) were on average around 0.15 m. Gradient Richardson number (Ri) estimates at the 12N and 20W T-chains indicate vertically well-mixed (unstratified) conditions, with values well below $\mathrm{Ri} < 0.25$ over 95% of the sampling time (Arzeno et al., 2018). Similar conditions were observed during the AUV hydrodynamic surveys (H1–H3). Additional details about the sea state conditions are provided in Table 4.1.

Spectral analysis indicates that alongshore velocities at Makua have a much clearer coherence with the pressure gradient than with the sea surface displacement, with maximum energy at semidiurnal frequencies (Arzeno et al., 2018). Previous studies have identified the Hawaiian Ridge (Merrifield et al., 2001; Rudnick et al., 2003) and the Kaena Ridge (located about

Table 4.1: AUV Hydrodynamic Survey Details.

Survey	Dates	N[a]	Duration (hr)	Phase[b] (deg)	H_s^c (m)	T_p^c (s)	θ_w^c (deg)	Λ_0^d (m s^{-2})	V_0 (m s^{-1})
H1	06-Sep-2013	22	4.7	145°–285°	0.60	12.2	−1°	6.9×10^{-5}	0.47
H2	07-Sep-2013	29	5.2	94°–242°	0.47	13.8	6°	5.3×10^{-5}	0.39
H3	08-Sep-2013	29	4.0	70°–187°	0.43	12.3	8°	5.2×10^{-5}	0.37

[a]Number of cross-shore transects.
[b]Phase as defined in section 4.3.2.
[c]Wave conditions at SBE pressure sensors.
[d]Amplitude of the pressure gradient as defined in section 4.3.2.

45 km west-northwest of Makua; Carter et al., 2008; Nash et al., 2006) as sites of significant barotropic-to-baroclinic tidal energy conversion at semidiurnal frequencies. The relatively small tidal amplitudes at Makua and its exposure to tidal generation sources suggest that the observed pressure gradient and the associated alongshore velocities are likely driven by a semidiurnal internal tide propagating in deeper stratified waters offshore (Arzeno et al., 2018). Prior studies have reported on similar energetic semidiurnal tidal currents at other nearshore locations around the island of O'ahu (e.g., Sevadjian et al., 2012; Smith et al., 2016).

A series of cross-shore sections from the H3 AUV survey over the Makua reef (Figure 4.2) reveals the evolution of the alongshore flow in response to the changing tidal pressure gradient. Initially, the flow is directed northward (red tones) across the reef (Figure 4.2a,b). As the pressure gradient switches direction, the nearshore flow begins to accelerate southward (blue tones) before the offshore flow (Figure 4.2c,d,e). At the end of sequence, the flow has undergone a complete reversal across the reef (Figure 4.2f). The spatial evolution of the alongshore velocity structure exhibits characteristics of an oscillatory boundary layer (e.g., Panton, 2013; Schlichting and Gersten, 2016), with the nearshore and near-bed flow leading the outer flow in phase. The dynamics of this system will be examined in Section 4.3.3.

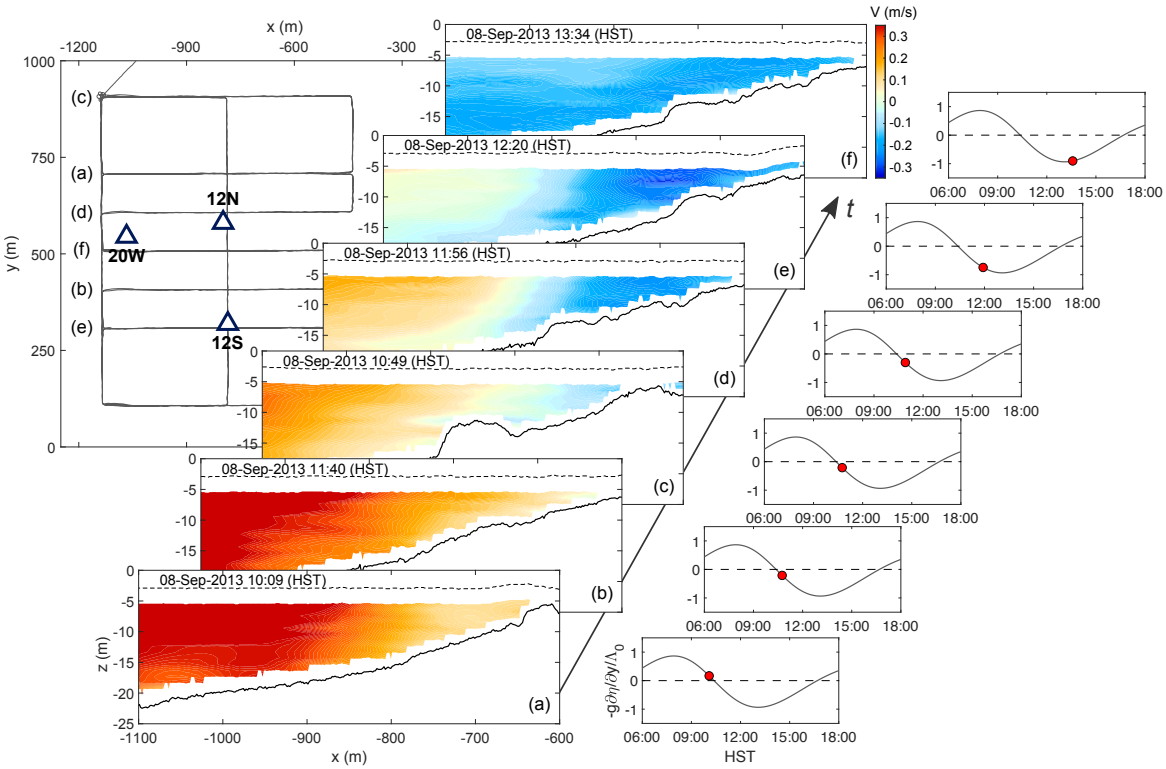

Figure 4.2: left: AUV tracks (gray line) and locations of the ADCP array (triangles: 12N, 12S and 20W) for a hydrodynamic survey (H3) conducted over the forereef slopes of Makua on 8 September 2013. center: Tidal flow evolution of the along-shore velocity captured by the REMUS-100 AUV during a sequence of cross-shore transects. Velocity data was spatially-averaged over 120 m; red and blue tones indicate northward and southward flow, respectively. Note that the letters (a)–(f) in the center panel correspond to transect labels shown in the left panel. right: Normalized pressure gradient ($-g\partial\eta/\partial y/\Lambda_0$, where Λ_0 is the pressure gradient amplitude) filtered via complex-demodulation as a function of time (solid gray line) with the corresponding value for each transect (red circles).

4.3 Analysis

4.3.1 Benthic roughness

Bottom range data from the AUV and LIDAR were processed to characterize variations in bottom roughness. Here, we use root mean square (rms) values derived from spectral variance within selected wavenumber bands as a proxy for bed roughness (Nunes and Pawlak, 2008). Though the link between rms and physical roughness is not direct, as shown by Rogers et al. (2018), spectral variance provides a simple tool for describing variability in roughness. Here the objective is to relate observations of drag to general scales and patterns of roughness.

Altitude data from the AUV altimeter were preprocessed to minimize the effects of spurious measurements. Outlier data, as identified based on a two-standard deviation threshold relative to a three-point median filter, are removed. Altitude data was further masked based on vehicle attitude, excluding points where vehicle pitch or roll exceeded ± 10 degrees and where changes in pitch or roll exceeded a threshold of 1 degree between measurements.

Spatial data series from all surveys were then split into 32 m segments with 16 m overlap, wherever masked data were free from gaps larger than 0.5 m. Gaps smaller than 0.5 m were linearly interpolated. The final percentage of points replaced by interpolation was minimal ($2-7\%$ per survey). A total of 3771 32 m segments were obtained from the three benthic survey missions. From these, segments where standard deviations in pitch, roll or heading exceeded thresholds (1.5, 1.5 and 4.0 degrees, respectively) were flagged as invalid to further minimize effects of vehicle motion. A total of 2326 'good' segments were considered for the approximately 1.5 x 2.0 km survey region from the three surveys. Data segments were further classified based on vehicle heading yielding 442 along- and 1884 cross-shore segments. Locations of these segments are shown in Figure 4.3 overlaid on the alongshore gradient in the 2 m gridded LIDAR data.

The power spectral density $S(k)$ is calculated for each 32-m AUV survey segment as a function of wavenumber k, after detrending, interpolating onto a regular 2 cm grid and window-

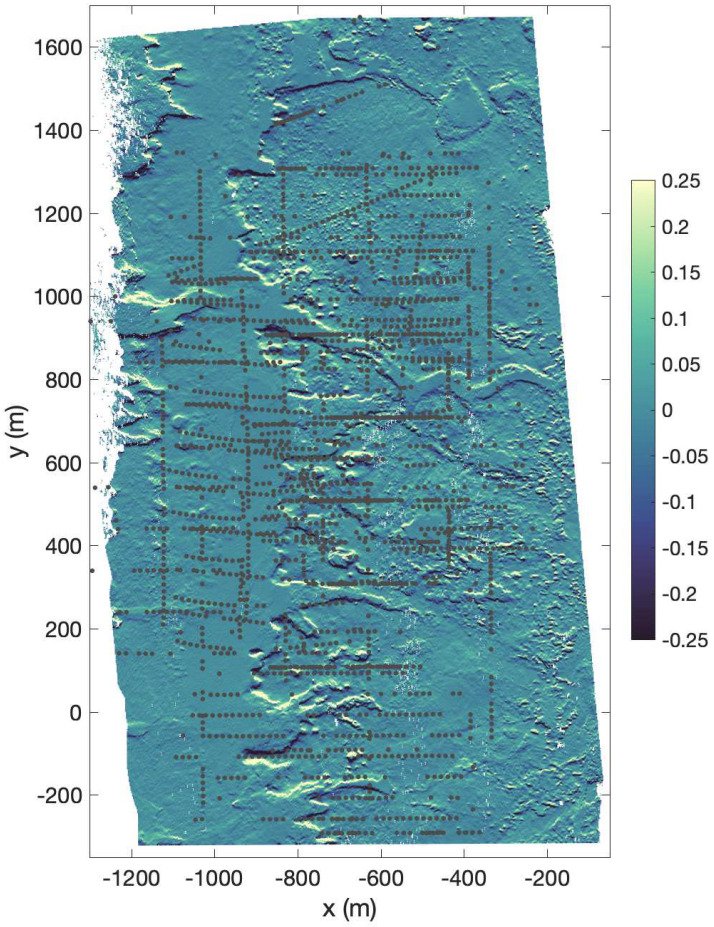

Figure 4.3: Map of the alongshore gradient ($\partial h/\partial y$) for the 2 m gridded LIDAR bathymetry data at Makua showing the variability in roughness. Gray dots indicate central locations of the AUV-based data segments used to compute bottom range spectral variance.

ing with a Hamming function. The spectral rms roughness is then calculated within selected wavenumber bands as

$$R_{B_i}^2 = \int_{k_{i_1}}^{k_{i_2}} S(k)\, dk\,, \tag{4.1}$$

where k_{i_1} and k_{i_2} are the upper and lower wavenumber limits, respectively. The integral in equation (4.1) is calculated from the discrete power spectral density using a trapezoidal method.

The 2 m gridded LIDAR data was also analyzed for spectral content. Isolated empty grid points were replaced with the median of neighboring boxes (0.3% of boxes). Alongshore and cross-shore segments of 128 m in length with 50% overlap, were then extracted from the gridded data, yielding over 39,000 segments in each direction. Spectral rms was calculated from these as given in (4.1).

Limitations in the raw data spatial resolution constrain the AUV data to wavelengths between 0.2 and 16 m, whereas the LIDAR data is valid over wavelengths between 4 and 64 m. Therefore, in order to compare the two methods directly, we split the data into 3 wavelength bins: 0.2–4 m (AUV only), 4–16 m (AUV and LIDAR), and 16–64 m (LIDAR only).

4.3.2 Ensemble phase averaging

Here we take an ensemble averaged view of the alongshore tidal flow, and examine its spatio-temporal structure as a function of phase and cross-shore distance. Ensemble phase averaging allows us to combine field observations from multiple AUV surveys (Table 4.1), facilitating a more robust velocity field reconstruction. Here, the alongshore pressure gradient determines the tidal phase, rather than the local depth-averaged alongshore velocity (c.f., Arzeno et al., 2018). In this case, it is convenient to examine the cross-shore structure of the alongshore flow as a function of the alongshore pressure gradient phase because, in contrast to the alongshore flow, the sea surface elevation gradients are expected to remain uniform in the cross-shore direction over the reef scale.

To extract the tidal amplitude and phase, the observed alongshore pressure gradient is filtered via complex demodulation (Emery and Thomson, 1997) using a Blackman window centered around the M_2 tidal frequency band (12.42 h) (Figure 4.4). The phase (ϕ) is defined so that the pressure gradient adheres to a cosine function (Figure 4.4, see also Figure 4.5a); the interval between pressure gradient peaks is defined linearly from 0° to 360° for each tidal oscillation. The characteristic amplitude of the pressure gradient (Λ_0) is computed as the maximum amplitude of the complex demodulated signal within each oscillation period ($T = 2\pi/\omega$). The characteristic velocity scale (V_0) is then derived based on an unsteady momentum balance as $V_0 = \Lambda_0/\omega$, and represents the maximum tidal velocity amplitude in the absence of bottom friction (see section 4.3.3 and C).

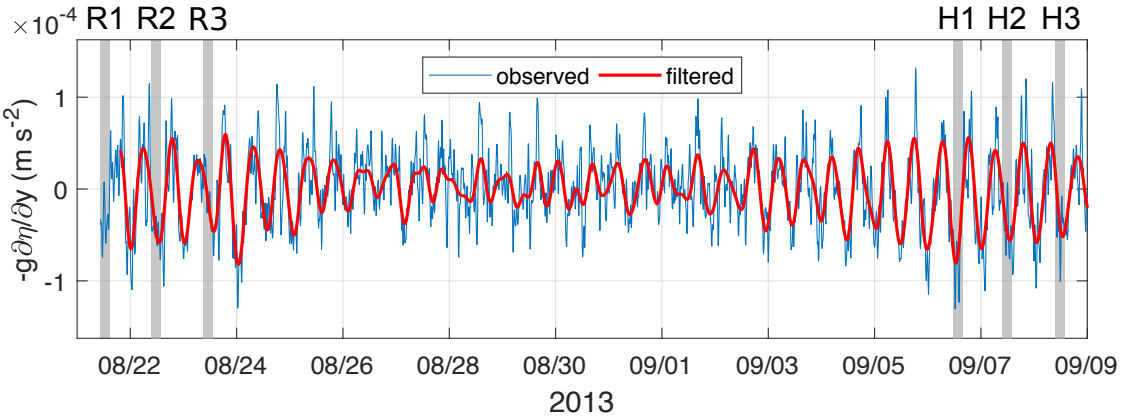

Figure 4.4: Time-series of the alongshore pressure gradient: observed (blue) and filtered via complex-demodulation (red). Shaded rectangles illustrate the AUV survey times. Benthic roughness and hydrodynamic surveys are labeled as R1, R2, R3 and H1, H2, H3, respectively.

Phase averages of the normalized pressure gradient (Figure 4.5a) and of the ADCP depth-averaged alongshore velocity ensembles (Figure 4.5b,c) exhibit phase offsets consistent with Figure 4.2, with velocities roughly in quadrature with the pressure gradient and the nearshore leading the offshore flow in phase. Phase offsets remained constant throughout the observational period. Arzeno et al. (2018) report high coherence between pressure gradient and velocity signals ($\text{Coh}^2 = 0.99$) with a periodic pattern dominated by semidiurnal forcing. The qualitative comparison between the three tidal cycles associated with the hydrodynamic surveys (solid black

lines in Figure 4.5) and the full 50 cycles observed (dashed gray lines Figure 4.5) suggests that normalized phase-averaged quantities from the H1–H3 subset are generally consistent with those for the overall dataset. Secondary intratidal variations in the pressure gradient for the H1–H3 subset (black line in Figure 4.5a) are likely related to local (i.e., affecting only one pressure sensor), stochastic sea surface height fluctuations. Accordingly, these intratidal features are likely to have short alongshore length scales (< 2 km), and are thus not expected to affect the large scale pressure gradient and the associated reef-scale alongshore flow.

Depth- and spatially-averaged AUV-based velocity measurements were normalized for each hydrodynamic survey (H1–H3) using corresponding characteristic velocity scales (V_0) as listed in Table 4.1, and then sorted according to their respective phase (ϕ) and cross-shore location (x). This collapses the AUV velocity data from multiple surveys (H1–H3) reasonably well near the 20 m and 12 m isobaths, as shown in Figure 4.5b,c (light blue circles). These AUV-based velocities also show favorable agreement with ADCP velocities at the 20 m ($r^2 = 0.93$) and 12 m ($r^2 = 0.88$) isobaths. Individual scatter in AUV-based velocity measurements (~ 2 cm s^{-1}) is likely the result of wave-induced effects and spatial variations in alongshore flow.

We reconstruct the full tidal cycle for the depth-averaged alongshore flow using a least-squares fit of a sinusoidal function

$$\hat{V}(x,\phi) = \frac{V}{V_0}\sin(\phi - \Delta\phi)\,, \tag{4.2}$$

to the normalized AUV data from the H1–H3 surveys, which cover roughly 60% of the full tidal cycle (see Table 1). This also allows us to quantify the tidal velocity phase shift ($\Delta\phi$, positive for a phase lead) and attenuation (V/V_0) at each cross-shore location (x). We extend this process to a range of cross-shore locations ($-1100 \leq x \leq -480$ m) at 1 m intervals to reconstruct the cross-shore structure of the alongshore flow, using the fit given in equation (4.2) and as shown in Figure 4.6. Results (depicted in Figure 4.6) are consistent with the sequence of cross-shore

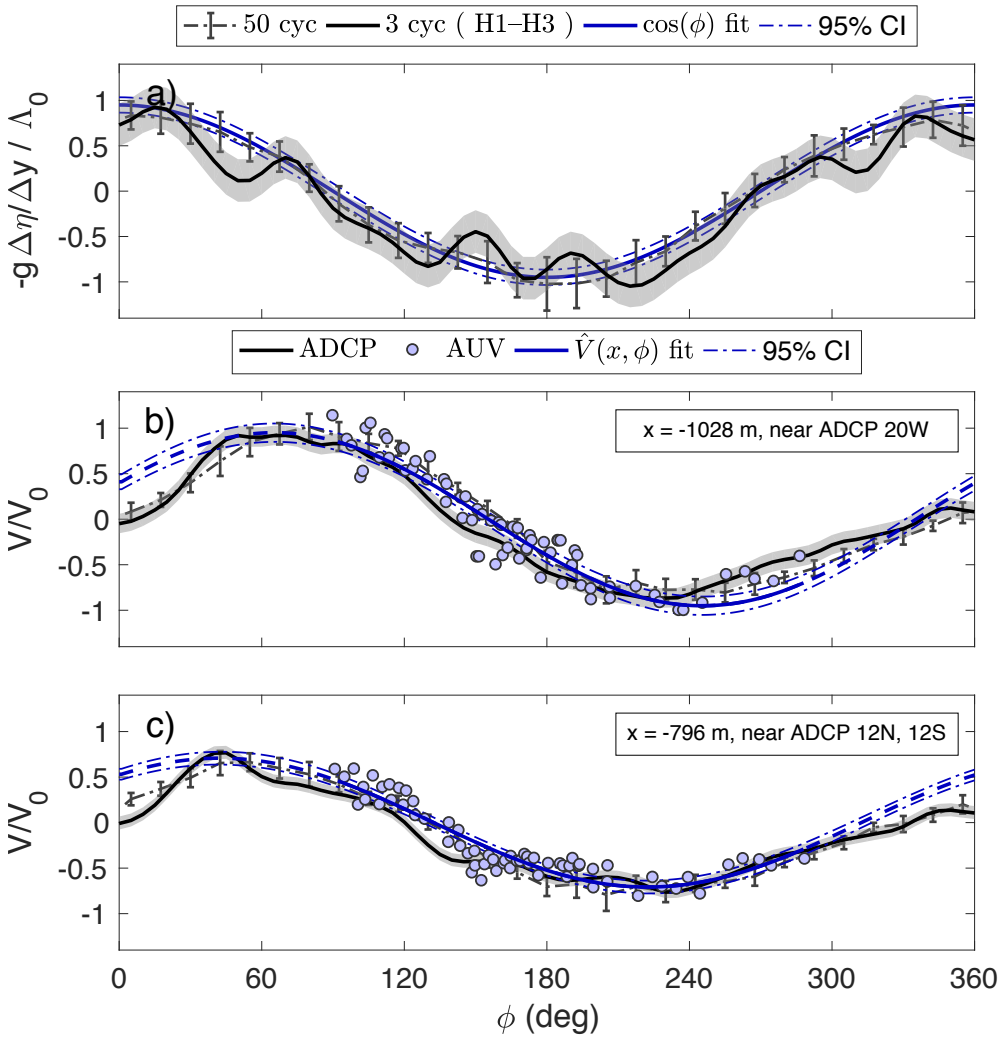

Figure 4.5: Normalized, phase-ensemble averages of (a) alongshore barotropic pressure gradient derived from SBE pressure sensors and depth-averaged alongshore velocities near the (b) 20 m and (c) 12 m isobaths. Averaged fixed observations for 50 tidal cycles (dashed gray line) and 3 AUV survey tidal cycles (solid black line) along with AUV-based observations (light blue circles) for three hydrodynamic surveys (H1–H3). Sinusoidal fits to AUV data (blue) from the H1–H3 surveys allow the reconstruction of the full tidal cycle. Pressure gradient and velocity observations were normalized for each tidal cycle by the corresponding scaling values Λ_0 and V_0. Shaded regions, error bars, and blue dash-dotted lines represent 95% confidence intervals.

transects presented in Figure 4.2; in particular, we highlight the velocity attenuation and phase lead in the nearshore region relative to the offshore flow.

AUV-derived velocity fits in Figure 4.5b,c (blue line) agree well with the ADCP velocity ensembles (black line) for most of the tidal cycle, although both fits appear to over-estimate the alongshore velocity over the initial northward flow phase, between about 300 and 40 degrees. In contrast, a visual inspection suggests that the alongshore pressure gradient signal is near sinusoidal (Figure 4.5a). The deviations on the northward flow phase suggest that other unaccounted momentum sources may be driving the offshore transport of low momentum fluid from shallower regions of the reef. We will address this issue in greater detail in section 4.5.

4.3.3 Model for tidally-driven alongshore flow

Following observations and analysis of the momentum budget for the Makua forereef (Arzeno et al., 2018), we adopt a simple one-dimensional model that assumes a balance between the local acceleration, the barotropic pressure gradient, and the bottom drag. These terms account for the bulk of the momentum balance near the 12 m isobath, effectively closing the tidally-averaged momentum budget 75% and 61% of the time at 12N and 12S, respectively (Arzeno et al., 2018). Scaling considerations suggest that the surface wind stress, the Coriolis term, and the lateral stress gradient are about one to two orders of magnitude smaller than the dominant forcing terms for the observational period. We neglect contributions due to cross-shore advection, which was shown by Arzeno et al. (2018) to play a local role near regions with highly variable bathymetry. We consider an alongshore uniform bathymetry [$h = h(x)$] (discussed in section 4.4.2) where depth-averaged alongshore flow is only a function of the cross-shore coordinate and time [$V = V(x,t)$]. Further, we assume that sea level variations are small compared to the water depth ($\eta \ll h$, $\eta/h \leq 0.03$ for the Makua forereef), and that the sea surface height (η) and the pressure gradient ($g\partial\eta/\partial y$) do not vary in the x-direction. We will revisit implications associated with these assumptions in section 4.5.

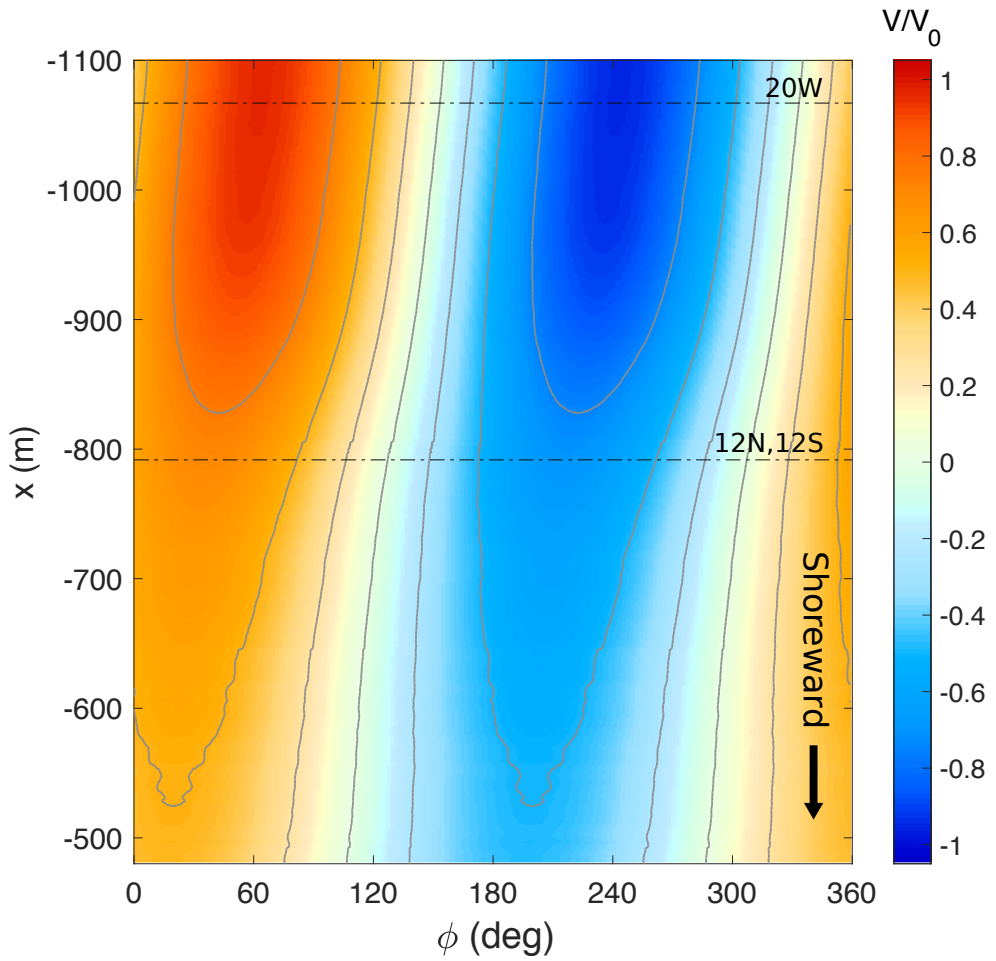

Figure 4.6: Normalized, depth-averaged alongshore velocity as a function of tidal phase (ϕ) and cross-shore distance (x) reconstructed from AUV velocity observations using (4.2). Positive (red) and negative (blue) velocity values correspond to northward and southward flows, respectively. Solid contour lines represent normalized velocity levels ranging from -0.75 to 0.75 in 0.25 intervals. Thin horizontal dashed lines represent the cross-shore location of the 12 and 20 m isobaths.

The depth-averaged alongshore momentum equation is then

$$\frac{\partial V}{\partial t} = -g\frac{\partial \eta}{\partial y} - \frac{\tau_b}{\rho h}, \tag{4.3}$$

where t is time, $g = 9.8$ m s^{-2} is gravitational acceleration, τ_b is the bottom stress, ρ is density, and h is the local water depth. The bottom stress is estimated following Feddersen et al. (2000) (see also Lentz et al., 2018)

$$\tau_b = \rho C_D \left\langle (V + \tilde{v})|\mathbf{U} + \tilde{\mathbf{u}}| \right\rangle, \tag{4.4}$$

where $\langle\cdot\rangle$ represents a time average over multiple wave cycles, C_D is a nondimensional drag coefficient for depth-averaged flow, $\mathbf{U} = U\hat{\mathbf{i}} + V\hat{\mathbf{j}}$ is the mean, depth-averaged horizontal velocity vector, and $\tilde{\mathbf{u}} = \tilde{u}\hat{\mathbf{i}} + \tilde{v}\hat{\mathbf{j}}$ is the horizontal wave velocity vector evaluated at the bottom ($z = -h$). We substitute (4.4) in (4.3), assume a sinusoidal pressure gradient [$-g\frac{\partial \eta}{\partial y} = \Lambda_0 \cos(\omega t)$], and rewrite this in nondimensional form (see Appendix C) as follows:

$$\frac{\partial V^*}{\partial t^*} = \cos(t^*) - F(x)\left\langle \left(V^* + \tilde{v}^*\right)\left|\mathbf{U}^* + \tilde{\mathbf{u}}^*\right| \right\rangle, \tag{4.5}$$

where

$$t^* = \omega t = \frac{n\pi\phi}{180^\circ}, \quad n = 0, 1, 2, 3, \ldots$$

$$V^* = \frac{V}{V_0}, \quad v^* = \frac{v}{V_0}, \quad \mathbf{U}^* = \frac{\mathbf{U}}{V_0}, \quad \tilde{\mathbf{u}}^* = \frac{\tilde{\mathbf{u}}}{V_0},$$

and

$$F(x) = \frac{\Lambda_0 C_D(x)}{\omega^2 h(x)}, \tag{4.6}$$

represents a nondimensional drag coefficient that varies with depth, drag coefficient, and tidal forcing.

Note that alongshore advection ($V\partial V/\partial y$) is neglected when writing (4.3); its order of

magnitude relative to that of the bottom drag can be shown to be

$$\frac{O\left(V\frac{\partial V}{\partial y}\right)}{O\left(\frac{\tau_b}{\rho h_0}\right)} \sim \frac{1}{C_D}\frac{h_0}{L_y}\frac{\Delta V}{V},$$

where $\Delta V/V$ represents the spatial variation in the depth-averaged alongshore velocity relative to the spatially-averaged flow, L_y denotes the averaging length scale, and h_0 is a characteristic water depth. We estimate alongshore velocity differences using rms variations in individual transect estimates (e.g., see scatter in Figure 4.5b,c) to give $\Delta V/V \sim 10^{-1}$. For our observational domain $h_0/L_y \sim 10^{-2}$. We thus conclude that when $C_D > 10^{-3}$ the advective terms will be of secondary importance. This condition, however, can be further relaxed here given that the unexplained variance may not be wholly attributable to the streamwise variations in the alongshore current. Additional contributions to the scatter in AUV ensembles (and to ΔV) can arise from errors in the estimation of V_0 and the influence of wave-induced velocities (see section 4.3.2). Arzeno et al. (2018) estimated drag coefficients at the 12 m isobath at Makua from log-fits to velocity profiles, and obtained local estimates ranging from 2×10^{-3} to 8×10^{-3}. We will revisit this topic in section 4.4.2, where we present spatially-averaged C_D estimates for a range of cross-shore locations. We further discuss the role of advection in section 4.5.

To account for the influence of surface gravity waves on bottom drag, we model the cross-shore wave transformation assuming conservation of wave energy flux with a normally incident (see θ_w in Table 4.1), alongshore uniform wave field (i.e., $\partial_y = 0$) with no wind-wave generation, breaking, or bottom drag dissipation. The resulting expression for the cross-shore wave height shoaling is

$$H_s(x) = \left[\frac{c_{gP}}{c_g(x)}\right]^{\frac{1}{2}} H_{sP}, \tag{4.7}$$

where c_g is the group velocity calculated via linear wave theory, H_s is the significant wave height, and H_{sP} and c_{gP} are computed at the SBE pressure sensors (see wave conditions in Table 4.1).

We calculate wave orbital velocities at the bottom ($z = -h$) using linear wave theory

$$\tilde{u}(x) = \frac{\omega_w H_s(x)}{2\sqrt{2}\sinh(k_w h)}, \tag{4.8}$$

where ω_w is the wave radian frequency, and consider a small wave angle parameterization based on a joint-Gaussian distributed velocity field (Feddersen et al., 2000), with the assumption that alongshore wave velocities and cross-shore currents are negligible (i.e., $\tilde{v} = U = 0$) so that

$$\left\langle (V+\tilde{v})|\mathbf{U}+\tilde{\mathbf{u}}| \right\rangle \approx \sqrt{\frac{2}{\pi}}\sigma_u V b \exp(b)\left[K_0(b)+K_1(b)\right], \tag{4.9}$$

where $b = V^2/(2\sigma_u)^2$, $\sigma_u = \tilde{u}/\sqrt{2}$ is the standard deviation of the near-bed wave orbital velocities, and K_0 and K_1 are modified Bessel functions of the second kind.

Near-bed wave orbital velocities were computed for each survey (H1–H3) following (4.7)–(4.8), assuming that wave conditions (Table 4.1) do not vary in time over each survey. We then combine the three profiles for $\tilde{u}_i(x)$ ($i = 1,2,3$; one for each survey) into a weighted-average profile $[\tilde{u}(x)]$ that accounts for the number of cross-shore transects in each AUV mission (Table 4.1). Corresponding $\sigma_u(x)$ values increase from 6 to 16 cm s^{-1} across the forereef ($-1100 \le x \le -480$ m), with wave orbital excursion amplitudes $[\sigma_u(x)/\omega_w]$ ranging from 13 to 34 cm. Modifying this analysis to include the effects of frictional dissipation (e.g., Lentz et al., 2016a) did not alter the results over the cross-section of the reef examined here.

We substitute (4.9) in (4.5) and solve the normalized, depth-averaged alongshore momentum equation for $V(t)$ for a range of values of F at each cross-shore location using a first order explicit Euler scheme (Moin, 2010). The cross-shore grid ($-1100 \le x \le -480$ m) is uniformly spaced with spatial resolution $\Delta x = 1$ m; the time step is $\Delta t = T/720$ (or $\Delta\phi = 0.5^\circ$). We integrate from an initial value $V^*(t^*{=}0, x{=}-1100){=}0$ until a stationary periodic solution is obtained, and initialize the equation at succeeding grid points ($x > -1100$ m) with the last time step value from the neighboring grid point: $V^*(0, x_j) = V^*(2n\pi, x_{j-1})$, where $x_{j-1} = x_j - \Delta x$ and n is the number

of cycles. Convergence was typically achieved within the first six cycles (rms errors $< 10^{-3}$).

4.4 Results

4.4.1 Flow structure

Figure 4.7 illustrates momentum budget terms and solutions of (4.5) using (4.9) as a function of tidal phase (ϕ) for select values of $F = C_D\Lambda_0/(\omega^2 h)$. In deep water far offshore ($h \to \infty$ as $x \to -\infty$, $F = 0$), the unsteady term balances the pressure gradient (black curves in Figure 4.7); this balance produces an alongshore velocity (Figure 4.7d) that is in quadrature with the pressure gradient (Figure 4.7a). As F increases (i.e., depth decreases), the bottom drag (Figure 4.7c) becomes progressively more important in the momentum balance (note the corresponding decrease in the amplitude of the unsteady term in Figure 4.7b). Frictional effects attenuate flow velocities and drive a more immediate response to the pressure forcing, decreasing the phase lag between the velocity and the pressure gradient; this is manifested as a reduction in the velocity amplitude (V/V_0) and a corresponding phase shift ($\Delta\phi$) in the nearshore velocity relative to the offshore flow, as shown in Figure 4.7d (colored curves). When $F \gtrsim 2.9$, bottom stress balances pressure gradient over most of the tidal cycle. This dominant balance between the pressure gradient forcing ($\cos t^*$) and the drag term ($F\langle V^*|\tilde{u}^*|\rangle$) produces velocity curves that gradually approach the square root of a sinusoid with increasing F values (e.g., note the flattening of crests in Figure 4.7d).

At each cross-shore location, an optimal value for F is determined by fitting with the AUV-based velocity observations (Figure 4.6) in a least-squares sense. In this case, C_D is effectively the only fitting parameter given that the values for Λ_0, h, ω are known from observations (further discussion to follow in section 4.4.2). Best-fit solutions of (4.5) using (4.9) accurately reproduce the cross-shore structure and evolution of the observed depth-averaged alongshore flow (Figure 4.6). Figure 4.8 shows the best-fit cross-shore structure over the full tidal phase with

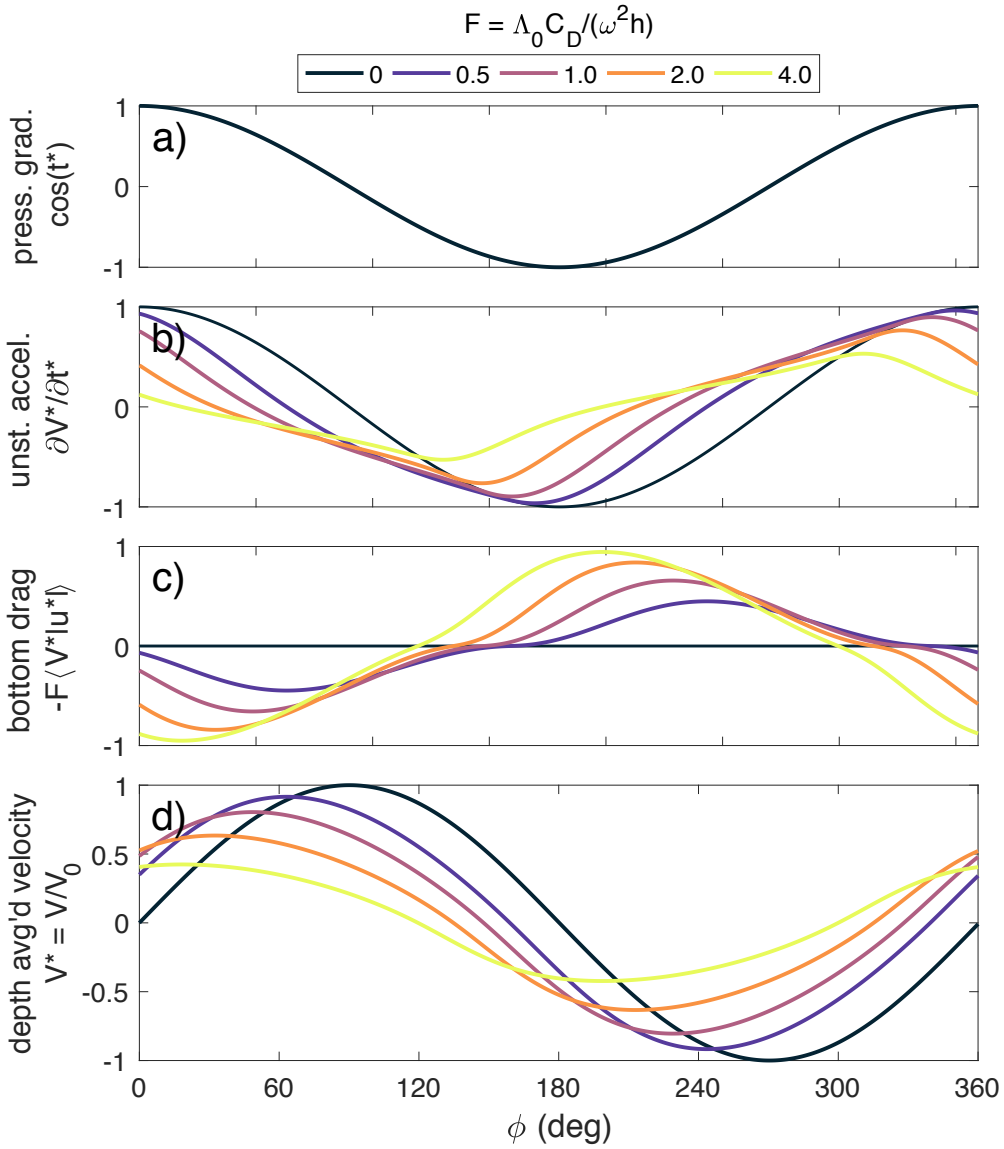

Figure 4.7: Normalized (a) pressure gradient, (b) unsteady acceleration, (c) bottom stress, and (d) depth-averaged velocity as a function of tidal phase (ϕ): solutions to equation (4.5) using (4.9) for select values of nondimensional drag $F = 0$, 0.5, 1.0, 2.0, 4.0. These values for F correspond to $h = \infty$, 22.6, 16.7, 11.4, 6.2 m ($x = -\infty$, -1100, -902, -782, -510 m) for the observed data.

contours of the AUV observations overlaid.

The principal characteristics of the flow structure, the velocity phase shift ($\Delta\phi$) and amplitude attenuation (V/V_0) relative to the offshore flow, are highlighted in Figure 4.9b,c. Cross-shore variations in $\Delta\phi$ and V/V_0 estimated from best-fit solutions (blue lines in Figure 4.9b,c) using (4.2) are consistent with both ADCP- (black circles in Figure 4.9b,c) and AUV-based (black lines in Figure 4.9b,c) measurements. Although best-fit estimates slightly under-predict amplitudes and phase shifts, comparisons indicate good quantitative agreement overall, with linear regression slopes of 0.86 and 0.97 for $\Delta\phi$ and V/V_0, respectively, and high skill ($r^2 = 0.99$) for both quantities. Differences between the AUV-observed and modeled velocity phase shifts ($\Delta\phi$) increase from 1 to around 9 degrees in the shoreward direction. Discrepancies between the observed and modeled velocity amplitudes (V/V_0) peak near $x = -960$ m with a maximum difference of about 7%, subsiding to a relatively constant level of about 4% for $x > -800$ m. Taken together, results in Figure 4.8 and Figure 4.9b,c confirm that equation (4.3) describes the alongshore dynamics adequately on tidal timescales, over a significant portion of the Makua forereef.

For fully developed flow, the momentum budget is dominated by pressure and drag forces. This balance gives rise to a characteristic length scale, h_δ (see equation C.7), that provides a measure of the depth at which the flow can become fully developed across the water column for a given tidal oscillation. This quantity can also be interpreted as a measure of the height of the bottom boundary layer (dashed blue line in Figure 4.9a) at maximum velocity and bottom stress.

Cross-shore profiles of the non-dimensional momentum budget terms (scaled by Λ_0) show the bottom drag ($|F\langle V^*|\tilde{u}^*|\rangle|$) overtaking the unsteady acceleration term ($|\partial V^*/\partial t^*|$) around the 15 m isobath (Figure 4.9d). The alongshore velocity profile develops an inflection point around this region, leading to a maximum cross-shore shear $|\Delta V/\Delta x| \approx 8 \times 10^{-4}$ s^{-1} at the onset of flow reversal (i.e., near pressure gradient zero-crossings: $\phi = 90°, 270°$). The pressure gradient is predominantly balanced by the bottom drag at shallower depths ($h < h_\delta \approx 8$ m, see

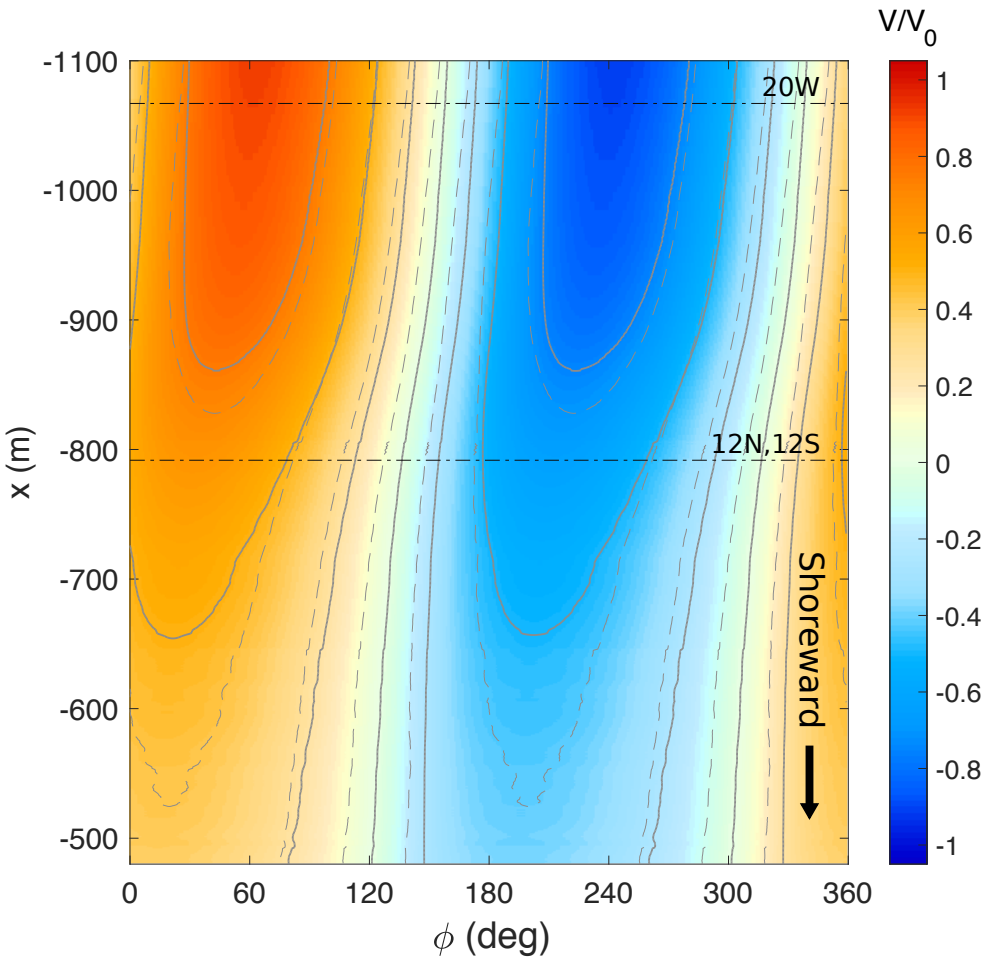

Figure 4.8: As in Figure 4.6, but for best-fit solutions of the alongshore momentum balance using (4.5) and (4.9). Dashed contour lines, overlaid here for reference, show AUV velocity observations from Figure 4.6.

(C.7) in C). Here, the bottom boundary layer extends over the full depth of the water column at maximum velocity and bottom stress (see dashed blue line in Figure 4.9a), and does not experience significant cross-shore shear over the tidal cycle. Wave-driven enhancement of bottom friction begins to play a more important role in the bottom drag as waves shoal ($h < 13$ m), contributing to an increase of up to 18% in drag in the shallower regions of our sampling domain ($h \approx 6$ m).

4.4.2 Drag coefficient

The bottom stress formulation in (4.6) assumes a drag coefficient (C_D) that relates the drag term (τ_b) in (4.4) to the depth-averaged value $\left\langle (V+\tilde{v})|\mathbf{U}+\tilde{\mathbf{u}}| \right\rangle$, as parameterized in (4.9). The best-fit solutions of the alongshore momentum balance (Figure 4.8) and the associated $F(x)$ values allow the straightforward estimation of a spatially-averaged C_D from (4.6), provided that Λ_0, ω, and $h(x)$ are known. We thus compute a characteristic pressure gradient scale (Λ_0) and tidal frequency (ω) for the H1–H3 sampling period, weight-averaging to account for the number of cross-shore transects in each AUV mission (Table 4.1). The cross-shore depth profile, $h(x)$, (Figure 4.9a) was estimated by spatially-averaging the LIDAR-derived bathymetry over the alongshore extent of the study region ($-300 < y < 1500$ m).

Drag coefficient (C_D) estimates derived from theoretical best-fit solutions using (4.6) (solid blue line in Figure 4.9e) range from 0.004 to about 0.010 [$\pm$0.002] over a 600 m cross-section of the forereef, for water depths spanning from 24 to 5 m; and show a general increase with decreasing water depth. Error bands in Figure 4.9e represent the 95% confidence intervals quantified in terms of Λ_0, ω^2, $h(x)$, and $F(x)$ by adding their respective uncertainties in quadrature (Emery and Thomson, 1997). Uncertainties in Λ_0 and ω^2 were derived from standard errors in pressure gradient fits, and account for about 5% of the error in C_D. Uncertainties associated with $h(x)$ include both the semi-diurnal variations in sea surface height (η) and the alongshore variations in LIDAR-derived bathymetry (computed as the 95% confidence level via bootstrapping), and

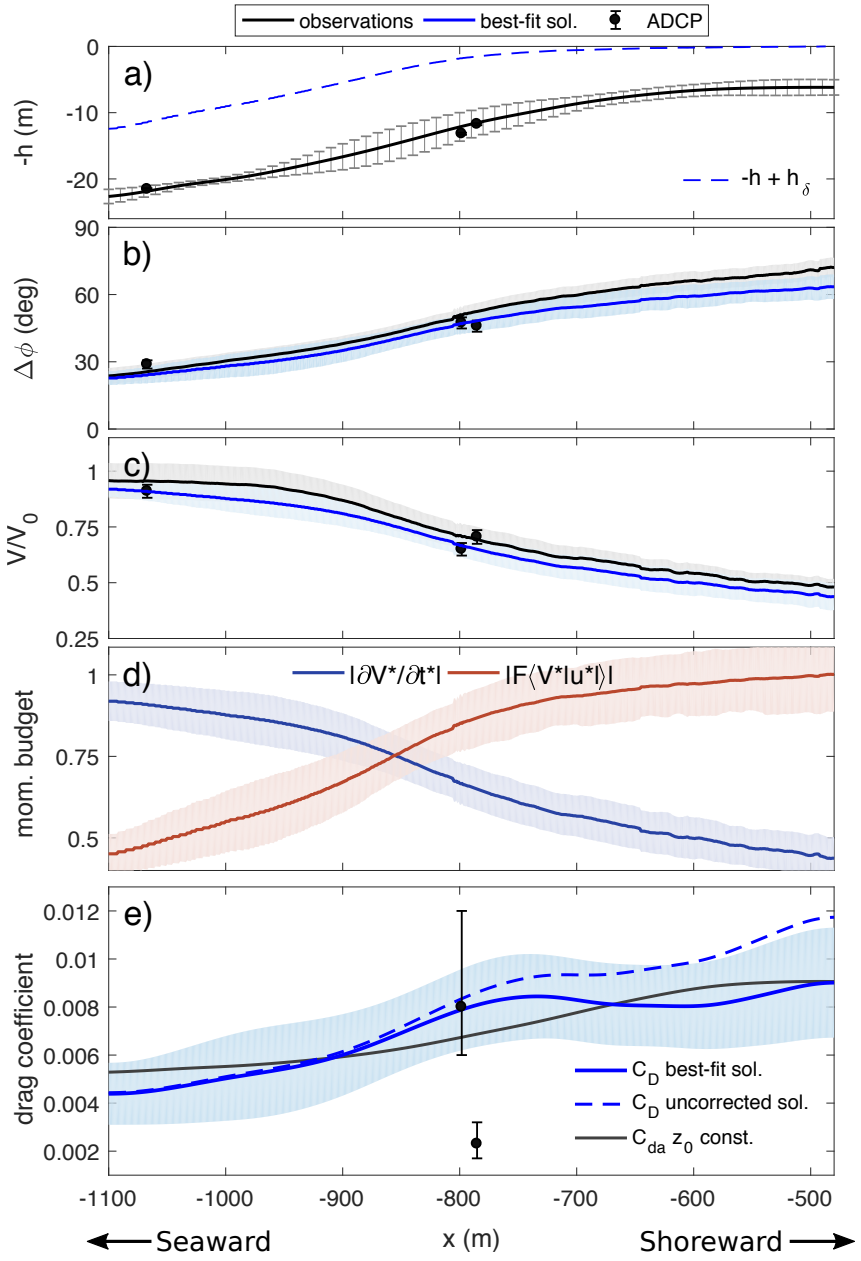

Figure 4.9: Cross-shore profiles of (a) water depth from LIDAR data, (b) tidal velocity phase shift and (c) attenuation relative to the offshore flow, (d) amplitudes of the nondimensional (blue) unsteady acceleration ($|\partial V^*/\partial t^*|$) and the (red) bottom stress ($|F\langle V^*|\tilde{u}^*|\rangle|$) terms, and (e) drag coefficient (C_D) estimates. The dashed blue line in (a) represents the location of h_δ relative to water depth, $-h$ (see C.7). Black circles in (a)–(c), and (e) represent fixed ADCP-based values; black and blue lines in (b) and (c) correspond to AUV-based observations and values obtained from best-fit solutions of the alongshore momentum equation, respectively. Solid blue in (e) represents the best fit solution for C_D, while the dashed line represents the fit neglecting wave effects on steady bottom drag; the solid black line in (e) was obtained using (4.10) assuming a constant z_0. Error bars and shaded regions indicate the standard deviation in (a) and the 95% confidence intervals in (b)–(e).

represent 7% of the error in C_D on average. Uncertainties in optimized $F(x)$ values were derived from the standard errors of the best-fit solutions, and explain the remaining 88% of the error. Surface gravity waves enhance bottom stress on the mean flow across the reef; excluding the influence of waves leads to overestimating drag coefficients by 5%–30% in water depths ranging from 12.7 m to 6.2 m (dashed blue line in Figure 4.9e).

Comparisons with local drag coefficient estimates derived by Arzeno et al. (2018) from ADCP-based log-fits (black circles in Figure 4.9e) show good quantitative agreement with best-fit solution estimates of C_D at 12N ($x \approx -798$ m), but deviate considerably (by about a factor of four) at 12S ($x \approx -785$ m). Similar discrepancies have been observed in previous studies for log-fit and momentum balance comparisons of drag coefficient estimates in coral reef environments; most notably due to the influence of nearby obstacles on the shape of the observed velocity profiles (e.g., Rosman and Hench, 2011; Rogers et al., 2018) or because definition of the bottom is ambiguous (e.g., Lentz et al., 2016b). Arzeno et al. (2018) noted non-negligible advective contributions at 12S, suggesting that a large (~ 3 m) bathymetric step located approximately 25 m south of the mooring site could have resulted in a local acceleration of the flow. These advective contributions may also account for the poorer agreement shown in Figure 4.9e for 12S.

For depth-averaged currents, Lentz et al. (2017) define the following drag coefficient formulation:

$$C_{da} \approx \kappa^2 \left[\log\left(\frac{h}{z_0}\right) + (\Pi - 1) \right]^{-2}, \tag{4.10}$$

where $\kappa = 0.4$ is the von Kármán constant, z_0 is the hydrodynamic roughness scale, and $\Pi \approx 0.2$ is Cole's wake strength parameter for high Reynolds number in open channel flow (Coles, 1956; Nezu and Nakagawa, 1993). The applicability of (4.10) for depth-averaged flow relies on several assumptions: small roughness elements relative to the depth water column ($z_0 \ll h$); and

unidirectional, fully developed, turbulent flow with a velocity profile described by

$$v(\tilde{z}) = \frac{u_*}{\kappa}\left[\log\left(\frac{\tilde{z}}{z_0}\right) + 2\Pi\sin^2\left(\frac{\pi\tilde{z}}{2h}\right)\right], \tag{4.11}$$

where $u_* = \sqrt{\tau_b/\rho}$ is the friction velocity and $\tilde{z}$ is the height above z_0. These assumptions imply a steady state balance between the pressure gradient and the bottom stress, and a fully developed boundary layer over the depth of the water column.

We proceed with the assumptions outlined above, and obtain a cross-shore profile of the implied hydrodynamic roughness (z_0) by inverting (4.10) using the alongshore averaged values for the drag coefficient (C_D). The implied z_0 values range from about 2 to 6 cm [$\pm$1 cm] across the reef, with a conspicuous amplification between $-850 < x < -650$ m (Figure 4.10a). We will further examine the cross-shore profile of z_0 as well as the relationship between physical roughness and hydrodynamic roughness in section 4.4.3.

We can illustrate the relative role of depth in the drag variation using (4.10) to estimate C_{da} using a constant value for z_0. Using the mean value for the implied hydrodynamic roughness shown in Figure 4.10a ($\bar{z}_0 \approx 4.2$ cm), $C_{da}\big|_{\bar{z}_0}$ decreases monotonically with decreasing depth (solid black line in Figure 4.9e), as expected. Relative variations in the measured C_D then highlight the influence of variable roughness. Results in Figure 4.9e show that the dependence of C_D with water depth is generally consistent with $C_{da}\big|_{\bar{z}_0}$. However, C_D exhibits a local maximum around $x \approx -750$ m ($h \approx 10.2$ m) that is not observed in $C_{da}\big|_{\bar{z}_0}$, suggesting that cross-shore variations in hydrodynamic roughness (z_0) are likely playing an important role in regulating the alongshore averaged drag coefficient (C_D) at the Makua forereef. The local maximum in C_D coincides roughly with the cross-shore location of large-scale bathymetric features associated with spur and groove morphology (see Figure 4.3).

It should be noted that a reasonable parameterization of the drag coefficient based on the quadratic drag law ($C_D = C_{da} = u_*^2/U_{\mathrm{ref}}^2$) requires a self-similar velocity profile with a shape that

is independent of flow speed and a meaningful reference velocity (U_{ref}) (depth-averaged or at a fixed height). Here, we have selected the depth averaged alongshore flow as the reference velocity for practical reasons. However, our observations and analysis indicate that the alongshore flow is not always fully developed across the water column. For cases in which the flow is not fully developed, the "free stream" flow that does not feel the effects of the boundary is expected to occupy some fraction of the water column. This, in turn, leads to larger depth-averaged velocity magnitudes relative to the fully developed case because the free stream flow is generally faster than the flow within the boundary layer. We therefore expect that both C_D and $C_{da}\big|_{\bar{z}_0}$ (Figure 4.9e) will be slightly underestimated for regions where the flow is not fully developed.

4.4.3 Roughness

LIDAR and AUV-based roughness data were analyzed as described in section 4.3.1 to qualitatively assess the scales that are most relevant to the hydrodynamic roughness. Rms roughness heights were calculated using (4.1) in the cross- and alongshore directions for the spectral bands between 16–64 m, 4–16 m, and 0.2–4 m (Figure 4.10b,c). Differences between the cross- and alongshore rms roughness estimates point to directionality in the seabed substrate. These differences are most evident for the larger wavelengths (4–64 m), particularly between $-850 < x < -650$ m (Figure 4.10b). In contrast, directional differences are less pronounced for the 0.2–4 m spectral band (Figure 4.10c), suggesting that reef roughness is more isotropic at smaller scales. Overall, rms roughness estimates decrease substantially offshore ($x < -900$ m), and become increasingly more isotropic towards the reef flat. The aforementioned patterns are consistent with the roughness variability evident in Figure 4.3.

The AUV-based rms roughness estimates compare favorably with LIDAR estimates for the 4–16 m band in the alongshore direction (Figure 4.10c), but slightly deviate in the cross-shore direction, especially closer to shore. Some of the observed deviations could be attributed to the effects of wave motion on the vehicle (Amador et al., 2017), which can modify its trajectory

and in turn increase the observed rms roughness. In this case, wave-induced motions would be accentuated for cross-shore transects and in shallower regions closer to shore, where wave orbital velocities tend to be more significant due to shoaling.

The cross-shore profiles for rms in Figure 4.10b,c also provide a good representation of relative bottom slope rms variation for the selected spectral bands, since the slope spectrum is related to the roughness spectrum by a factor of $1/\lambda$, where λ is the roughness wavelength in each spectral band. Here we are considering selected spectral bands, with fixed representative wavelengths so that the corresponding slope rms will vary similarly.

The spectral rms roughness estimates (Figure 4.10b,c) collected over the reef shelf reflect three regions with distinct roughness characteristics that are also evident in the alongshore gradient illustrated in Figure 4.3. First, a smooth region offshore ($x < -900$ m) corresponding to a sandy seabed, exhibiting low roughness values in all bands. Second, a rough reef region ($-850 < x < -650$ m), coinciding with the location of spur and groove formations (see Figure 4.3). Third, a region closer to shore marked by reduced rms at low wave numbers.

The most significant observation to emerge from a comparison between the rms data in Figure 4.10 and the inferred z_0, is that the main peak in hydrodynamic roughness, located between $-850 < x < -650$ m (Figure 4.10a), is only represented in the larger spectral wavelengths bands (4–64 m). As mentioned previously, this region of elevated roughness coincides with the cross-shore location of large-scale features associated with spur and grove morphology (see Figure 4.3). Further, correlations of z_0 versus LIDAR-derived rms over a range of spectral wavelengths (4–64 m) (not shown), indicate that z_0 is better correlated ($0.6 < r^2 < 0.75$) with the longer wavelengths ($\lambda > 14$ m). Interestingly, correlations with the cross-shore roughness estimates were not found to be notably different from those associated with the alongshore roughness.

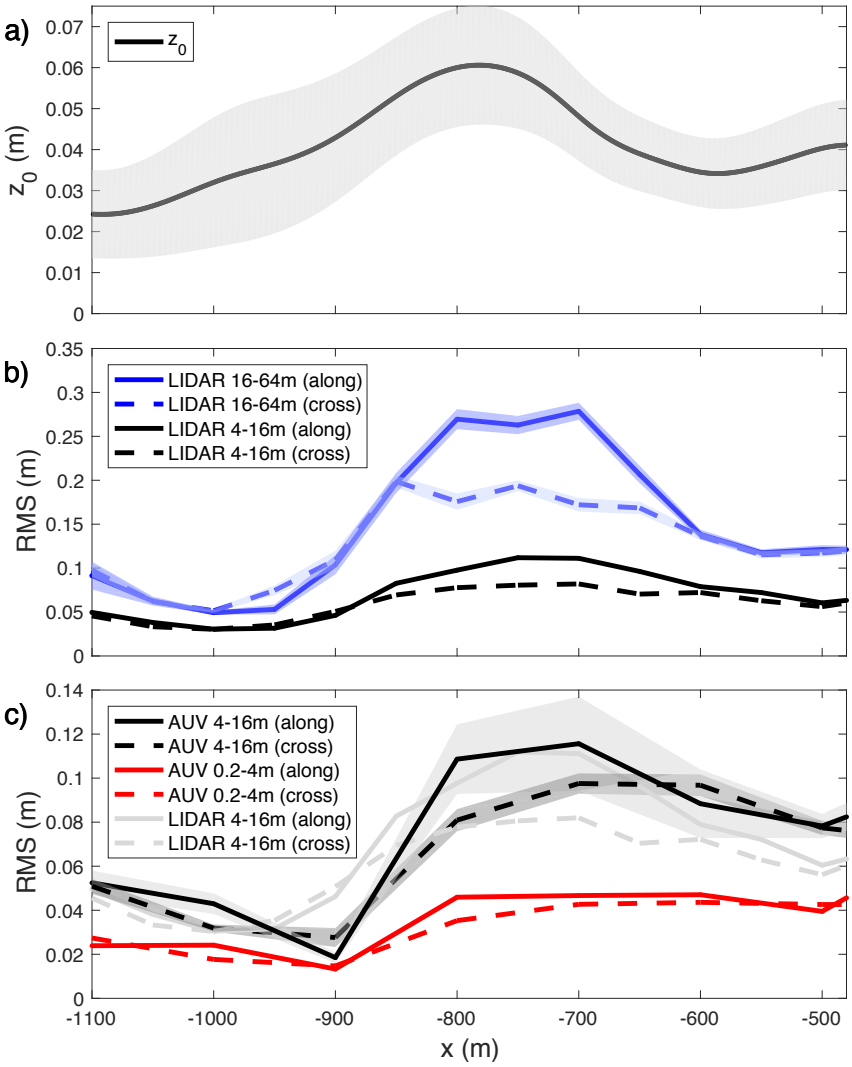

Figure 4.10: Cross-shore profiles of (a) hydrodynamic roughness, z_0, inferred from best-fit solutions using (4.6) and (4.10), and spectral rms bottom roughness calculated using (4.1) from (b) LIDAR- and (c) AUV-derived spectral variance for the cross-shore (dashed lines) and alongshore (solid lines) directions. Blue, black and red lines in (b)–(c) capture the spectral rms roughness for wavelengths between 16–64 m, 4–16 m and 0.2–4 m, respectively; faint gray lines in (c) correspond to LIDAR-derived rms roughness for the 16–64 m band (shown again for comparison). Shaded regions in (a)–(c) indicate 95% confidence intervals.

4.5 Discussion

The analytical predictions shown in Figure 4.8 (see also Figure 4.9b,c) provide an accurate representation of the depth-averaged alongshore flow at the Makua reef on tidal timescales, indicating that the alongshore momentum budget is appropriately described on semidiurnal timescales by a balance between local acceleration, barotropic pressure gradient, and bottom drag. These results are consistent with the local primary balance obtained by Arzeno et al. (2018) for the 12 m isobath using time series data from point sensors. A broader reef-scale scale view, however, suggests that cross-shore variations in water depth and bottom roughness substantially modulate the relative magnitudes of the unsteady and bottom drag terms across the reef (Figure 4.9d). These cross-shore variations in the along-shore momentum balance drive an oscillatory boundary layer response, with the nearshore flow leading the offshore flow in phase and with a corresponding attenuation of the velocity magnitude. In general, these relatively simple dynamics should hold for any tidally-dominated environment with slowly varying along-flow geometry and variable depth in the cross-flow direction.

The results of this study highlight the role of bathymetry in establishing the relative dominance of the momentum budget terms, and in turn, the nature of the tidally-driven alongshore flow over the reef. The alongshore momentum balance provides a natural depth scale, h_δ (see Appendix C), that divides alongshore flow into two distinct regions. For $h < h_\delta$, the flow is characterized by a predominant pressure gradient–bottom drag balance. This implies that the bottom generated turbulence has enough time to equilibrate and spread vertically over the water column before flow reversal. For $h > h_\delta$, the momentum budget exhibits contributions from the local acceleration, pressure gradient, and bottom drag. In this case, the balance produces a "free-stream" inertial core above the boundary layer that does not feel the effects of bottom generated turbulence. The dynamics of tidally-driven alongshore flows are in contrast to the more typical steady pressure gradient–bottom drag balance of shallow reef flats (e.g., Hench et al.,

2008; Lentz et al., 2016b; Rogers et al., 2018), where the unsteady term is usually neglected because the flow is assumed to become fully-developed over timescales that are shorter than the forcing timescale.

Spatially averaged drag coefficient estimates are consistent with previously reported values for tropical coral reefs in similar water depths (e.g., Reidenbach et al., 2006; Rogers et al., 2015), and compare favorably with local estimates by Arzeno et al. (2018) at the Makua 12N mooring, where advective contributions are negligible. Consistent with observations and analysis by Lentz et al. (2017), C_D estimates showed a general tendency of increasing with decreasing water depths. However, the analytical formulation in (4.6) as well as the open channel flow formulation (4.10) likely underpredict the drag coefficient when the flow is not fully-developed, as discussed in section 4.4.2. It follows that drag coefficient estimates presented in Figure 4.9e are not necessarily representative across the tidal cycle, as the relative dominance of the alongshore momentum budget terms fluctuates considerably (Figure 4.7).

The results in Figures 4.9e and 4.10 offer compelling evidence to support the idea that the larger roughness scales, with wavelengths of $O(10\text{ m})$, play a more dominant role than the small-scale roughness elements of $O(1\text{ m})$ in regulating the spatially-averaged drag coefficient (C_D) and the resulting reef-scale circulation. This is consistent with the findings of Reidenbach et al. (2006), who noted that the larger scales in reef topography may be more influential than the local roughness features in setting the drag coefficient. Rogers et al. (2015) also suggested that the form drag resulting from spur and groove morphology dominates over the drag induced by the local roughness variability. Recent model results by Rogers et al. (2018) indicate that the small scale roughness characteristics of the reef do not contribute significantly to the overall drag because the large scale features tend to create wakes that isolate the small scale elements from the main flow field. For wavy environments, near-bed wave motions may also act as a low-pass filter on the bed roughness. In this case, the roughness scales at sizes smaller than the wave orbital amplitude may not directly affect the steady flow above the wave boundary layer.

The present findings have important implications for hydrodynamic models, where the appropriate choice of length scales to characterize C_D and z_0 in complex broad-banded roughness is unclear. It is likely that large-scale roughness features, such as spur and groove formations, exert form drag onto the spatially-averaged flow, similar to the way that large-scale obstacles influence the flow response above the coral canopy layer in shallow reef systems (e.g., Lowe et al., 2005; Hench and Rosman, 2013). However, a broad spectral roughness distribution can have important consequences in terms of the hydrodynamic response. For instance, a spectral description of a sharp edge geometry clearly requires contributions from high-wavenumber components. While these high-wavenumber components may not contribute significantly to the total drag on their own, sufficiently high wavenumbers are likely necessary to characterize the large scale bluff body features that are responsible for flow separation and boundary drag in complex reef morphologies. Suitable parameterizations of bottom drag should therefore consider contributions from a sufficiently broad range of length scales.

Furthermore, as illustrated in Figure 4.10, z_0 is not uniquely determined by the spectral rms roughness. While the spectral variance provides a simple tool for describing general scales and patterns in roughness, the validity of using spectral energy alone for characterizing multi-scale roughness is questionable, most notably because it fails to capture phase information (Jaramillo and Pawlak, 2011). Thus, power spectra cannot account for the sheltering of small-scale roughness elements by large-scale roughness features (Jiménez, 2004; Yang and Meneveau, 2017). To address this limitation, Rogers et al. (2018) recently proposed a simplified approach to estimate z_0 in coral reefs that considers both the rms of the depth and of the streamwise slope, requiring the specification of a proportionality constant. Numerous other metrics can be defined to describe reef topography (e.g., Hearn, 2011; Duvall et al., 2019), but still lack correspondence to measured hydrodynamic roughness. The connection between physical and hydrodynamic roughness in highly complex bed geometries remains a topic of active research and warrants further investigation. Determining the horizontal and vertical length scales that are relevant to the

bottom drag constitutes an important step towards establishing a useful characterization of the physical roughness over coral reefs.

As evident in Figure 4.5b,c (blue line), velocity fits agree well with ADCP-based velocity ensembles (black line) over most of the tidal cycle, but exhibit deviations over the initial northward phase of the flow, despite a near sinusoidal pressure gradient. This departure from purely sinusoidal behavior suggests other sources of momentum that may be driving a net transport of low momentum fluid from the shallower regions of the reef. Previous observations at Makua by Sevadjian et al. (2012) indicate that relatively weak tidal cross-shore velocities consistently steer away from shore as the alongshore flow accelerates northward, consistent with the observed deviations. There are several possible explanations for this behavior. Cross-shore flows may be a result of asymmetries in the tidal current due to coastline curvature. Alternatively, it may be the case that alongshore variations in bottom drag due to spatial heterogeneities in roughness could be generating secondary currents (Nezu and Nakagawa, 1993; Rogers et al., 2015). These secondary currents could be manifested as offshore mean flows at ADCP locations. Also consistent with the observed deviations, the work of Rogers et al. (2015) showed that wave-induced circulation cells are capable of driving cross-shore flows over spur and groove formations for directly incident waves and low alongshore flow conditions.

While the effects of alongshore advection can be expected to diminish with spatial averaging (see section 4.3.3), it should be noted that local contributions from cross-shore advection may provide a residual lateral stress that is not accounted for by the proposed model (4.3). These residual stresses can arise from spatially-filtering the unresolved scales of motion that are smaller than the alongshore averaging length. Prior work has shown that cross-shore advective acceleration can provide a non-negligible contribution to the local momentum budget for reef morphologies with highly variable bathymetry (Rogers et al., 2015; Arzeno et al., 2018). Other potential sources of cross-shore momentum transport include thermally-driven (Molina et al., 2014) and wind-driven (Hendrickson and MacMahan, 2009) exchange flows. For the observational period considered

here, however, the estimated cross-shore wind stress was two orders of magnitude smaller than the dominant terms (Arzeno et al., 2018), and the presence of energetic alongshore flows suggests that thermally-driven flows were likely suppressed over most of the tidal cycle via bottom generated turbulence (Ulloa et al., 2018). Nevertheless, exchange circulation may be an important mechanism for driving cross-shore momentum at other sites or under different conditions, and should be taken into consideration when conducting these kinds of spatial averages. Although we anticipate that residual lateral stresses will lead to the overestimation of C_D, scaling analysis suggests that their overall magnitude was likely negligible in this case.

Despite sharing some common features with other turbulent oscillatory boundary layers (e.g., Jensen et al., 1989; Mellor, 2002), analysis of the along-shore momentum equation indicates that the dynamics at Makua are fundamentally different. Scaling considerations suggest that lateral shear stresses do not play a significant role in setting the cross-shore structure of the tidally-driven flow alongshore flow. This is because the length scales associated with the lateral exchange of momentum are usually much larger than those associated with the bottom turbulence (i.e., the local water depth). Prior work by Wolanski et al. (1984) and Signell and Geyer (1991) has also concluded that bottom friction is typically of far greater importance than the lateral stress gradient in shallow coastal waters. Lateral stresses, however, could play an important role in the momentum balance in the presence of shear instabilities (e.g., Bowen and Holman, 1989; Oltman-Shay et al., 1989), where the momentum exchange might be dominated by horizontal coherent structures (Shiono and Knight, 1991; Van Prooijen et al., 2005).

Finally, we note that these results represent reef-scale $O(1000\ \mathrm{m})$ averages, derived primarily from spatially-averaged observations and likely do not represent the local bed shear stress, which is often used to model sediment transport and nutrient uptake relationships. However, the relatively high C_D values observed over spur and groove formations imply enhanced potential for turbulent mixing, which in turn might increase the replenishment of planktonic food to the benthic community and possibly increase food uptake and coral growth rates (Reidenbach et al.,

2006). Further work is needed to elucidate how the spatial heterogeneity of coral-scale roughness features interacts with the alongshore flow.

4.6 Summary

In this paper we have examined the dominant forcing mechanisms in the alongshore momentum balance, and the resulting hydrodynamic response over the Makua reef shelf on intratidal timescales. As noted by Arzeno et al. (2018), the observations at Makua suggest that the tidal pressure gradient develops as a barotropic response to a baroclinic semidiurnal tide propagating in stratified waters offshore. Ensemble phase averages of the alongshore pressure gradient and velocities from multiple AUV surveys reveal characteristics akin to an oscillatory boundary layer, with the nearshore flow leading the offshore flow in phase and with a corresponding attenuation of the velocity magnitude near the shallower regions of the reef. Analysis of the depth-averaged alongshore momentum equation indicates that the cross-shore structure and evolution of the alongshore flow at Makua is tidally-driven and adequately described on semidiurnal timescales by a balance between local acceleration, barotropic pressure gradient, and bottom drag; a result that was previously established for the 12 m isobath with time series data (Arzeno et al., 2018).

The results of this study indicate that the velocity phase lag and attenuation, relative to the offshore flow, are uniquely determined by the local water depth (h), drag coefficient (C_D), and tidal forcing. In addition, a characteristic length scale (h_δ) associated with the height of the fully developed turbulent boundary layer can be derived directly from the momentum balance. By fitting solutions of the alongshore momentum equation with AUV-based observations, we obtain estimates of drag coefficient (C_D) and hydrodynamic roughness (z_0) over a 600 m cross-shore section of the Makua reef. These estimates compare favorably with analysis of time series data at the 12 m isobath, and show good qualitative agreement with LIDAR and AUV-based roughness

data. Results suggest that larger scales, with wavelengths of $O(10\ \mathrm{m})$, play a more significant role than smaller meter-scale roughness in determining drag.

4.7 Acknowledgments

This work was funded by the Office of Naval Research via award N00014-13-1-0340, by the Chancellor's Research Excellence Scholarship (formerly FISP), and by the Army Corps of Engineers via a subcontract from the University of California, San Diego (PO 1036151). The authors thank Audric Collignon, Carly Quisenberry, Chris Kontoes, Joe Gilmore, and Christina Comfort for their assistance with field operations in support of the Makua experiments. We also thank Antonio Sánchez and Falk Feddersen for their valuable comments and insight.

Chapter 4 is currently being prepared for submission for publication (Amador A., Arzeno I. B., Giddings S. N., Merrifield M., and Pawlak G., 2020). The dissertation author was the primary investigator and author of this paper.

Appendix A

Wave-induced Bias

A theoretical model is developed to describe the wave-induced bias observed in AUV-based velocity measurements. Here we assume that the vehicle follows very closely the horizontal and vertical water displacements produced by surface gravity waves.

AUV trajectory

Consider deep water surface gravity waves as given by linear wave theory

$$u_w = a\sigma e^{kz}\cos(kx-\sigma t)\,, \tag{A.1}$$

$$w_w = a\sigma e^{kz}\sin(kx-\sigma t)\,, \tag{A.2}$$

in Cartesian coordinates with x horizontal and z vertical. Here u_w and w_w specify the horizontal and vertical wave velocities, respectively, a is the wave amplitude, σ is the wave radian frequency, and k is the wavenumber. The trajectory of a particle immersed in a monochromatic wave field

can be obtained by solving the following set of ordinary differential equations

$$\frac{\mathrm{d}x}{\mathrm{d}t} = U + a\sigma \mathrm{e}^{kz}\cos(kx-\sigma t)\,, \tag{A.3}$$

$$\frac{\mathrm{d}z}{\mathrm{d}t} = a\sigma \mathrm{e}^{kz}\sin(kx-\sigma t)\,, \tag{A.4}$$

with initial conditions $x(0) = X_0$ and $z(0) = Z_0$. We define the non-dimensional variables

$$\hat{x} = kx\,, \quad \hat{z} = kz\,, \quad \hat{t} = \sigma t\,, \tag{A.5}$$

and the non-dimensional problem is then

$$\frac{\mathrm{d}\hat{x}}{\mathrm{d}\hat{t}} = \frac{U}{c} + \varepsilon \mathrm{e}^{\hat{z}}\cos(\hat{x}-\hat{t})\,, \tag{A.6}$$

$$\frac{\mathrm{d}\hat{z}}{\mathrm{d}\hat{t}} = \varepsilon \mathrm{e}^{\hat{z}}\sin(\hat{x}-\hat{t})\,, \tag{A.7}$$

where $c = \sigma/k$ is the wave phase speed and the small parameter $\varepsilon = ak \ll 1$ is the wave steepness.

We analyze this problem using a regular perturbation series expansion

$$\hat{x} = \hat{x}_0 + \varepsilon\hat{x}_1 + \varepsilon^2\hat{x}_2 + ... \tag{A.8}$$

$$\hat{z} = \hat{z}_0 + \varepsilon\hat{z}_1 + \varepsilon^2\hat{z}_2 + ... \tag{A.9}$$

At leading order, we have

$$\frac{\mathrm{d}\hat{x}_0}{\mathrm{d}\hat{t}} = \frac{U}{c}\,, \quad \text{with solution} \quad \hat{x}_0 = \frac{U}{c}\hat{t} + \hat{X}_0\,, \tag{A.10}$$

$$\frac{\mathrm{d}\hat{z}_0}{\mathrm{d}\hat{t}} = 0\,, \quad \text{with solution} \quad \hat{z}_0 = \hat{Z}_0\,. \tag{A.11}$$

At the next order

$$\frac{\mathrm{d}\hat{x}_1}{\mathrm{d}\hat{t}} = \mathrm{e}^{\hat{z}_0}\cos\left(\hat{x}_0 - \hat{t}\right) \tag{A.12}$$

$$= \mathrm{e}^{\hat{Z}_0}\cos\left(\hat{X}_0 - (1-\tfrac{U}{c})\hat{t}\right) \tag{A.13}$$

$$\hat{x}_1 = -\frac{1}{1-U/c}\mathrm{e}^{\hat{Z}_0}\sin\left(\hat{X}_0 - (1-\tfrac{U}{c})\hat{t}\right). \tag{A.14}$$

Similarly,

$$\frac{\mathrm{d}\hat{z}_1}{\mathrm{d}\hat{t}} = \mathrm{e}^{\hat{z}_0}\sin\left(\hat{x}_0 - \hat{t}\right) \tag{A.15}$$

$$= \mathrm{e}^{\hat{Z}_0}\sin\left(\hat{X}_0 - (1-\tfrac{U}{c})\hat{t}\right) \tag{A.16}$$

$$\hat{z}_1 = \frac{1}{1-U/c}\mathrm{e}^{\hat{Z}_0}\cos\left(\hat{X}_0 - (1-\tfrac{U}{c})\hat{t}\right). \tag{A.17}$$

Substituting the solutions for $\hat{x}_0$, $\hat{x}_1$, $\hat{z}_0$ and $\hat{z}_1$ in our regular perturbation expansion (A.8, A.9), we get

$$\hat{x} = \hat{X}_0 + \frac{U}{c}\hat{t} - \frac{\varepsilon}{1-U/c}\mathrm{e}^{\hat{Z}_0}\sin\left(\hat{X}_0 - (1-\tfrac{U}{c})\hat{t}\right) + O(\varepsilon^2), \tag{A.18}$$

$$\hat{z} = \hat{Z}_0 + \frac{\varepsilon}{1-U/c}\mathrm{e}^{\hat{Z}_0}\cos\left(\hat{X}_0 - (1-\tfrac{U}{c})\hat{t}\right) + O(\varepsilon^2). \tag{A.19}$$

Using dimensional variables, the vehicle trajectory is

$$x = X_0 + Ut - a\frac{\sigma}{\omega}\mathrm{e}^{kZ_0}\sin\left(kX_0 - \omega t\right), \tag{A.20}$$

$$z = Z_0 + a\frac{\sigma}{\omega}\mathrm{e}^{kZ_0}\cos\left(kX_0 - \omega t\right), \tag{A.21}$$

where $\omega = \sigma - kU$ is the Doppler shifted frequency.

AUV-based velocity measurements

We can now compute the mean u-velocity profile relative to the earth as measured by an onboard ADCP, u_{Lq}. We donote the height of the range cell (above or below the AUV) by Δz. Then

$$u_{Lq} = u_w(x(t), z(t) + \Delta z; t)\,, \tag{A.22}$$

where $x(t)$ and $z(t)$ describe the vehicle's trajectory. Again, for simplicity, we assume deep water waves

$$u_{Lq} = a\sigma e^{k(z(t)+\Delta z)} \cos\left(kx(t) - \sigma t\right)\,. \tag{A.23}$$

To solve for the time-averaged velocity profiles, we use a Taylor series expansion to include first order variations in both fluid velocity components and time average over one wave cycle (indicated here by the overbar)

$$\overline{u}_{Lq} = \overline{u_{Lq}\left(X_0, Z_0; t\right)} + \overline{(x - X_0)\left.\frac{\partial u_{Lq}}{\partial x}\right|_{X_0,Z_0}} + \overline{(z - Z_0)\left.\frac{\partial u_{Lq}}{\partial z}\right|_{X_0,Z_0}} + \ldots \tag{A.24}$$

where

$$(x - X_0) = -a\frac{\sigma}{\omega}\mathrm{e}^{kZ_0}\sin\left(kX_0 - \omega t\right)\,, \tag{A.25}$$

$$(z - Z_0) = a\frac{\sigma}{\omega}\mathrm{e}^{kZ_0}\cos\left(kX_0 - \omega t\right)\,, \tag{A.26}$$

$$\left.\frac{\partial u_{Lq}}{\partial x}\right|_{X_0,Z_0} = -ak\sigma\mathrm{e}^{k(Z_0+\Delta z)}\sin\left(kX_0 - \omega t\right)\,, \tag{A.27}$$

$$\left.\frac{\partial u_{Lq}}{\partial z}\right|_{X_0,Z_0} = ak\sigma\mathrm{e}^{k(Z_0+\Delta z)}\cos\left(kX_0 - \omega t\right)\,, \tag{A.28}$$

hence

$$\overline{u}_{Lq} = a^2 k\frac{\sigma^2}{\omega}\mathrm{e}^{2kZ_0}\mathrm{e}^{k\Delta z}\,. \tag{A.29}$$

As is the case with Stokes drift, the vertical component of the wave-induced bias is zero.

Appendix B

Scaling Factor for Depth-averaged AUV Velocities

Time-averaged (20-min) ADCP-based alongshore velocity profiles at 12N, 12S, and 20W were normalized by their depth-averaged value, and interpolated onto a nondimensional range cell $r^* = r/h$, where r is the vertical range above the bottom-mounted ADCP and h is the local water depth derived from the ADCP pressure gauge. Normalized velocity profile ensembles were then averaged together ($\langle |v| / \int_0^1 |v| \mathrm{d}r^* \rangle$) and extrapolated to the surface via nearest neighbor extrapolation. Velocities below the first ADCP range cell were extrapolated to the seabed assuming a no-slip boundary condition and a logarithmic profile, following Arzeno et al. (2018). Figure B.1a shows normalized profiles derived from 12N, 12S, and 20W ensembles. Figure B.1b shows the vertical distribution of AUV-based samples (percentage of bursts) as a function of nondimensional depth (r^*) for the hydrodynamic surveys (H1–H3; see Table 4.1).

We apply a scaling factor (SF) to the uncorrected, depth-averaged AUV velocities to account for missing data close to the boundaries and within the DVL blanking range. We define the scaling factor as

$$SF = \frac{\overline{v}_{\text{full}}}{\overline{v}_{\text{missing}}}, \tag{B.1}$$

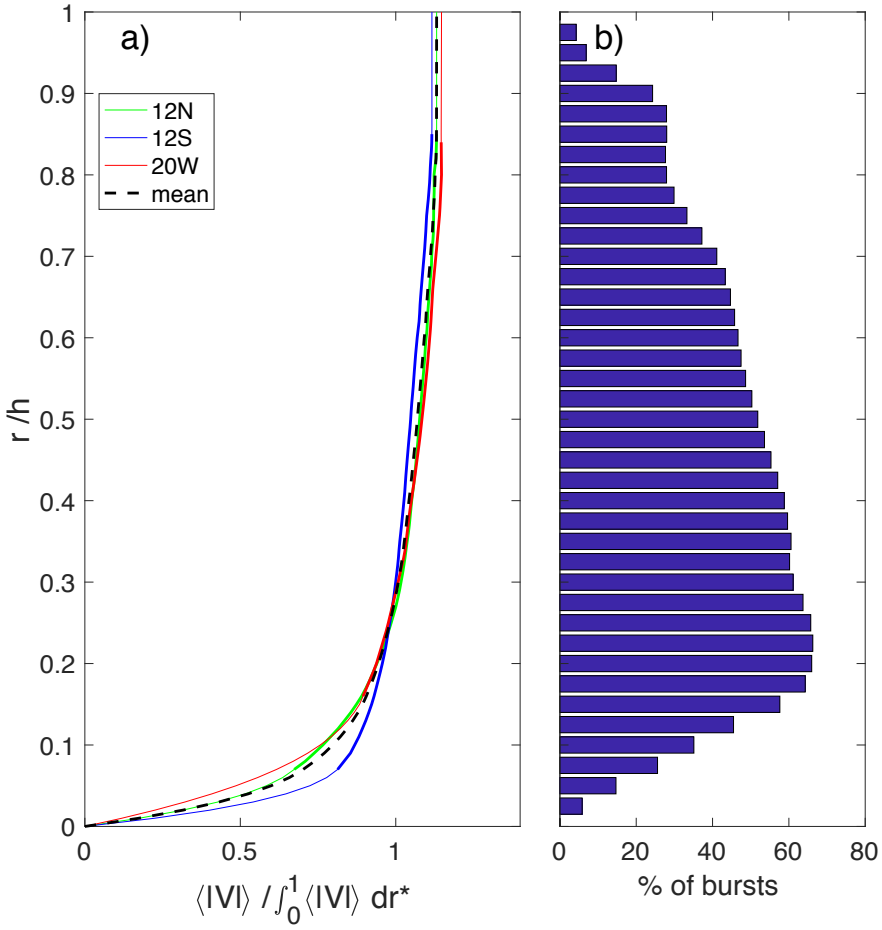

Figure B.1: (a) Alongshore velocity profiles from ADCP ensemble averaged observations at 12N (green), 12S (blue), and 20W (red), normalized by their corresponding depth-averaged velocity. Thin lines in (a) correspond to extrapolated values; the black dashed line shows the mean vertical profile, calculated using 12N, 12S, and 20W ensembles. (b) Vertical distribution of AUV-based velocity observations, normalized by the total number of observations. The vertical coordinate in both (a) and (b) represents height above the bed normalized by the local depth ($r^* = r/h$).

where $\overline{v}_{\text{full}} \equiv 1$ and $\overline{v}_{\text{missing}}$ is the depth average value of the empirical velocity profile (derived from ADCP ensembles) computed after removing all the missing values that are also absent from the corresponding DVL profile.

Scaling factors were calculated using normalized velocity profiles derived from 12N, 12S, and 20W ensembles, and their mean profile. Results were insensitive to the choice of scaling factor (varied by less than 3%), suggesting that our method is robust. AUV-based depth-averaged velocity measurements were corrected for missing data using a scaling factor derived from the mean ADCP-based velocity profile (dashed black line in Figure B.1a). Corresponding scaling factors ranged from 0.90 to 1.2, and were generally higher near the shallower regions of the survey domain.

Appendix C

Alongshore Momentum Balance

Consider a depth-averaged, incompressible, alongshore uniform, unsteady flow subject to an oscillating pressure gradient. Following Arzeno et al. (2018), we assume a balance between local acceleration, barotropic pressure gradient, and bottom drag

$$\frac{\partial V}{\partial t} = -g\frac{\partial \eta}{\partial y} - \frac{C_D}{h}V|V|\,, \tag{C.1}$$

$$-g\frac{\partial \eta}{\partial y} \propto \cos(\omega t)\,. \tag{C.2}$$

Here, x and y denote the cross- and alongshore directions, V is the depth-averaged alongshore velocity, ρ is the fluid density, $h(x)$ is the cross-shore variable depth of the flow, ω is the oscillating frequency, and t represents time; bottom stress has been parameterized as $\tau_b = \rho C_D V|V|$, where $C_D(x)$ is a cross-shore variable drag coefficient for depth-averaged flow. The sea surface height (η) and the pressure gradient ($g\partial\eta/\partial y$) are taken as uniform in the x-direction.

In deep water, far from shore ($x \to -\infty$) the unsteady term balances the barotropic pressure gradient; hence an oscillating pressure gradient given by:

$$-g\frac{\partial \eta}{\partial y} = \Lambda_0 \cos(\omega t)\,, \tag{C.3}$$

produces an oscillating flow with velocity

$$V = V_0 \sin(\omega t), \quad \text{as} \quad x \to -\infty, \tag{C.4}$$

and a characteristic velocity scale $V_0 \sim \Lambda_0/\omega$.

We define the following nondimensional variables

$$V^* = \frac{V}{V_0}, \quad t^* = \omega t, \tag{C.5}$$

and use (C.3) and (C.5) to rewrite the non-dimensional problem as

$$\frac{\partial V^*}{\partial t^*} = \cos(t^*) - F(x)V^*|V^*|, \quad \text{where} \quad F(x) = \frac{\Lambda_0 C_D(x)}{\omega^2 h(x)}, \tag{C.6}$$

represents a nondimensional drag coefficient that varies with forcing conditions, and with depth and C_D in the cross-shore direction.

In the nearshore region $\partial V^*/\partial t^* \to 0$, and the momentum budget shifts to a balance between the bottom drag and the pressure gradient. This dominant balance gives a characteristic length scale

$$h_\delta \sim \frac{\Lambda_0 C_D}{\omega^2} V^*|V^*| = \frac{V_0 C_D T}{2\pi} V^*|V^*|, \tag{C.7}$$

that is proportional to the velocity, drag coefficient, and oscillating period ($T = 2\pi/\omega$). This quantity can be interpreted as the depth at which the flow becomes fully developed for a given pressure gradient (Λ_0) and oscillating period (T), and is associated with the height of the turbulent bottom boundary layer.

Bibliography

Amador, A., I. B. Arzeno, S. N. Giddings, M. Merrifield, and G. Pawlak, 2020a: Cross-shore structure of tidally driven alongshore flow over rough bathymetry, manuscript in preparation.

Amador, A., S. N. Giddings, and G. Pawlak, 2020b: ADCP-based estimates of lateral turbulent Reynolds stresses in wavy coastal environments, manuscript in preparation.

Amador, A., S. Jaramillo, and G. Pawlak, 2017: ADCP bias and Stokes drift in AUV-based velocity measurements. *Journal of Atmospheric and Oceanic Technology*, **34 (9)**, 2029–2042.

Amador, A., G. Pawlak, and S. Jaramillo, 2015: ADCP bias and Stokes drift in AUV-based measurements. *Current, Waves and Turbulence Measurement (CWTM), 2015 IEEE/OES Eleventh*, IEEE, 1–5.

Anderson, W., J. M. Barros, K. T. Christensen, and A. Awasthi, 2015: Numerical and experimental study of mechanisms responsible for turbulent secondary flows in boundary layer flows over spanwise heterogeneous roughness. *Journal of Fluid Mechanics*, **768**, 316–347.

Arzeno, I. B., A. Collignon, M. A. Merrifield, S. N. Giddings, and G. Pawlak, 2018: An alongshore momentum budget over a fringing tropical fore-reef. *Journal of Geophysical Research: Oceans*, **123 (11)**, 7839–7855.

Atkinson, M., and R. Bilger, 1992: Effects of water velocity on phosphate uptake in coral reef-hat communities. *Limnology and Oceanography*, **37 (2)**, 273–279.

Atkinson, M., J. Falter, and C. J. Hearn, 2001: Nutrient dynamics in the biosphere 2 coral reef mesocosm: water velocity controls NH4 and PO4 uptake. *Coral Reefs*, **20 (4)**, 341–346.

Austin, J. A., and S. J. Lentz, 2002: The inner shelf response to wind-driven upwelling and downwelling. *Journal of Physical Oceanography*, **32 (7)**, 2171–2193.

Baird, M., and M. Atkinson, 1997: Measurement and prediction of mass transfer to experimental coral reef communities. *Limnology and Oceanography*, **42 (8)**, 1685–1693.

Barros, J. M., and K. T. Christensen, 2014: Observations of turbulent secondary flows in a rough-wall boundary layer. *Journal of Fluid Mechanics*, **748**.

Becker, J., M. A. Merrifield, and M. Ford, 2014: Water level effects on breaking wave setup for Pacific Island fringing reefs. *Journal of Geophysical Research: Oceans*, **119 (2)**, 914–932.

Bian, C., Z. Liu, Y. Huang, L. Zhao, and W. Jiang, 2018: On estimating turbulent Reynolds stress in wavy aquatic environment. *Journal of Geophysical Research: Oceans*, **123 (4)**, 3060–3071.

Bowen, A. J., 1969: The generation of longshore currents on a plane beach. *J. Mar. Res.*, **27 (2)**, 206–215.

Bowen, A. J., and R. A. Holman, 1989: Shear instabilities of the mean longshore current: 1. theory. *Journal of Geophysical Research: Oceans*, **94 (C12)**, 18 023–18 030.

Boyd, T., M. Inall, E. Dumont, and C. Griffiths, 2010: AUV observations of mixing in the tidal outflow from a Scottish sea loch. *Autonomous Underwater Vehicles (AUV), 2010 IEEE/OES*, IEEE, 1–9.

Bricker, J. D., and S. G. Monismith, 2007: Spectral wave–turbulence decomposition. *Journal of Atmospheric and Oceanic Technology*, **24 (8)**, 1479–1487.

Brink, K. H., 2016: Cross-shelf exchange. *Annual Review of Marine Science*, **8**, 59–78.

Brown, C. A., Y. Huot, M. J. Purcell, J. J. Cullen, and M. R. Lewis, 2004: Mapping coastal optical and biogeochemical variability using an autonomous underwater vehicle and a new bio-optical inversion algorithm. *Limnol. Oceanogr. Methods*, **2**, 262–281.

Brown, J., C. Tuggle, J. MacMahan, and A. Reniers, 2011: The use of autonomous vehicles for spatially measuring mean velocity profiles in rivers and estuaries. *Intelligent Service Robotics*, **4 (4)**, 233–244.

Burchard, H., 2002: *Applied turbulence modelling in marine waters*, Vol. 100. Springer Science & Business Media.

Burchard, H., and Coauthors, 2008: Observational and numerical modeling methods for quantifying coastal ocean turbulence and mixing. *Progress in Oceanography*, **76 (4)**, 399–442.

Carter, G. S., and Coauthors, 2008: Energetics of M2 barotropic-to-baroclinic tidal conversion at the Hawaiian Islands. *Journal of Physical Oceanography*, **38 (10)**, 2205–2223.

Clark, D. B., F. Feddersen, and R. Guza, 2010: Cross-shore surfzone tracer dispersion in an alongshore current. *Journal of Geophysical Research: Oceans*, **115 (C10)**.

Coles, D., 1956: The law of the wake in the turbulent boundary layer. *Journal of Fluid Mechanics*, **1 (2)**, 191–226.

Cowen, R. K., and S. Sponaugle, 2009: Larval dispersal and marine population connectivity. *Annual Review of Marine Science*, **1**, 443–466.

Csanady, G., 1972: The coastal boundary layer in Lake Ontario: Part II. the summer-fall regime. *Journal of Physical Oceanography*, **2 (2)**, 168–176.

Davis, K. A., S. J. Lentz, J. Pineda, J. Farrar, V. Starczak, and J. Churchill, 2011: Observations of the thermal environment on red sea platform reefs: a heat budget analysis. *Coral Reefs*, **30 (1)**, 25–36.

Dewey, R., and S. Stringer, 2015: Reynolds stresses and turbulent kinetic energy estimates from various ADCP beam configurations: Theory. Unpublished manuscript.

Diedenhofen, B., and J. Musch, 2015: cocor: A comprehensive solution for the statistical comparison of correlations. *PloS one*, **10 (4)**, e0121 945.

Duvall, M. S., J. L. Hench, and J. H. Rosman, 2019: Collapsing complexity: quantifying multi-scale properties of reef topography. *Journal of Geophysical Research: Oceans*.

Emery, W., and R. Thomson, 1997: *Data analysis methods in physical oceanography*. Pergamon.

Falter, J. L., M. J. Atkinson, and M. A. Merrifield, 2004: Mass-transfer limitation of nutrient uptake by a wave-dominated reef flat community. *Limnology and Oceanography*, **49 (5)**, 1820–1831.

Feddersen, F., and R. Guza, 2003: Observations of nearshore circulation: Alongshore uniformity. *Journal of Geophysical Research: Oceans*, **108 (C1)**, 6–1.

Feddersen, F., R. Guza, S. Elgar, and T. Herbers, 2000: Velocity moments in alongshore bottom stress parameterizations. *Journal of Geophysical Research: Oceans*, **105 (C4)**, 8673–8686.

Feddersen, F., and A. Williams, 2007: Direct estimation of the Reynolds stress vertical structure in the nearshore. *Journal of Atmospheric and Oceanic Technology*, **24 (1)**, 102–116.

Ferrario, F., M. W. Beck, C. D. Storlazzi, F. Micheli, C. C. Shepard, and L. Airoldi, 2014: The effectiveness of coral reefs for coastal hazard risk reduction and adaptation. *Nature communications*, **5**, 3794.

Fewings, M. R., and S. J. Lentz, 2010: Momentum balances on the inner continental shelf at Martha's Vineyard Coastal Observatory. *Journal of Geophysical Research: Oceans*, **115 (C12)**.

Fletcher, C. H., and Coauthors, 2012: *National assessment of shoreline change: Historical shoreline change in the Hawaiian Islands*. Reston, Virginia: U.S. Geological Survey.

Fong, D. A., and N. L. Jones, 2006: Evaluation of AUV-based ADCP measurements. *Limnol. Oceanogr. Methods*, **4**, 58–67.

Fong, D. A., and S. G. Monismith, 2004: Evaluation of the accuracy of a ship-mounted, bottom-tracking ADCP in a near-shore coastal flow. *Journal of Atmospheric and Oceanic Technology*, **21 (7)**, 1121–1128.

Genin, A., S. G. Monismith, M. A. Reidenbach, G. Yahel, and J. R. Koseff, 2009: Intense benthic grazing of phytoplankton in a coral reef. *Limnology and Oceanography*, **54 (3)**, 938–951.

Gerbi, G. P., J. H. Trowbridge, J. B. Edson, A. J. Plueddemann, E. A. Terray, and J. J. Fredericks, 2008: Measurements of momentum and heat transfer across the air–sea interface. *Journal of Physical Oceanography*, **38 (5)**, 1054–1072.

González-Castro, J. A., and M. Muste, 2007: Framework for estimating uncertainty of ADCP measurements from a moving boat by standardized uncertainty analysis. *Journal of Hydraulic Engineering*, **133 (12)**, 1390–1410.

Goodman, L., E. R. Levine, and Z. Wang, 2010: Subsurface observations of surface waves from an autonomous underwater vehicle. *IEEE Journal of Oceanic Engineering*, **35 (4)**, 779–784.

Goodman, L., and Z. Wang, 2009: Turbulence observations in the northern bight of Monterey Bay from a small AUV. *Journal of Marine Systems*, **77 (4)**, 441–458.

Gove, J. M., and Coauthors, 2016: Near-island biological hotspots in barren ocean basins. *Nature communications*, **7**, 10 581.

Green, R. H., R. J. Lowe, and M. L. Buckley, 2018: Hydrodynamics of a tidally forced coral reef atoll. *Journal of Geophysical Research: Oceans*, **123 (10)**, 7084–7101.

Guenther, G. C., M. W. Brooks, and P. E. LaRocque, 2000: New capabilities of the "SHOALS" airborne lidar bathymeter. *Remote Sensing of Environment*, **73 (2)**, 247–255.

Hally-Rosendahl, K., F. Feddersen, and R. Guza, 2014: Cross-shore tracer exchange between the surfzone and inner-shelf. *Journal of Geophysical Research: Oceans*, **119 (7)**, 4367–4388.

Hashimoto, N., 1997: Analysis of the directional wave spectrum from field data. *Advances in Coastal and Ocean Engineering*, **3**, 103–144.

Haven, S., and E. A. Terray, 2015: Surface wave measurements from an autonomous underwater vehicle. *Current, Waves and Turbulence Measurement (CWTM), 2015 IEEE/OES Eleventh*, IEEE, 1–7.

Hearn, C. J., 2011: Perspectives in coral reef hydrodynamics. *Coral Reefs*, **30 (1)**, 1.

Hearn, C. J., M. Atkinson, and J. Falter, 2001: A physical derivation of nutrient-uptake rates in coral reefs: effects of roughness and waves. *Coral Reefs*, **20 (4)**, 347–356.

Hench, J. L., J. J. Leichter, and S. G. Monismith, 2008: Episodic circulation and exchange in a wave-driven coral reef and lagoon system. *Limnology and Oceanography*, **53 (6)**, 2681–2694.

Hench, J. L., and J. H. Rosman, 2013: Observations of spatial flow patterns at the coral colony scale on a shallow reef flat. *Journal of Geophysical Research: Oceans*, **118 (3)**, 1142–1156.

Hendrickson, J., and J. MacMahan, 2009: Diurnal sea breeze effects on inner-shelf cross-shore exchange. *Continental Shelf Research*, **29 (18)**, 2195–2206.

Hittner, J. B., K. May, and N. C. Silver, 2003: A Monte Carlo evaluation of tests for comparing dependent correlations. *The Journal of General Psychology*, **130 (2)**, 149–168.

Holman, R., M. Haller, T. Lippmann, K. Holland, and B. Jaffe, 2015: Advances in nearshore processes research: Four decades of progress. *Shore & Beach*, **83 (1)**, 39.

Horwitz, R. M., and S. J. Lentz, 2016: The effect of wind direction on cross-shelf transport on an initially stratified inner shelf. *Journal of Marine Research*, **74 (4)**, 201–227.

Hughes, A. D., and A. G. Grottoli, 2013: Heterotrophic compensation: a possible mechanism for resilience of coral reefs to global warming or a sign of prolonged stress? *PLoS One*, **8 (11)**, e81 172.

Irish, J. L., and W. J. Lillycrop, 1999: Scanning laser mapping of the coastal zone: the shoals system. *ISPRS Journal of Photogrammetry and Remote Sensing*, **54 (2-3)**, 123–129.

Jaramillo, S., and G. Pawlak, 2010: AUV-based observations of rough bed hydrodynamics. *Autonomous Underwater Vehicles (AUV), 2010 IEEE/OES*, IEEE, 1–9.

Jaramillo, S., and G. Pawlak, 2011: AUV-based bed roughness mapping over a tropical reef. *Coral Reefs*, **30 (1)**, 11–23.

Jensen, B., B. Sumer, and J. Fredsøe, 1989: Turbulent oscillatory boundary layers at high Reynolds numbers. *Journal of Fluid Mechanics*, **206**, 265–297.

Jiménez, J., 2004: Turbulent flows over rough walls. *Annu. Rev. Fluid Mech.*, **36**, 173–196.

Jones, G., G. Almany, G. Russ, P. Sale, R. Steneck, M. Van Oppen, and B. Willis, 2009: Larval retention and connectivity among populations of corals and reef fishes: history, advances and challenges. *Coral Reefs*, **28 (2)**, 307–325.

Jones, N. L., R. J. Lowe, G. Pawlak, D. A. Fong, and S. G. Monismith, 2008: Plume dispersion on a fringing coral reef system. *Limnol. Oceanogr.*, **53 (5)**, 2273–2286.

Joyce, T. M., 1989: On in situ "calibration" of shipboard ADCPs. *Journal of Atmospheric and Oceanic Technology*, **6 (1)**, 169–172.

Kaimal, J. C., J. Wyngaard, Y. Izumi, and O. Coté, 1972: Spectral characteristics of surface-layer turbulence. *Quarterly Journal of the Royal Meteorological Society*, **98 (417)**, 563–589.

Kirincich, A. R., 2013: Long-term observations of turbulent Reynolds stresses over the inner continental shelf. *Journal of Physical Oceanography*, **43 (12)**, 2752–2771.

Kirincich, A. R., S. J. Lentz, and G. P. Gerbi, 2010: Calculating Reynolds stresses from ADCP measurements in the presence of surface gravity waves using the cospectra-fit method. *Journal of Atmospheric and Oceanic Technology*, **27 (5)**, 889–907.

Kirincich, A. R., and J. H. Rosman, 2011: A comparison of methods for estimating Reynolds stress from ADCP measurements in wavy environments. *Journal of Atmospheric and Oceanic Technology*, **28 (11)**, 1539–1553.

Kumar, N., G. Voulgaris, J. C. Warner, and M. Olabarrieta, 2012: Implementation of the vortex force formalism in the coupled ocean-atmosphere-wave-sediment transport (COAWST) modeling system for inner shelf and surf zone applications. *Ocean Modelling*, **47**, 65–95.

Lentz, S. J., 1994: Current dynamics over the northern California inner shelf. *Journal of Physical Oceanography*, **24 (12)**, 2461–2478.

Lentz, S. J., J. H. Churchill, and K. A. Davis, 2018: Coral reef drag coefficients–surface gravity wave enhancement. *Journal of Physical Oceanography*, **48 (7)**, 1555–1566.

Lentz, S. J., J. H. Churchill, K. A. Davis, and J. T. Farrar, 2016a: Surface gravity wave transformation across a platform coral reef in the Red Sea. *Journal of Geophysical Research: Oceans*, **121 (1)**, 693–705.

Lentz, S. J., J. H. Churchill, K. A. Davis, J. T. Farrar, J. Pineda, and V. Starczak, 2016b: The characteristics and dynamics of wave-driven flow across a platform coral reef in the Red Sea. *Journal of Geophysical Research: Oceans*, **121 (2)**, 1360–1376.

Lentz, S. J., K. A. Davis, J. H. Churchill, and T. M. DeCarlo, 2017: Coral reef drag coefficients–water depth dependence. *Journal of Physical Oceanography*, **47 (5)**, 1061–1075.

Lentz, S. J., M. Fewings, P. Howd, J. Fredericks, and K. Hathaway, 2008: Observations and a model of undertow over the inner continental shelf. *Journal of Physical Oceanography*, **38 (11)**, 2341–2357.

Lentz, S. J., and M. R. Fewings, 2012: The wind-and wave-driven inner-shelf circulation. *Annual Review of Marine Science*, **4**, 317–343.

Lentz, S. J., R. Guza, S. Elgar, F. Feddersen, and T. Herbers, 1999: Momentum balances on the North Carolina inner shelf. *Journal of Geophysical Research: Oceans*, **104 (C8)**, 18 205–18 226.

Lentz, S. J., and C. Winant, 1986: Subinertial currents on the southern California shelf. *Journal of Physical Oceanography*, **16 (11)**, 1737–1750.

Lewis, A., and S. Hutchinson, 2001: Great Barrier Reef depth and elevation model. *GBRDEM. CRC Reef Research Centre, Townsville*.

Lohrmann, A., B. Hackett, and L. P. Røed, 1990: High resolution measurements of turbulence, velocity and stress using a pulse-to-pulse coherent sonar. *Journal of Atmospheric and Oceanic Technology*, **7 (1)**, 19–37.

Longuet-Higgins, M. S., 1970: Longshore currents generated by obliquely incident sea waves: 1. *Journal of Geophysical Research*, **75 (33)**, 6778–6789.

Longuet-Higgins, M. S., and R. Stewart, 1964: Radiation stresses in water waves; a physical discussion, with applications. *Deep Sea Research and Oceanographic Abstracts*, Elsevier, Vol. 11, 529–562.

Lowe, R. J., and J. L. Falter, 2015: Oceanic forcing of coral reefs. *Annual Review of Marine Science*, **7**, 43–66.

Lowe, R. J., J. R. Koseff, and S. G. Monismith, 2005: Oscillatory flow through submerged canopies: 1. velocity structure. *Journal of Geophysical Research: Oceans*, **110 (C10)**.

Lowe, R. J., A. S. Leon, G. Symonds, J. L. Falter, and R. Gruber, 2015: The intertidal hydraulics of tide-dominated reef platforms. *Journal of Geophysical Research: Oceans*, **120 (7)**, 4845–4868.

Lu, Y., and R. G. Lueck, 1999: Using a broadband ADCP in a tidal channel. Part II: Turbulence. *Journal of Atmospheric and Oceanic Technology*, **16 (11)**, 1568–1579.

Lugo-Fernandez, A., H. Roberts, and W. Wiseman Jr, 1998: Tide effects on wave attenuation and wave set-up on a caribbean coral reef. *Estuarine, Coastal and Shelf Science*, **47 (4)**, 385–393.

Lumley, J., and E. Terray, 1983: Kinematics of turbulence convected by a random wave field. *Journal of Physical Oceanography*, **13 (11)**, 2000–2007.

Mejia-Alvarez, R., and K. T. Christensen, 2013: Wall-parallel stereo particle-image velocimetry measurements in the roughness sublayer of turbulent flow overlying highly irregular roughness. *Physics of Fluids*, **25 (11)**, 115 109.

Mellor, G., 2002: Oscillatory bottom boundary layers. *Journal of Physical Oceanography*, **32 (11)**, 3075–3088.

Merrifield, M. A., P. E. Holloway, and T. S. Johnston, 2001: The generation of internal tides at the Hawaiian Ridge. *Geophysical Research Letters*, **28 (4)**, 559–562.

Mitchum, G. T., and A. J. Clarke, 1986: The frictional nearshore response to forcing by synoptic scale winds. *Journal of Physical Oceanography*, **16 (5)**, 934–946.

Moin, P., 2010: *Fundamentals of engineering numerical analysis*. Cambridge University Press.

Molina, L., G. Pawlak, J. Wells, S. Monismith, and M. A. Merrifield, 2014: Diurnal cross-shore thermal exchange on a tropical forereef. *Journal of Geophysical Research: Oceans*, **119 (9)**, 6101–6120.

Moline, M. A., and Coauthors, 2005: Remote environmental monitoring units: An autonomous vehicle for characterizing coastal environments. *Journal of Atmospheric and Oceanic Technology*, **22 (11)**, 1797–1808.

Monismith, S. G., 2007: Hydrodynamics of coral reefs. *Annu. Rev. Fluid Mech.*, **39**, 37–55.

Nash, J. D., E. Kunze, C. M. Lee, and T. B. Sanford, 2006: Structure of the baroclinic tide generated at Kaena Ridge, Hawaii. *Journal of Physical Oceanography*, **36 (6)**, 1123–1135.

Nezu, I., and H. Nakagawa, 1993: *Turbulence in open-channel flows*. A.A. Balkema.

Nickols, K., B. Gaylord, and J. Largier, 2012: The coastal boundary layer: predictable current structure decreases alongshore transport and alters scales of dispersal. *Marine Ecology Progress Series*, **464**, 17–35.

Nidzieko, N. J., D. A. Fong, and J. L. Hench, 2006: Comparison of Reynolds stress estimates derived from standard and fast-ping ADCPs. *Journal of Atmospheric and Oceanic Technology*, **23 (6)**, 854–861.

Nunes, V., and G. Pawlak, 2008: Observations of bed roughness of a coral reef. *Journal of Coastal Research*, **24 (sp2)**, 39–50.

Oltman-Shay, J., P. Howd, and W. Birkemeier, 1989: Shear instabilities of the mean longshore current: 2. field observations. *Journal of Geophysical Research: Oceans*, **94 (C12)**, 18 031–18 042.

Panton, R. L., 2013: *Incompressible flow*. John Wiley & Sons.

Paull, L., S. Saeedi, M. Seto, and H. Li, 2014: AUV navigation and localization: A review. *IEEE Journal of Oceanic Engineering*, **39 (1)**, 131–149.

Pawlak, G., and Coauthors, 2009: Development, deployment, and operation of Kilo Nalu nearshore cabled observatory. *OCEANS 2009-EUROPE*, IEEE, 1–10.

Pineda, J., V. Starczak, A. Tarrant, J. Blythe, K. A. Davis, T. Farrar, M. Berumen, and J. C. da Silva, 2013: Two spatial scales in a bleaching event: Corals from the mildest and the most extreme thermal environments escape mortality. *Limnology and Oceanography*, **58 (5)**, 1531–1545.

Pope, S. B., 2000: *Turbulent Flows*. Cambridge University Press.

Pratchett, M., and Coauthors, 2008: Effects of climate-induced coral bleaching on coral-reef fishes: Ecological and economic consequences. *Oceanography and Marine Biology: An Annual Review*, **46**, 251–296.

Quataert, E., C. Storlazzi, A. Van Rooijen, O. Cheriton, and A. Van Dongeren, 2015: The influence of coral reefs and climate change on wave-driven flooding of tropical coastlines. *Geophysical Research Letters*, **42 (15)**, 6407–6415.

RD Instruments, 1996: Acoustic Doppler current profiler: Principles of operation: A practical primer. RD Instruments, 20 pp.

Reidenbach, M. A., S. G. Monismith, J. R. Koseff, G. Yahel, and A. Genin, 2006: Boundary layer turbulence and flow structure over a fringing coral reef. *Limnology and Oceanography*, **51 (5)**, 1956–1968.

Roberts, C. M., and Coauthors, 2002: Marine biodiversity hotspots and conservation priorities for tropical reefs. *Science*, **295 (5558)**, 1280–1284.

Rogers, J. S., S. A. Maticka, V. Chirayath, C. B. Woodson, J. J. Alonso, and S. G. Monismith, 2018: Connecting flow over complex terrain to hydrodynamic roughness on a coral reef. *Journal of Physical Oceanography*, **48 (7)**, 1567–1587.

Rogers, J. S., S. G. Monismith, R. B. Dunbar, and D. Koweek, 2015: Field observations of wave-driven circulation over spur and groove formations on a coral reef. *Journal of Geophysical Research: Oceans*, **120 (1)**, 145–160.

Rogowski, P., and E. Terrill, 2015: Mapping velocity fields in coastal waters using an autonomous underwater vehicle. *Current, Waves and Turbulence Measurement (CWTM), 2015 IEEE/OES Eleventh*, IEEE, 1–8.

Rogowski, P., E. Terrill, and J. Chen, 2014: Observations of the frontal region of a buoyant river plume using an autonomous underwater vehicle. *Journal of Geophysical Research: Oceans*, **119 (11)**, 7549–7567.

Rosman, J. H., and G. P. Gerbi, 2017: Interpreting fixed-location observations of turbulence advected by waves: Insights from spectral models. *Journal of Physical Oceanography*, **47 (4)**, 909–931.

Rosman, J. H., and J. L. Hench, 2011: A framework for understanding drag parameterizations for coral reefs. *Journal of Geophysical Research: Oceans*, **116 (C8)**.

Rosman, J. H., J. L. Hench, J. R. Koseff, and S. G. Monismith, 2008: Extracting Reynolds stresses from acoustic Doppler current profiler measurements in wave-dominated environments. *Journal of Atmospheric and Oceanic Technology*, **25 (2)**, 286–306.

Rudnick, D. L., and Coauthors, 2003: From tides to mixing along the Hawaiian Ridge. *Science*, **301 (5631)**, 355–357.

Schlichting, H., and K. Gersten, 2016: *Boundary-layer theory*. Springer.

Scully, M. E., J. H. Trowbridge, C. R. Sherwood, K. R. Jones, and P. Traykovski, 2018: Direct measurements of mean Reynolds stress and ripple roughness in the presence of energetic forcing by surface waves. *Journal of Geophysical Research: Oceans*, **123 (4)**, 2494–2512.

Sebens, K., S. Grace, B. Helmuth, E. Maney Jr, and J. Miles, 1998: Water flow and prey capture by three scleractinian corals, madracis mirabilis, montastrea cavernosa and porites porites, in a field enclosure. *Marine Biology*, **131 (2)**, 347–360.

Sevadjian, J., M. McManus, K. Benoit-Bird, and K. Selph, 2012: Shoreward advection of phytoplankton and vertical re-distribution of zooplankton by episodic near-bottom water pulses on an insular shelf: Oahu, Hawaii. *Continental Shelf Research*, **50**, 1–15.

Sevadjian, J. C., M. McManus, and G. Pawlak, 2010: Effects of physical structure and processes on thin zooplankton layers in Mamala Bay, Hawaii. *Marine Ecology Progress Series*, **409**, 95–106.

Sgarioto, D. E., 2011: *The Influence of Shallow Water Waves on the REMUS Autonomous Underwater Vehicle*. Defence Technology Agency.

Shaw, W. J., and J. H. Trowbridge, 2001: The direct estimation of near-bottom turbulent fluxes in the presence of energetic wave motions. *Journal of Atmospheric and Oceanic Technology*, **18 (9)**, 1540–1557.

Shiono, K., and D. W. Knight, 1991: Turbulent open-channel flows with variable depth across the channel. *Journal of Fluid Mechanics*, **222**, 617–646.

Signell, R. P., and W. R. Geyer, 1991: Transient eddy formation around headlands. *Journal of Geophysical Research: Oceans*, **96 (C2)**, 2561–2575.

Sinnett, G., F. Feddersen, G. Pawlak, A. Lucas, and E. Terrill, 2016: Observations of nonlinear internal wave runup into the surfzone. *AGU Fall Meeting Abstracts*.

Smalley, R., S. Leonardi, R. Antonia, L. Djenidi, and P. Orlandi, 2002: Reynolds stress anisotropy of turbulent rough wall layers. *Experiments in fluids*, **33 (1)**, 31–37.

Smith, K. A., G. Rocheleau, M. A. Merrifield, S. Jaramillo, and G. Pawlak, 2016: Temperature variability caused by internal tides in the coral reef ecosystem of Hanauma Bay, Hawai'i. *Continental Shelf Research*, **116**, 1–12.

Stacey, M. T., S. G. Monismith, and J. R. Burau, 1999a: Measurements of Reynolds stress profiles in unstratified tidal flow. *Journal of Geophysical Research: Oceans*, **104 (C5)**, 10 933–10 949.

Stacey, M. T., S. G. Monismith, and J. R. Burau, 1999b: Observations of turbulence in a partially stratified estuary. *Journal of Physical Oceanography*, **29 (8)**, 1950–1970.

Stansfield, K., G. Gasparini, and D. Smeed, 2003: High-resolution observations of the path of the overflow from the Sicily Strait. *Deep Sea Research Part I: Oceanographic Research Papers*, **50 (9)**, 1129–1149.

Stansfield, K., and Coauthors, 2001: Deep-sea, high-resolution, hydrography and current measurements using an autonomous underwater vehicle: The overflow from the Strait of Sicily. *Geophys. Res. Lett.*, **28 (13)**, 2645–2648.

Suanda, S. H., and F. Feddersen, 2015: A self-similar scaling for cross-shelf exchange driven by transient rip currents. *Geophysical Research Letters*, **42 (13)**, 5427–5434.

Sumner, E., and Coauthors, 2013: First direct measurements of hydraulic jumps in an active submarine density current. *Geophys. Res. Lett.*, **40 (22)**, 5904–5908.

Taebi, S., R. J. Lowe, C. B. Pattiaratchi, G. N. Ivey, G. Symonds, and R. Brinkman, 2011: Nearshore circulation in a tropical fringing reef system. *Journal of Geophysical Research: Oceans*, **116 (C2)**.

Thomson, R. E., and W. J. Emery, 2014: *Data analysis methods in physical oceanography*. Newnes.

Thornton, E. B., and R. Guza, 1986: Surf zone longshore currents and random waves: Field data and models. *Journal of Physical Oceanography*, **16 (7)**, 1165–1178.

Trowbridge, J., 1998: On a technique for measurement of turbulent shear stress in the presence of surface waves. *Journal of Atmospheric and Oceanic Technology*, **15 (1)**, 290–298.

Trowbridge, J., and S. Elgar, 2001: Turbulence measurements in the surf zone. *Journal of Physical Oceanography*, **31 (8)**, 2403–2417.

Trowbridge, J., M. Scully, and C. R. Sherwood, 2018: The cospectrum of stress-carrying turbulence in the presence of surface gravity waves. *Journal of Physical Oceanography*, **48 (1)**, 29–44.

Trowbridge, J. H., and S. J. Lentz, 2018: The bottom boundary layer. *Annual Review of Marine Science*, **10**, 397–420.

Ulloa, H. N., K. A. Davis, S. G. Monismith, and G. Pawlak, 2018: Temporal variability in thermally driven cross-shore exchange: The role of semidiurnal tides. *Journal of Physical Oceanography*, **48 (7)**, 1513–1531.

Van Prooijen, B. C., J. A. Battjes, and W. S. Uijttewaal, 2005: Momentum exchange in straight uniform compound channel flow. *Journal of hydraulic engineering*, **131 (3)**, 175–183.

Vermaas, D., W. Uijttewaal, and A. Hoitink, 2011: Lateral transfer of streamwise momentum caused by a roughness transition across a shallow channel. *Water Resources Research*, **47 (2)**.

Whipple, A. C., R. A. Luettich, and H. E. Seim, 2006: Measurements of Reynolds stress in a wind-driven lagoonal estuary. *Ocean Dynamics*, **56 (3-4)**, 169–185.

Williams, E., and J. H. Simpson, 2004: Uncertainties in estimates of Reynolds stress and TKE production rate using the ADCP variance method. *Journal of Atmospheric and Oceanic Technology*, **21 (2)**, 347–357.

Willingham, D., W. Anderson, K. T. Christensen, and J. M. Barros, 2014: Turbulent boundary layer flow over transverse aerodynamic roughness transitions: induced mixing and flow characterization. *Physics of Fluids*, **26 (2)**, 025 111.

Wolanski, E., J. Imberger, and M. L. Heron, 1984: Island wakes in shallow coastal waters. *Journal of Geophysical Research: Oceans*, **89 (C6)**, 10 553–10 569.

Wolanski, E., and M. J. Kingsford, 2014: Oceanographic and behavioural assumptions in models of the fate of coral and coral reef fish larvae. *Journal of The Royal Society Interface*, **11 (98)**, 20140 209.

Wyatt, A. S., J. L. Falter, R. J. Lowe, S. Humphries, and A. M. Waite, 2012: Oceanographic forcing of nutrient uptake and release over a fringing coral reef. *Limnology and Oceanography*, **57 (2)**, 401–419.

Wyatt, A. S., R. J. Lowe, S. Humphries, and A. M. Waite, 2010: Particulate nutrient fluxes over a fringing coral reef: relevant scales of phytoplankton production and mechanisms of supply. *Marine Ecology Progress Series*, **405**, 113–130.

Yahel, G., A. F. Post, K. Fabricius, D. Marie, D. Vaulot, and A. Genin, 1998: Phytoplankton distribution and grazing near coral reefs. *Limnology and Oceanography*, **43 (4)**, 551–563.

Yang, X., and C. Meneveau, 2017: Modelling turbulent boundary layer flow over fractal-like multiscale terrain using large-eddy simulations and analytical tools. *Philosophical Transactions of the Royal Society A: Mathematical, Physical and Engineering Sciences*, **375 (2091)**, 20160 098.

Zhang, Z., J. Falter, R. Lowe, G. Ivey, and M. McCulloch, 2013: Atmospheric forcing intensifies the effects of regional ocean warming on reef-scale temperature anomalies during a coral bleaching event. *Journal of Geophysical Research: Oceans*, **118 (9)**, 4600–4616.

Zou, G. Y., 2007: Toward using confidence intervals to compare correlations. *Psychological Methods*, **12 (4)**, 399.